Coherent multi-exciton dynamics in semiconductor nanostructures via two-dimensional Fourier Transform optical spectroscopy

by

Katherine Walowicz Stone
B.S. Chemistry and B.S. Chemical Engineering
Michigan State University 2003

Submitted to the Department of Chemistry
in partial fulfillment of the requirements for the degree of

DOCTOR OF PHILOSOPHY

at the

MASSACHUSETTS INSTITUTE OF TECHNOLOGY

June 2009

Author .....
Department of Chemistry
May 6th, 2009

Certified by .....
Keith Adam Nelson
Professor of Chemistry
Thesis Supervisor

Accepted by .....
Robert W. Field
Chairman, Departmental Committee on Graduate Students

This doctoral thesis has been examined by a committee of the Department of Chemistry as follows:

Professor Jeffrey I. Steinfeld .....

Chairperson

Professor Keith A. Nelson .....

Thesis Supervisor

Professor Andrei Tokmakoff .....

Coherent multi-exciton dynamics in semiconductor nanostructures via two-dimensional Fourier Transform optical spectroscopy

by

Katherine Walowicz Stone

B.S. Chemistry and B.S. Chemical Engineering

Michigan State University 2003

Submitted to the Department of Chemistry
on May 6th, 2009, in partial fulfillment of the
requirements for the degree of
DOCTOR OF PHILOSOPHY

Abstract

The Coulomb correlations between photoexcited charged particles in materials such as photosynthetic complexes, conjugated polymer systems, J-aggregates, and bulk or nanostructured semiconductors produce a hierarchy of collective electronic excitations (i.e. excitons, biexcitons, etc.) which may be harnessed for applications in quantum optics, light-harvesting, or quantum information technologies. These excitations represent correlations among successively greater numbers of electrons and holes, and their associated multiple-quantum coherences could reveal detailed information about complex many-body interactions and dynamics. However, unlike single-quantum coherences involving excitons, multiple-quantum coherences do not radiate and they have largely eluded direct observation and characterization.

In this work, I present a novel optical technique, two-quantum two-dimensional Fourier transform optical spectroscopy, which allows direct observation of the dynamics of multiple-exciton states that reflect the correlations of their constituent electrons and holes. The approach is based on closely analogous methods in nuclear magnetic resonance, in which multiple phase-coherent fields are used to drive successive transitions such that multiple-quantum coherences can be accessed and probed. A spatiotemporal femtosecond pulse shaping technique has been used to overcome the challenge of control over multiple, noncollinear phase-coherent optical fields in the experimental geometries that are used to isolate selected signal contributions through wavevector matching. Results from a GaAs quantum well system reveal distinct coherences of biexcitons that are formed from two identical excitons or from two excitons whose holes are in different spin sublevels ("heavy-hole" and "light-hole" excitons). The biexciton binding energies and dephasing dynamics are

determined, and changes in the dephasing rates as a function of the excitation density are observed, revealing still higher-order correlations due to exciton-biexciton interactions. Two-quantum coherences due to four-particle correlations that do not involve bound biexciton states but that influence the exciton properties are also observed and characterized. I also present one-quantum two-dimensional Fourier transform optical spectroscopy measurements which show that the higher-order correlations isolated by two-quantum techniques are highly convolved with two-particle correlations in the conventional one-quantum measurements.

Thesis Supervisor: Keith Adam Nelson
Title: Professor of Chemistry

Biographical Note

Katherine Walowicz Stone (a.k.a. Kathy or Kasia) was born Katherine Ann Walowicz on January 14th, 1980 in Detroit, MI to Leszek Jan and Karolina Walowicz. She has one younger sister, Annette Barbara (a.k.a. Basia). She was raised in Sterling Heights, MI. She attended Adlai E. Stevenson High School in her hometown where she was captain of the girls' swim team and president of the National Honors Society. She also participated in Science Olympiad and Quiz Bowl. In 1998 she graduated Valedictorian of her class.

Kathy attended Michigan State University in East Lansing, MI from 1998 to 2003 and was a student in the Lyman Briggs School of Natural Science, the College of Engineering and the Honors College. In her freshman year she was a member of the Junior Varsity Womens' Crew Team. In 1999, Kathy began doing undergraduate research with Professor Marcos Dantus in the Chemistry Department where her research focus included ultrafast laser pulse shaping and coherent control of multiphoton absorption in condensed phase systems. Kathy was also President of the Michigan Alpha chapter of Tau Beta Pi, an honors society for students in engineering, from 2001 to 2002. Kathy graduated from university in May, 2003 with a B.S. in Chemistry and a B.S. in Chemical Engineering and she received the Distinguished Award in Chemistry, which is awarded to the graduating student with the highest grade point average in chemistry courses.

Kathy married her high school sweetheart, Nicholas Charles Stone, in June of 2003 with whom she moved to Boston, MA shortly after to begin a Ph.D. program in physical chemistry in the Department of Chemistry at MIT. With Professor Keith Adam Nelson, she studied techniques for spatiotemporal shaping of ultrafast laser pulses for nonlinear spectroscopy applications. When Kathy is not in the laboratory, she enjoys video games, cooking, gardening and brewing beer.

Acknowledgments

I was about 14 years old when I first settled on pursuing science and engineering as a career. I can recall that my first opportunity to seriously attempt a scientific experiment was for my 9th grade biology class. Back then I was mainly interested in botany, so I devised an experiment to test the effect of different lighting conditions on plant growth. I planted identical catnip seeds in identical containers filled with identical soil types and placed one container on a window sill so that it could receive natural light, and the other I placed in the basement underneath a fluorescent lamp. The basement seeds sprouted within a week and the resulting plant grew long and spindly with short, narrow leaves. The window seeds took much longer to sprout and the matured plant was bushy with broad leaves. I was excited that I had gotten such dramatically different-looking plants and so I started to hypothesize all sorts of exotic explanations as to why I had obtained those results. However, when I presented my experiment to the class, my teacher ignored my wild conjectures and asked me to simply recount my basic experimental procedure. By the end, I had come to the simple conclusion that the basement plant was most likely not catnip (which, if you've ever seen a catnip plant, it's not at all spindly and the leaves are broad with scalloped edges), but instead just a random weed that had sprouted because I just took the soil in which to plant the seeds from my backyard! In short, my first scientific experiment was a technical failure, but it did teach me a few simple aspects of the scientific method and I guess I have been honing those skills ever since. My professional development and accomplishments would not have been possible without the help of many people to whom I will attempt here to express my gratitude.

First, I would like to thank my Ph.D. research advisor, Keith Nelson. Keith has been an incredibly supportive mentor and guide. I have learned much about science from him and from the members of his team which he assembled. Keith taught me about the unique advantages afforded by pulse shaping which address the challenges of optical wave-mixing spectroscopy in very elegant ways, and I want to thank him for letting me pursue the techniques and experiments presented within these pages. I also want to thank him for believing in my work and supporting my efforts to publish the results and apply for a patent. Keith is also an extremely kind, friendly and fair person who is fun to be around.

I also want to thank several people who helped me directly with the work presented in this thesis. Daniel "Duffy" Turner is currently a 4th year graduate student in the Nelson group who joined the 2D FTOPT project in 2006. His assistance with maintaining the laser system and lab equipment, and making the actual measurements has been invaluable, and the modifications he made to optical setup made the rubidium measurements feasible. Kenan Gundogdu, who did a post-doc in the Nelson group from 2006 to 2008 and is now an Assistant Professor of Physics at North Carolina State University, helped me learn about 2D FT spectroscopy techniques and interpret the semiconductor quantum well measurements. Both Duffy and Kenan have been excellent co-workers with whom I've enjoyed many interesting and spirited scientific and non-scientific conversations. I also want to thank my collaborators at NIST/UC

Boulder, Steve Cundiff and the students and post-docs in his group, for the quantum well samples and their expertise in many-body phenomena in semiconductors.

I also want to thank the graduate student, Joshua Vaughan, and post-doc, Thomas Hornung, in the Nelson group who were my primary day-to-day mentors when I was a young graduate student. It was Josh who pioneered spatiotemporal pulse shaping in the Nelson group, and, along with Thomas, its application to nonlinear spectroscopy. They took me under their wing and taught me the basic optical techniques which are the foundation of my studies.

I also want to thank all the members of the Nelson group for creating a friendly and helpful working environment. Ka-Lo Yeh joined the group the same year as I. We started working on the same project, which diverged in the end, but she has remained a close collaborator and friend. I'll always remember the time we travelled down from Seattle to San Francisco by car after the Ultrafast Phenomena conference in 2006 and visited Crater Lake, Portland, and the giant redwood forest. Darius Torchinsky was a graduate student in physics (although I won't hold that against him) who is very knowledgable about spectroscopy in general, and was always good for a nice scientific (or not) discussion over coffee. I'd also like to thank Eric Statz and Ben Paxton for being a great resource for those laser, optic and cryostat-related technical issues. Dylan Arias and Patrick Wen are currently 2nd year graduate students embarking on exciting research projects related to 2D FTOPT and I'm looking forward to seeing their Ph.D. theses as well. I also wish to thank, for their advice and words of encouragement, Prof. Bob Field, Prof. Jeff Cina, Prof. Thomas Feurer, Prof. Marcos Dantus, and Dr. Igor Pastirk.

I also wish to express my gratitude to members of my family. To my father, for supporting my choice to pursue a career in science and for always remaining enthusiastic about it. To my mother, for teaching me to stand up for myself. To my sister, who was my first friend. To my mother-in-law and father-in-law, Sally and Tom, for letting me be myself. To my brother-in-law, Adam, and his wife, Jenny, for sibling Thanksgiving and welcome respites from lab work. And to my other brother-in-law, Aaron, for forgiving me for stealing his older brother away and being like a younger brother to me too.

Last, but certainly not least, I want to thank my husband, Nick, for lovingly supporting me during my years in graduate school. I would not have had the courage to move away from home to begin this journey, or to continue it, without him, and so it is to Nick that I dedicate this work. Thank you for taking care of the house, the bills, the meals, the laundry, and for taking care of me. Thank you for being my best friend. Thank you for the trips to Maine, Cooperstown, and London. Thank you for bringing home our cat, Juliet. To me, you'll never grow old, you'll never die, and you'll always eat oatmeal.

Contents

List of Figures

List of Tables

List of Abbreviations

2D FTOPT: Two-dimensional Fourier Transform optical spectroscopy

EID: Excitation-induced dephasing

EIS: Excitation-induced frequency (or energy) shift

FWM: Four-wave mixing

LFE: Local field effects

MOBE: Modified optical Bloch equations

OBE: Optical Bloch equations

QD: Quantum dot

QW: Quantum well

SLM: Spatial light modulator

X: Exciton-ground-state coherence

X_2: Biexciton-ground-state coherence

Chapter 1

Introduction

Charged particle correlations play a significant role in determining the coherent optical responses of semiconductor nanostructures and assemblies of molecular chromophores, which are being considered for new applications in light-harvesting, optoelectronic, and quantum information technologies. The collective electronic states of these materials are formed from linear combinations of the atomic or molecular orbitals belonging to their individual constituents such that the states are arranged into bands. Absorption of a photon can excite an electron from the filled valence band to the empty conduction band, leaving a positively charged "hole" in the valence band. It is the Coulomb force that mediates the correlation between the two particles and prompts the formation of a new bound state – a quasiparticle known as an exciton.

In semiconductors, the basis for the Wannier-Mott model describing the excitonic bands proceeds from delocalized Bloch wavefunctions. The exciton Bohr radius is large and the electron and hole are loosely bound to each other as they move throughout the material. In contrast, in molecular complexes, the excitonic bands are derived from molecular orbitals such that the Bohr radius of these so-called Frenkel excitons is small and the electron and hole remain strongly overlapped as they move through the complex. It is the delocalization of the atomic/molecular wavefunctions that determines the nature and dynamics of the exciton. The spatial extent of the exciton wavefunction can be controlled by modifying the nanoscale structure of the material [1] which provides opportunities for chemists to devise materials with useful optical

and electronic properties.

The optical properties of semiconductors can be tuned by alternately layering two different semiconductor films (with thickness on the order of nanometers) with different bandgaps or by synthesizing semiconductor particles of nanometer-scale diameter, such that the exciton is confined by a potential energy jump at the boundaries. The tailored optical properties of these so-called semiconductor quantum wells (QWs) and quantum dots (QDs) have proved useful for wide-ranging applications and continue to provide testbeds for fundamental study. For example, coupled QWs are attractive materials for the study of excitonic Bose-Einstein condensates since the exciton lifetime can be controlled with the application of an electric field through the quantum-confined Stark effect [2]. The exciton of a QW embedded in a microcavity can strongly couple to an electromagnetic field to form an exciton-polariton which is also an interesting candidate for solid-state Bose-Einstein condensates [3]. Semiconductor quantum dots are useful for applications in quantum control and quantum optics since the electron spin decoherence can be manipulated by an optical field [4] and the optical transitions can exhibit interference phenomena (i.e. an Autler-Townes splitting) when driven by a strong optical field [5].

In molecular complexes, the delocalization of the exciton is greatly influenced by the nanoscale arrangement of the chromophores such that the optical properties of conjugated polymers and J-aggregates are strongly dependent on the aggregation state [1]. These materials play important roles in electroluminescent and photovoltaic devices. Their high absorption coefficients enable strong coupling with an optical field, producing luminescent exciton-polariton states when nanolayers of material are sandwiched between the highly reflective surfaces of a microcavity [6]. Integration of inorganic materials, such as quantum dots, which have high fluorescence yields compared to organic molecules, into these devices increases their luminescent efficiency [7].

Linear and nonlinear ultrafast spectroscopy techniques [8] are conducive to the study of exciton properties. However, several observations of semiconductor nanostructures and molecular chromophore assemblies have shown that correlations *between*

excitons are significant and that the spectral signatures dependent on their interactions may be largely convolved in conventional measurements. The correlations give rise to exciton-exciton or exciton-free carrier scattering or the binding of two excitons to form a new bound quasiparticle known as a biexciton. The biexciton is often described in terms of a band of two-exciton states with approximately twice the energy of the one-exciton states that can be accessed by absorption of a second optical photon.

In biological light-harvesting complexes, coherently coupled electronic states [9] allow energy-efficient transfer of the photo-excited exciton [10]. Simulations of the coherent dynamics of multiple-electronic correlations such as biexcitons [11] demonstrate that states in the two-exciton manifold may play important roles in natural photosynthetic antenna complexes which appear to have evolved rapid relaxation pathways to avert damage under highly energized conditions. These two-exciton states may also be involved in the coherent control of exciton dynamics [12] in these materials. Absorption into the two-exciton band of a J-aggregate [13] is relevant to determining the size-dependence of optical nonlinearities and understanding processes such as exciton-exciton annihilation in these materials. Simulations of coherently coupled exciton states in J-aggregates demonstrate a promising method by which the exciton localization size under different experimental conditions can be investigated [14].

In semiconductor QWs, the effects of exciton-exciton interactions, or "many-body" effects [15], are especially prevalent since Wannier excitons have large Bohr radii. Not only are excitons originating from different valence bands coupled [16], but they may be scattered by exciton or free-carrier populations [17]. Furthermore, the scattering interactions can produce new contributions to the coherent optical response [18]. Biexciton formation also plays a significant role in the coherent optical response of QWs [19, 20, 21, 22]. Two-exciton states have been exploited in coherent control schemes [23] and used to access exciton spin coherences for quantum information processing [24]. In zinc oxide QWs, the biexciton binding energy is strong even at room temperature, making for a stable, strongly absorbing and, therefore, efficient

material for optoelectronic device applications [25]. Similarly, in semiconductor QDs, the complete nonlinear optical response can only be fully simulated when higher-order particle correlations are included [26]. Biexciton states have been exploited for controlling electromagnetically induced transparency [27] for slow-light applications and in an all-optical quantum gate [28] suitable for quantum information processing. Multiply excited states in semiconductor QDs may provide a route to harnessing the extra energy deposited in these materials by the absorption of highly energetic photons [29, 30].

Conventional time- and frequency-domain techniques are indiscriminate with respect to many of the spectroscopic signatures that would result from the coupling and interaction of excitons. Fortunately, recent efforts in ultrafast infrared (IR) spectroscopy have allowed the separation of coupled vibrational resonances by adapting methods from two-dimensional Fourier Transform nuclear magnetic resonance (2D FTNMR) spectroscopy. 2D FT spectroscopy uses sequences of pulsed electromagnetic fields to excite coherences in the sample which oscillate during the interpulse delays and whose phases depend on the phase relationships between the fields and the other coherences they generated during previous pulse delays. Coherent superpositions of states that differ by a single quantum, i.e. single-quantum coherences, can be generated through allowed one-photon transitions. Coherent superpositions of states that differ by multiple quanta, i.e. multiple-quantum transitions, are generally nonradiative, but they may be accessed through a sequence of one-photon transitions. Optical analogs to the one-quantum and multiple-quantum techniques used in 2D FTNMR and 2D FTIR spectroscopy would permit isolation of exciton coupling and interaction contributions to ultrafast optical (OPT) spectroscopy measurements, since 2D FT spectroscopy methods can reveal correlated coherent motions by providing another frequency axis along which spectral features resulting from coupled and interacting excitations can be spread.

While many groups have performed 2D FTIR measurements [31, 32, 33, 34], far fewer have attempted 2D FTOPT spectroscopy. 2D FTOPT measurements require detection of the full signal field through interferometric mixing with a reference field so

that the full optical analog to 2D FTNMR can be realized [35]. While background-free detection of the signal field can be realized by borrowing wavevector-matching techniques from optical four-wave mixing (FWM) spectroscopy, the main experimental challenge presented by wavevector definition in the optical regime lies in the difficulty of producing multiple beams of light with pulses whose optical phases are specified and maintained even when the pulses are variably delayed in time-resolved measurements. Typically, reflective [36, 37] or diffractive [38, 39] beam-splitting optics are used to produce four distinct beams containing the three excitation fields and the reference field. Glass prisms or delay stages coupled with actively stabilized feedback loops are used to impart the required interpulse delays. With these methods, however, only partial phase stability can be obtained, i.e. the first two fields produced by one beamsplitter are phase-related, as are the third field and reference field produced by another, but no well-defined phase relationship exists between the two pulse pairs. As discussed in subsequent chapters, this is all that is required to perform one-quantum measurements, but full phase stability is a requirement for two-quantum 2D FTOPT measurements since the key element is the two-quantum coherence that is created by the first two pulses and whose phase as well as amplitude is measured by the last two.

The Nelson group at MIT has pioneered the use of femtosecond pulse shaping techniques in the temporal [40] and spatial [41] domains for the coherent control of phonon-polaritons [42], which are collective vibrations of a crystal lattice coupled to light. Recently, we showed that spatiotemporal pulse shaping techniques can be used as a platform for various ultrafast spectroscopy experiments [43]. Not only does it offer passive phase stability of all non-collinearly propagating pulses through the use of common path optics, it is also capable of arbitrary waveform generation since independent control of the amplitude and phase profile of each pulse is possible. These characteristics make spatiotemporal pulse shaping ideal for 2D FTOPT spectroscopy experiments, especially when investigation of higher-order correlations or coherent control of the induced response is desired. The spatiotemporal pulse shaping technique for one-quantum and two-quantum 2D FTOPT measurements presented here is distinct from one-quantum 2D FTOPT measurements using collinear phase-controlled

pulses [44] where only a portion of the complex signal field is detected. A recently demonstrated method [45] using only conventional optics also promises full phase stability and full signal field detection, but without the ability to arbitrarily define the excitation waveforms.

In this work, I will present 2D FTOPT measurements using spatiotemporal pulse shaping on semiconductor QWs which reveal exciton coupling and interactions. I will also present the first two-quantum 2D FTOPT measurements on these materials that constitute the first direct observations of biexciton coherences and separation of four-particle correlations from two-particle (single-exciton) correlations. Chapter 2 details the pulse sequences used in one-quantum and two-quantum 2D FTOPT spectroscopy. Chapter 3 presents the spatiotemporal pulse shaping technique and discusses its advantages and limitations. The spectral signatures resulting from four-particle correlations can be modeled using a phenomenological treatment of exciton interactions which is presented in Chapter 4. Chapter 5 presents 2D FTOPT measurements on excitons in semiconductor QWs where the 2D spectral features and complex lineshapes permit direct observation and characterization of four-particle correlations. Chapter 6 presents 2D FTOPT measurement on dense rubidium vapor which contrast with the measurements on semiconductor excitons since the many-body correlations described in Chapter 5 that arise from long-range Coulomb interactions between excitons are absent for excitations in rubidium.

Chapter 2

Theory of 2D Fourier transform spectroscopy

Nonlinear multidimensional spectroscopic methods permit spreading of congested spectra along multiple time or frequency coordinates, as in nuclear magnetic resonance (NMR) spectroscopy [46], thereby enabling quantitative determination of couplings, anharmonicities, relative dipole orientations, and dynamical processes that depend on them. These unique abilities have been elegantly demonstrated in many experiments over the past several years using coherent 2D spectroscopy with ultrashort pulses in the mid-infrared [47, 48, 49, 50, 51] and in the visible or near-infrared [52, 9, 53, 44] spectral ranges. In this chapter, I will discuss the coherent dynamics measured in 2D FTOPT spectroscopy and introduce the sequences of optical field interactions that are used to probe these dynamics by relating 2D FTOPT measurements to one-quantum and multiple-quantum measurements used in 2D FTNMR.

2.1 Coupled two-particle correlations and one-quantum techniques

In NMR spectroscopy, 2D FT techniques are useful for studying correlated spin responses. In 2D FTNMR, a series of radiofrequency (RF) magnetic fields are used

to manipulate an ensemble of nuclear spins oriented in a dc magnetic field polarized perpendicular to the RF fields. The first RF field, referred to as a $\frac{\pi}{2}$-pulse because it moves the net magnetization vector by 90^o from the z axis to the x-y plane, inducing nuclear spin coherences that are described quantum mechanically as superpositions between $\mid +\rangle$ and $\mid -\rangle$ spin states oriented along and against the dc field and that constitute an ensemble of radiating magnetic dipoles. In the simplest form of NMR spectroscopy, the resulting "free induction decay" detected by a magnetic coil is used to determine the spin precession frequency, ω_s, and dephasing rate, γ_s. However, in a 2D FTNMR measurement a second RF field (also $\frac{\pi}{2}$) applied after a variable delay, τ_1, aligns the dipoles to the axis parallel with the dc field. During the following period, τ_2, a through-space dipole-dipole interaction causes an exchange of the magnetization. Then a third RF field (also $\frac{\pi}{2}$) restores the nuclear spin coherences whose radiation is sensed by a magnetic coil during the final period, t. Subsequent 2D FT of the signal with respect to τ_1 and t yields a 2D FTNMR spectrum which shows cross-peaks, indicating that a magnetic dipole took on two different spin precession frequencies during the first and final time periods due to the magnetization exchange that occurred during τ_2.

From the preceding description of coupled nuclear spins, it is evident how 2D FT spectroscopy can be used to separate coupled vibrational and electronic coherences using ultrafast laser pulses in the infrared (IR) [54] and optical (OPT) [55] regimes, respectively, by combining familiar four-wave mixing (FWM) spectroscopy techniques with interferometric detection of the signal field. One important difference between RF and IR/OPT fields is that, in 2D FTNMR, the RF wavelengths far exceed the sample dimensions, and the sample is surrounded by the coils that deliver the fields and measure the responses. In this limit, the RF field frequencies and polarizations are important but their propagation directions are not. In contrast, in 2D FTIR and 2D FTOPT measurements the sample is large compared to the wavelength, and the fields are delivered to the sample and radiated from it in the form of coherent light beams with well-defined propagation directions, i.e. wavevectors. The key opportunities afforded by wavevector definition lie in the use of a non-collinear geometry of the

beams at the sample and the specification of the pulse time-ordering to select and sharply limit the contributions to the measured signal that is radiated from the sample as a coherent beam in a well-defined direction. If the three ultrafast excitation fields, $\vec{E}_A$, $\vec{E}_B$ and $\vec{E}_C$, arrive at the sample with distinct wavevectors $\vec{k}_A$, $\vec{k}_B$ and $\vec{k}_C$, then the FWM signal field, $\vec{E}_S$, will radiate in the direction given by the wavevector-matching condition: $\vec{k}_S = \vec{k}_A + \vec{k}_B - \vec{k}_C$, as shown in Fig. 2-1.

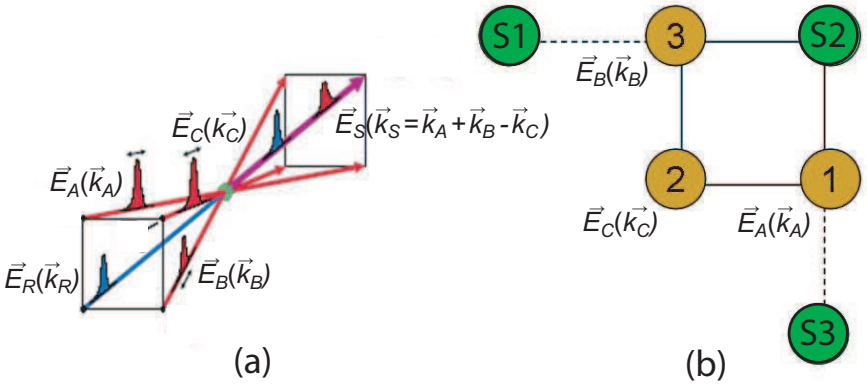

Figure 2-1: As in degenerate FWM spectroscopy experiments, 2D FTOPT can benefit from the use of non-collinear excitation fields arranged in the BOXCARS geometry (a) to spatially isolate three types of signals described as S1, S2, S3 (see main text). The spatial positions of the signals relative to the excitation fields are shown in (b) for the time-ordering of the fields where $\vec{E}_C$ is second to arrive at the sample. The spatial position of the signals will change if the time-ordering of fields is changed, such that the S1(S3) signal propagates to the fourth corner of the box if field $\vec{E}_C$ arrives first(last). A reference field, $\vec{E}_R$, which propagates in the same direction as the signal field, may be used for interferometric detection of the signal.

Two important types of one-quantum 2D FTOPT signals can be spatially isolated using this geometry just by changing the time-ordering of the "conjugate" field, $\vec{E}_C$ (so-called because it contributes its backward-propagating spatial and temporal components to the signal), such that it arrives first or second at the sample. In nonlinear spectroscopy terminology, these pulse sequences are named S1 and S2.

In the S1 pulse sequence, depicted in Fig. 2-2(a), field $\vec{E}_C$ arrives first to generate an exciton coherence in the sample, and after a variable delay, τ_1, interaction with field $\vec{E}_A$ produces an excited state population in a transient grating pattern with

wavevector $\vec{k}_A - \vec{k}_C$. The population grating diffracts the field $\vec{E}_B$, incident at the phase-matching or Bragg angle, to yield the coherently scattered signal $\vec{E}_S$, which evolves during the final time period t. The last excitation field $\vec{E}_B$ also reverses the temporal phase of the coherences that evolved during τ_1 such that the decay of $\vec{E}_S(\tau_1)$ yields the homogeneous dephasing time, since any inhomogeneous dephasing due to local variation in the frequency is reversed due to the "rephasing" induced by $\vec{E}_B$. Similar to the case of nuclear spins, if there are multiple electronic transitions excited at different frequencies within the spectral bandwidth of the pulses, then multiple coherences will be rephased in the signal field, and if two coherences are coupled, then the signal field components at each frequency will be modulated at the other frequency. The full signal field, $\vec{E}_S(\tau_1, t)$, is measured using interferometric methods with a reference field $\vec{E}_R$ that propagates collinearly with the signal field direction, i.e. $\vec{k}_R = \vec{k}_S$, and subsequent 2D Fourier transformation of the signal field yields a two-dimensional spectrum, $S(\omega_1, \omega)$, where coherences that evolved during $\tau_1(t)$ are spread along the $\omega_1(\omega)$ coordinate. The 2D spectrum shows diagonal peaks due to each individual coherence and off-diagonal cross-peaks that reveal the coupled exciton coherences. All of the peaks will be elongated along the diagonal and the linewidth of the peak antiparallel to the diagonal yields the homogeneous dephasing time.

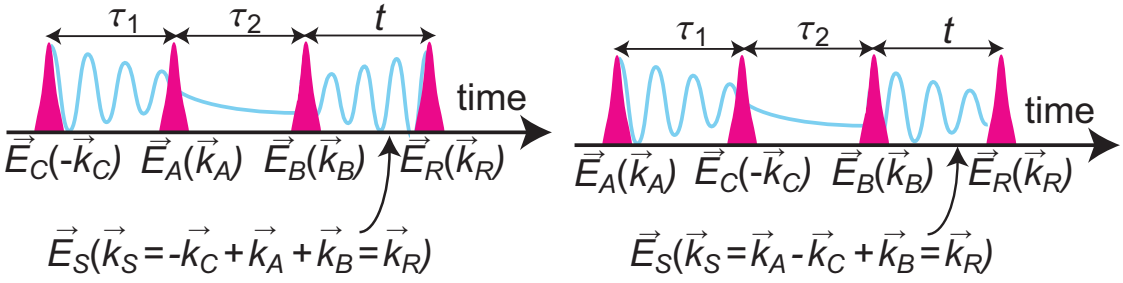

(a) Rephasing (S1) (b) Non-rephasing (S2)

Figure 2-2: Pulse sequences for one-quantum 2D FTOPT spectroscopy.

In the S2 pulse sequence, depicted in Fig. 2-2(b), field $\vec{E}_A$ arrives first to generate electronic coherences followed by field $\vec{E}_C$ which interacts to form the excited state population grating. In this case, the last field $\vec{E}_B$ does not reverse the temporal phase of the coherences excited by $\vec{E}_A$ and yields the so-called "non-rephasing" signal. As in

the S1 case, multiple coherences will be present in the signal field if the two coherences are coupled, such that 2D Fourier transformation of the signal shows diagonal and off-diagonal peaks. However, these peaks will not be elongated along the diagonal since the S2 pulse sequence is not able to eliminate inhomogeneous broadening from the sample. For both S1 and S2 measurements, the interpulse delay τ_2 can be scanned in order to obtain the lifetime of the excited state population. The off-diagonal features of the one-quantum 2D spectra can be monitored as a function of τ_2 which may reveal how electronic energy is coherently transferred between excitonic states.

Detection of the full signal field in these measurements allows separate examination of the real and imaginary parts of the sample response, revealing induced dynamics that are both absorptive and dispersive in character. In both the S1 and S2 cases, the complex parts of the 2D spectra are not purely absorptive or dispersive, unlike the real and imaginary parts of a 1D FTNMR spectrum. In the 1D measurement, the real part is purely absorptive and can be entirely negative-going, which indicates absorption, or entirely positive-going, which indicates emission. The imaginary part of the 1D spectrum is dispersive and indicates a change in phase, rather than amplitude, of the signal field, and exhibits a node at the resonance frequency, such that, for positive dispersion, the slope of the lineshape remains positive with respect to increasing frequency. See Section 4.2 for further examples. On the other hand, the complex S1 and S2 2D lineshapes exhibit a "phase twist" such that the real part of the 2D spectral peaks, while still largely absorptive, have some dispersive characteristics. This is due to the fact that the 2D Fourier transform of $\vec{E}_S(\tau_1, t)$ takes into account both the positive and negative values for τ_1 and t, such that Fourier transformation along either dimension separately yields an imaginary dispersive lineshape and subsequent 1D Fourier transformation along the opposite dimension mixes the dispersive lineshape into the total real 2D lineshape. The phase twist can be eliminated by correct addition of the real parts of the rephasing and non-rephasing 2D spectra [56].

2.2 Four-particle correlations and two-quantum techniques

In a single-pulse NMR measurement, the detected free induction decay is modified according the shielding of the magnetic dipole by the electron cloud and the coupling of the dipole to the dipolar field of another nucleus attached by a chemical bond. Based on this interpretation of a nuclear spin in a local magnetic field, it is straightforward to obtain molecular structural information when the sources of the local fields are limited. However, the spectra can become intractable for a large molecule. Although the one-quantum 2D FTNMR measurements described above are much more powerful than a simple single-pulse NMR measurement, since coupled nuclear spin coherences can be spread out along two frequency axes, the 2D spectra can still become too crowded for very large molecules like proteins and other polymers. However, in multiple-quantum NMR techniques, the response from multiple spins correlated through the aforementioned dipolar interactions is modulated by far fewer magnetic field contributions. Therefore, multiple-quantum techniques offer yet another degree of refinement by which signal contributions from congested one-quantum spectra can be isolated.

High-order nuclear spin coherences have been isolated and observed through multiple-quantum techniques [57, 58] used in 2D FTNMR spectroscopy. Multiple-quantum coherences do not radiate but they can be generated and probed in successive steps. First, each of the two RF fields, which may or may not be separated in time, induces a macroscopic spin coherence in the sample (a precession of the net magnetic moment) described quantum mechanically as a coherent superposition between the $|+\rangle$ and $|-\rangle$ spin states which evolves with the spin precession frequency ω_s. Neighboring spins are influenced by each other's magnetic moments through dipolar interactions, and the interaction strength is different when the precessing moments are aligned parallel or perpendicular to the direction between the two nuclei, as depicted in Fig. 2-3(a) and (b). The interaction – and the response of the precessing spins to it – thus has a component that oscillates at twice the precession frequency, $2\omega_s$. This

two-quantum coherent superposition of the $|\,-\,-\,\rangle$ and $|\,+\,+\,\rangle$ spin states has no net magnetic moment, and therefore is non-radiative and cannot be sensed directly. However a third field, phase-coherent with the first two fields and delayed by a temporal period τ_2, produces a new one-quantum spin coherence whose free induction decay is measured. The amplitude and phase of the resulting signal emitted during time t after the third field depend on the phase relationships between the RF fields and the one- and two-quantum coherences they generated. A 2D FT of the complex signal, $S(\tau_2, t)$, yields a 2D spectrum, $S(\omega_2, \omega)$, where groups of measured spin coherences (appearing along the emission frequency coordinate) sharing the same multiple-quantum coherence frequency along the ω_2 coordinate originate from equivalent pairs of nearby nuclei, and from this information the skeleton of even a large protein can be constructed. The multiple-quantum technique allows further simplification over conventional one-quantum spectra. Multiple-quantum techniques in NMR also permit the selection of correlations between spins on different molecules in a liquid mixture [59], providing information about liquid state structural dynamics [60].

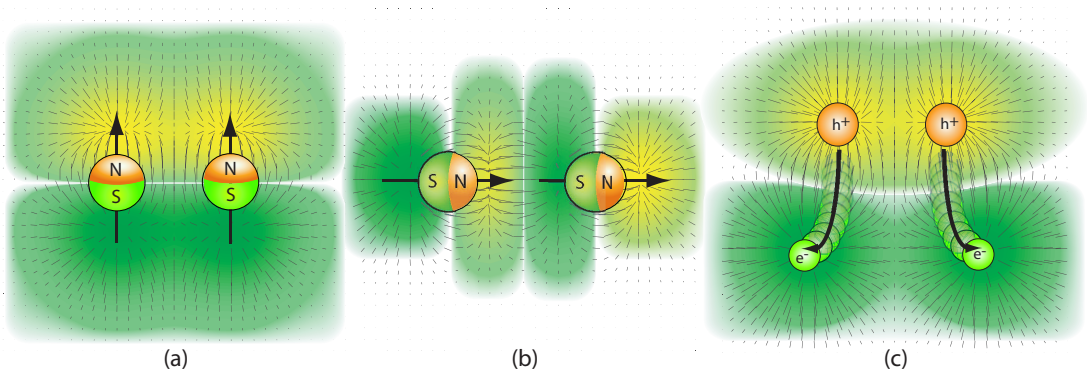

Figure 2-3: Interactions between two nuclear spins oriented (a) perpendicular and (b) parallel to the vector between the two nuclei. (c) Interactions between two electron-hole pairs.

A two-quantum 2D FTOPT signal can be isolated by again changing the time-ordering of the fields such that $\vec{E}_C$ arrives last at the sample. Analogous to the spin case, the first two optical fields, $\vec{E}_A$ and $\vec{E}_B$, induce coherent responses at the

exciton frequency, ω_e. The coherence can be described quantum mechanically as a superposition between the exciton wavefunction, $\mid X\rangle$, and ground state wavefunction, $\mid 0\rangle$, which specifies the absence of any electronic excitation in the system. Two electrons' trajectories during one-fourth of a coherence cycle are suggested by the black arrows in Fig. 2-3(c). As the nearby electrons move away from their parent holes, the screening forces provided by the holes are diminished and the electrons are more strongly repelled from each other. This occurs twice during each cycle, so the interparticle forces and the particle responses to them oscillate at $2\omega_e$.

Unlike the spin case, exciton correlations involve two pairs of real particles, and the holes also are alternately repelled and attracted at $2\omega_e$ as the screening between them provided by the electrons varies at that frequency. These correlated interactions may give rise to measurable changes in the exciton energy ε_e and dephasing rate γ_e. Nearby excitons also may interact through their locally radiated fields, further modulating each others' motions at $2\omega_e$.

Furthermore, the electron-hole pairs can adopt new time-averaged configurations, forming a biexciton state, $\mid X_2\rangle$, which is a bound quasiparticle formed from two exciton states, whose energy is minimized at a value lower than twice the exciton energy. As in the spin case, the biexciton-ground state coherence, and the other two-quantum coherences described above, which evolve during time period τ_2, are non-radiative. However, they can be detected through the action of a third field, $\vec{E}_C$, that induces transitions to one-quantum coherences whose signals, radiated during t, depend on the phase relationships between the first two and third fields.

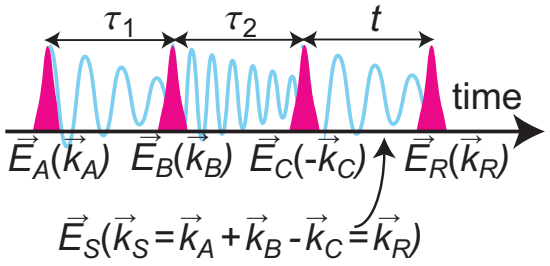

Figure 2-4: Pulse sequence used for two-quantum 2D FTOPT spectroscopy measurements.

The scenario described above shows how distinct biexciton and other two-quantum signals could be observed through an optical analog to two-quantum 2D FTNMR, i.e. two-quantum 2D FTOPT using the pulse sequence, also named S3, depicted in Fig. 2-4. In contrast to multiple-quantum nuclear spin coherences whose fundamental properties are well understood and whose measurement is conducted mainly to simplify complicated spectra, multiple-quantum optical coherences are of strong interest because they provide access to "dark" states whose properties and behavior are generally poorly understood and whose understanding may reveal much about high-order correlations in condensed matter, as described in Chapter 1.

However, performing these experiments in the optical regime requires that all the excitation fields and the reference field, used for interferometric detection which yields the full complex signal (rather than just its intensity), have controlled phase relationships. Combining this requirement with the key advantage of background-free detection of the full signal afforded by wavevector-matching of the optical excitation fields presents challenges because it means that phase relationships must be maintained among multiple noncollinear light fields that intersect at the sample. While two-quantum 2D FTIR spectroscopy of molecular vibrational overtones has been demonstrated in the infrared spectral region [61, 62, 63], where the wavelength is long enough that the phases of the IR fields in distinct beams can be maintained without extraordinary measures, a comparable measurement in the visible region is far more demanding. In the Chapter 3, I will describe an experimental technique for fully coherent 2D FTOPT spectroscopy, spatiotemporal pulse shaping, which addresses these challenges.

Chapter 3

Experimental methods

3.1 Introduction

Pulse shaping of ultrafast optical fields provides a unique and robust platform for performing many types of ultrafast spectroscopy measurements [43] and coherent control experiments [64]. In general, modulation of the temporal and spatial profile of a femtosecond laser pulse is achieved through filtering of the amplitudes and phases of its frequency and wavevector components. This calls for optical components that can discriminate between the different Fourier components of the pulse. Typical temporal pulse shaping setups involve diffractive or refractive elements, such as gratings or prisms, which can impart a different wavevector to each of the frequency components of the broadband laser pulse, and a focussing element, such as a lens or curved mirror, which focus the frequency components to different points in space at the focal plane. The phase and/or amplitude filtering element, called a spatial light modulator (SLM), is placed at the Fourier plane of the focusing element. The phase and amplitude profile imparted on the incoming waveform in frequency space, $E_{in}(\nu)$, can be treated mathematically as a transfer function, such that the output waveform is defined in the frequency domain as

$$E_{out}(\nu) = M(\nu)E_{in}(\nu) \tag{3.1}$$

or equivalently in the time domain, via the convolution theorem,

$$e_{out}(t) = m(t) * e_{in}(t). \tag{3.2}$$

SLMs with varied principles of operation have been devised [65]. The most ubiquitous are liquid crystal and acousto-optic based SLMs where the refractive index of the material can be controlled electrically [40, 66, 67] or by the oscillating mechanical pressure of a sound wave [68, 69], respectively. Mirror-based SLMs, where the positions of separate elements of the mirror are controlled through piezoelectric [70] or MEMS-based [71, 72] actuators, are also common.

Fully coherent 2D FTOPT afforded through spatiotemporal pulse shaping, which creates the four non-collinearly propagating optical fields from a single laser pulse in a single beam, and controls independently their interpulse delays, has both advantages and limitations. The key advantage for 2D FTOPT spectroscopy is that the phase relationships between features of the shaped waveform are passively stabilized through the use of common path optics, therefore eliminating the need to track or actively stabilize the phase offsets. Furthermore, as discussed below, the coherences detected during the first and second pulse delays, τ_1 and τ_2, respectively, are shifted into the rotating frame such that the reference frequency is defined by user. Also, the SLM can arbitrarily shape the phase and amplitude of the incoming fields.

The biggest limitation of spatiotemporal pulse shaping is that the output waveforms cannot be delayed beyond a certain maximum value in time. This is due to the fact that the phase profile applied in the frequency domain is not infinitely sampled. In other words, there is a minimum frequency sampling interval, $\delta\nu$, over which the applied phase is defined, which is determined in part by the frequency resolution achieved by the diffractive and refractive optical elements discussed above and the number and physical size of the SLM pixels. The maximum achievable time delay is easy to determine. By simple Fourier transform relationships, one can show that a temporal delay of the pulse envelope, τ, corresponds to a linear change in phase with respect to the frequency components of the pulse, $\phi(\nu)$, such that $\phi(\nu) = -2\pi(\nu - \nu_c)\tau$,

where ν_c is the carrier frequency of the pulse. This expression can be restated in terms of its slope, and therefore, the minimum frequency sampling interval, such that

$$\tau = -\frac{\delta\phi}{2\pi\delta\nu}. \tag{3.3}$$

Since the maximum phase change is 2π, the maximum time delay of the pulse envelope that can be achieved is simply $1/\delta\nu$. Furthermore, the intensity of the pulse will be modulated as the pulse is delayed, which imposes a minimum linewidth that will be convolved with the linewidth of the measured spectral features along the ω_1 and ω_2 coordinates. However, this distortion can be decoupled from the measurement as discussed in Section 3.3.3.

Since many of the experimental details regarding spatiotemporal pulse shaping, such as frequency-to-pixel calibration, phase change versus applied voltage calibration, and output waveform characterization have been published elsewhere [43, 73, 74], in this chapter I will discuss only the features of spatiotemporal pulse shaping that are directly relevant to 2D FTOPT measurements in addition to the optical setup.

3.2 The Multidimensional Optical Spectrometer

The optical components for the Multidimensional Optical Spectrometer, shown in Fig. 3-1, can be divided into three main parts: diffractive beam shaping, spatiotemporal pulse shaping, and spectral interferometry of the signal field. The main optical elements are summarized here. Diffractive beam-shaping and diffraction-based pulse shaping are discussed in further detail in Sections 3.2.1 and 3.2.2, respectively. As shown in Fig. 3-1, the beams containing the three pulsed fields, $\vec{E}_A$, $\vec{E}_B$ and $\vec{E}_C$, used to excite the coherent third order response in the sample and the reference field, $\vec{E}_R$, used to interferometrically detect the resulting the signal, are generated, via diffractive beam shaping, from a single pulse in a single Gaussian beam from an unamplified Ti:sapphire laser with an energy of 3 nJ/pulse and a beam diameter of approximately 2 mm. The static diffractive optic has a square lattice pattern which

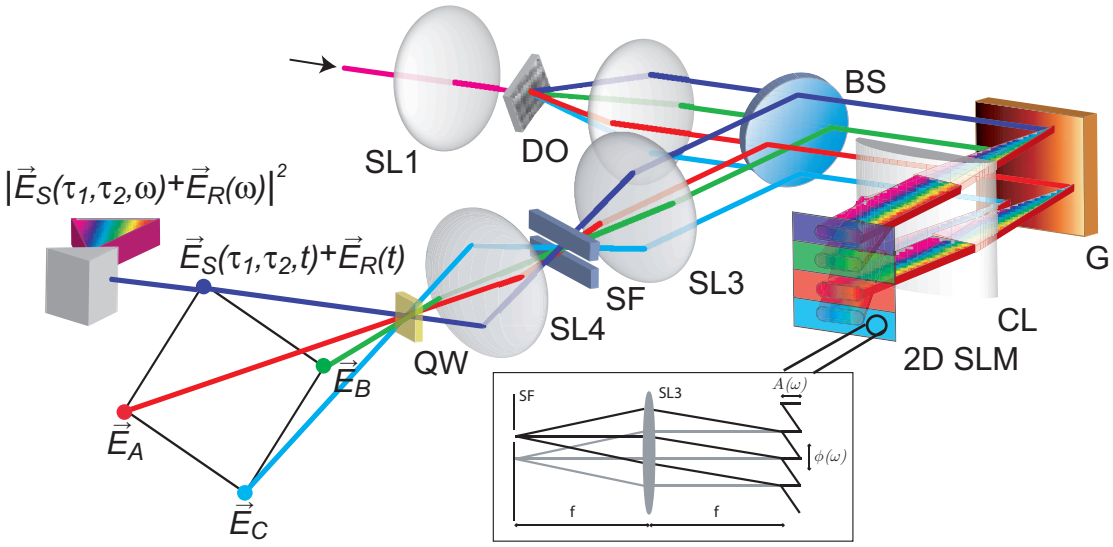

Figure 3-1: Components of the Multidimensional Optical Spectrometer. The labeled components are as follows: (SL1) 10 cm focal length spherical lens, (DO) static diffractive optic, (BS) 50/50 beamsplitter, (G) gold 1400 grooves/mm diffraction grating, (CL) 12.5 cm focal length cylindrical lens, (2D SLM) two-dimensional liquid spatial light modulator, Hamamatsu PAL-SLM X8267, (SL3) 80 cm focal length spherical lens, (SF) spatial filter, and (SL4) 15 cm focal length spherical lens. The optics are arranged in an imaging geometry (see main text). The inset depicts the phase pattern used for diffraction-based pulse shaping.

diffracts most of the input laser beam power into four beams, which pass through a beamsplitter and into the pulse shaper consisting of a grating, cylindrical lens and 2D liquid crystal spatial light modulator. The frequency components of the four beams are dispersed horizontally across four distinct regions of the SLM where their amplitudes and phases are controlled through diffraction, as detailed below. Then the frequency components are recombined at the grating, yielding the four fully phase-coherent, temporally shaped fields, $\vec{E}_A$, $\vec{E}_B$, $\vec{E}_C$ and $\vec{E}_R$. The fields are reflected by the beamsplitter and focused through a spatial filter and then into the sample. The signal emerges from the sample in the wavevector-matching direction, collinear with $\vec{E}_R$, and the superposed fields are directed into a spectrometer. The amplitude and phase of the signal are then obtained through spectral interferometry [75].

One drawback of this setup is that much of the input laser beam power is lost. Approximately 50% of the beam power is lost to higher diffraction orders in the diffractive beam shaping portion of the apparatus. Another 75% is lost because of two passes through the 50/50 beamsplitter. The diffraction grating is approximately 90% efficient and 80% of the beam power is retained after the spatial filter. Therefore, the overall efficiency of the setup is approximately 10%. Improvement has been demonstrated by taking advantage of the slight displacements of the shaped pulses from their incident beam paths as they emerge from the pulse shaper. The beamsplitter can be eliminated, the incident beams sent directly into the pulse shaper, and the displaced beams directed to a high reflector and into the rest of the setup. In this manner the 75% loss due to the beamsplitter is avoided.

3.2.1 Diffractive beam shaping

Diffractive beam shaping is depicted in Fig. 3-2(a). The laser output is focused into a static diffractive optic using a 10 cm spherical lens. The diffractive optic was constructed by mounting back-to-back two separate transmission gratings of equal groove spacing which could be rotated independently. The net result is a diffractive optic that has a square lattice pattern with a feature spacing of 9 μm and a feature depth of 400 nm which permits the most efficient diffraction of the beam into the

±1 diffraction orders. A second 10 cm lens collimates the diffracted beams so that the final beam pattern consists of four beams arranged on the corners of a square approximately 1 cm on a side. This is the familiar "BOXCARS" geometry used in many FWM experiments. The entire BOXCARS beam pattern is rotated approximately 25° so that after diffraction by the grating, none of the dispersed frequency components belonging to the four fields are overlapped on the surface of the 2D SLM. Approximately 50% of the input beam power is dispersed into the four major 1^{st} order diffracted beams. The zeroth and higher diffraction orders are blocked after the 2D pulse shaper.

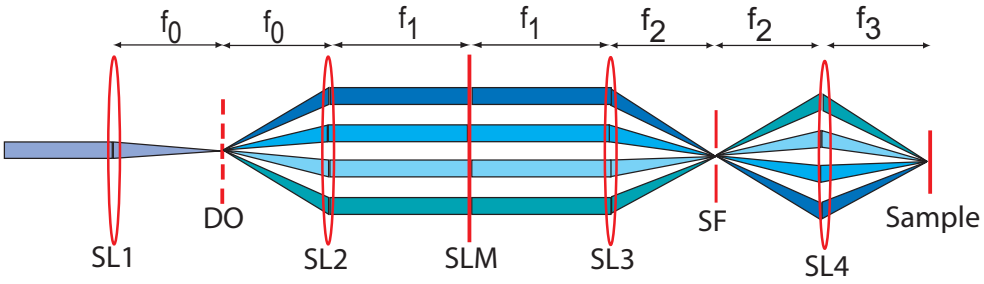

(a) Diffractive beam shaping

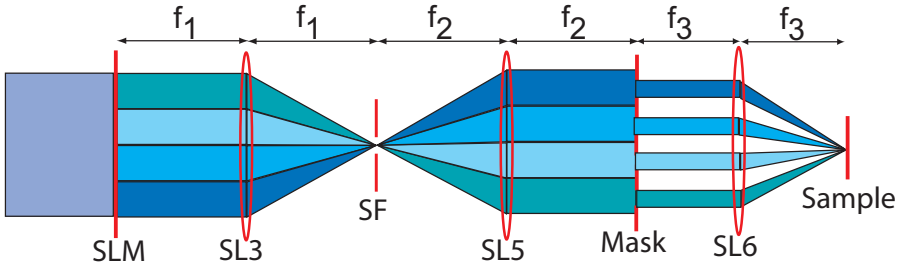

(b) Real-space beam shaping

Figure 3-2: Diffractive (a) versus real-space (b) beam shaping in an imaging geometry. The optical elements depicted in (a) are equivalent to the elements with the same labels in Fig. 3-1. In (b), the spherical lens, SL5, is involved in imaging the 2D SLM phase pattern to the spatial mask (see main text).

Spatiotemporal pulse shaping was first used for phase-coherent FWM without a diffractive optic to separate the incident light into four beams [43], which is depicted in Fig. 3-2(b). Instead, a single beam was sent into the pulse shaper, and four distinct regions of the SLM were used to produce four shaped outputs. These were incident onto a spatial mask with four holes placed at the corners of a square pattern, so four

beams, one from each distinct region of the SLM, emerged for use in the BOXCARS geometry. However, the spatial filtering by the holes blocked the great majority of the light, yielding poor throughput, and diffraction and scattering off of the edges of the holes added significantly to experimental noise. Beam shaping by diffraction increases the efficiency of the setup by an order of magnitude, produces outputs with Gaussian spatial profiles, and minimizes cross-talk between pulses generated from nearby regions on the SLM or from aperture edges. The beam pattern can also be easily reconfigured if the static diffractive optic is replaced with an adaptive element, such as another 2D SLM. Any pulse-front tilt imparted to the optical pulses by the diffractive element is eliminated at the sample if the beams are properly imaged from their point of generation to the sample [76].

3.2.2 Diffraction-based spatiotemporal pulse shaping using a 2D SLM

The amplitudes and phases of the frequency components of the four beams dispersed horizontally across four distinct vertical regions of the SLM are controlled through diffraction [77]. The SLM is ordinarily a phase-only device, that is, the liquid crystal rotation at any pixel is used to shift the phase of light that arrives there. Diffraction-based shaping allows control of the amplitudes as well as the phases of the separated spectral components. This is achieved with a 2D SLM by constructing a sawtooth grating pattern in the vertical direction with amplitude $A(\omega)$, spatial phase $\phi(\omega)$, and period d, (see Fig. 3-3(b) and inset of Fig. 3-1) for each of the horizontally separated frequency components of each of the four beams. The amplitude and phase of the diffracted light for each selected frequency component, $E(\omega)$, are controlled by the amplitude and spatial phase of the corresponding sawtooth grating pattern, such that

$$E(\omega) = \exp[i2\pi\phi(\omega)]\mathrm{sinc}[\pi(1 - A(\omega))] \tag{3.4}$$

where $\phi(\omega) = \dfrac{\Delta}{d}$ and Δ is the vertical displacement of the sawtooth grating pattern. The 2D phase pattern on the SLM illustrated in Fig. 3-3(a) shows the sawtooth

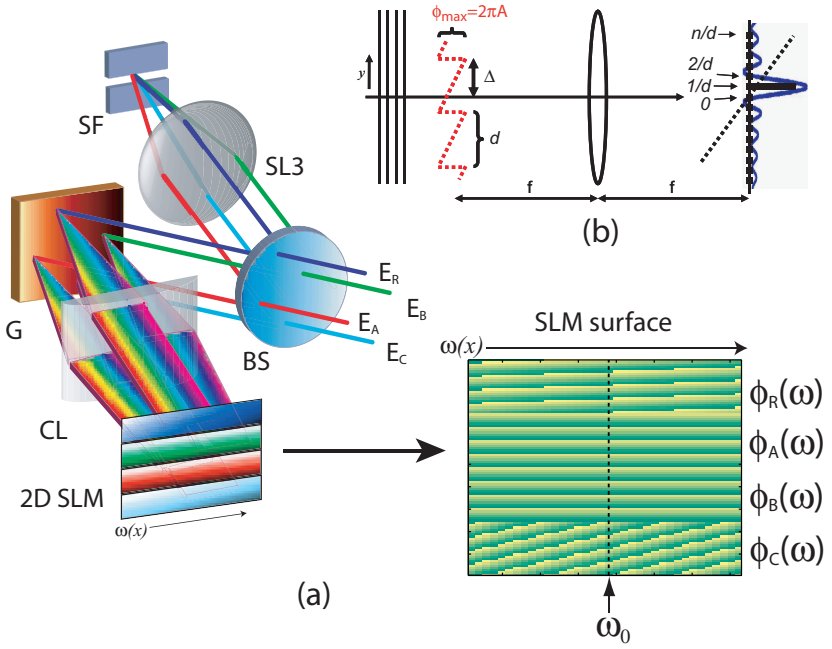

Figure 3-3: Illustration of the spatiotemporal pulse shaper operating in diffraction mode. The separated frequency components of the broadband pulses are projected onto the surface of the 2D SLM, shown in (a), effectively dividing it into four distinct horizontal regions. Within each region, each dispersed frequency component is diffracted by a sawtooth phase pattern, which is shown in (b) as a red dashed line. The phase for one selected frequency component is kept fixed for all four regions, which defines the reference frequency ω_0 (see the discussion in Section 3.3.1).

grating pattern and its spatial phase for each spectral component of each pulse. A phase that increases (decreases) linearly as a function of frequency yields a negative (positive) pulse envelope temporal delay. In the example depicted here, fields $\vec{E}_A$ and $\vec{E}_B$ are unmodulated, i.e. all their frequency components have the same phase, yielding pulses that are unshifted from $t = 0$. Fields $\vec{E}_C$ and $\vec{E}_R$ are temporally shifted from $t = 0$ by different amounts. Clearly, the SLM can be used to control the temporal delays of any of the pulses without the need for delay stages or variable-thickness elements (wedges) in the beam paths.

Recalling Eqn. 3.3, it follows that the minimum time delay achieved for the output waveforms is related to the minimum phase change, which depends on the how many independent phase values can be distinguished by the SLM. In the case of diffraction-based pulse shaping, the minimum phase change is the minimum vertical displacement of the sawtooth grating pattern. This pattern is defined in terms of the number of SLM pixels used to define d, the sawtooth period, and therefore the sampling interval for the sawtooth grating pattern is one SLM pixel. For the PAL-SLM X8267, which has 768 pixels along its vertical dimension, typically 12 pixels are used to define d, therefore the minimum phase change is $2\pi\frac{1}{12}$ radians. For the specific grating-lens pair used in this optical setup, $\delta\nu$=0.05 THz. Thus the minimum time delay is 1.67 ps which is far too large a step size for most ultrafast spectroscopy measurements. What is done in practice is that the linear phase profile (with respect to frequency) is oversampled in the frequency domain, such that several columns of pixels are binned together and the respective sawtooth phase profiles have the same vertical displacement. With respect to Eqn. 3.3, the binning of columns of pixels increases the frequency sampling interval, which in turn, allows a smaller minimum time delay for a fixed minimum phase change. For example, if the columns of pixels are binned into 4 groups of 192 pixels each, then the minimum time delay is approximately 9 fs.

Diffraction-based pulse shaping also discriminates against the pulse replica created due to imperfections in the pixel shape of the SLM which mar the shaped output delivered by standard reflection-based pulse shaping [41]. After the spectral components

have been diffracted from the SLM and recombined into the user-defined temporal waveforms, the focusing of the beams through the spatial filter eliminates these replicas and the de-selected frequency components from the final waveforms used for the experiment. However, the variation of the shaped output as a function of delay must be determined carefully prior to successful spectroscopic measurements. The main distortion is the decrease, or "roll-off" in the intensity of the pulse as it is delayed, which is due to the pixelated nature of the SLM and the smooth shape of the pixels [73, 74]. Pulse intensity roll-off is discussed in more detail in Section 3.3.3.

3.3 2D FTOPT spectroscopy using SLM-delayed pulses

Here I will discuss in detail several of the advantages, such as passive phase stability, rotating frame detection, and phase cycling and phasing of the signal, and limitations, such as pulse intensity roll-off, of the spatiotemporal pulse shaping technique in relation to 2D FTOPT spectroscopy.

3.3.1 Rotating frame detection

The pulse shaper permits the relative delay times between pulses to be varied while maintaining the relative optical phase relationships constant. This is accomplished by selecting a reference frequency ω_0 within the spectral bandwidths of the pulses and then varying the slope $\frac{d\phi}{d\omega}$ of the linear phase sweep in the SLM pixel pattern to change the relative pulse envelope delays while keeping the phase of the selected reference frequency constant. Thus, the amplitude and phase of the waveform generated by the SLM for one of the incident pulses can be written in the frequency domain and time domain as

$$E(\omega) = A(\omega)\exp[i(\omega - \omega_0)\tau - i\phi^{(0)}] \tag{3.5}$$
$$E(t) = a(t - \tau)\exp[-i\omega_0 t - i\phi^{(0)}]$$

where $A(\omega)$ and $a(t)$ are related by Fourier transformation, and $\phi^{(0)}$ is the optical phase, which describes the offset of the carrier wave ($\exp[-i\omega_0 t]$) from the pulse envelope maximum ($a(t)$) at $t = 0$. Note that for SLM-delayed pulses, the optical phase at the carrier frequency ω_0 remains constant for all delays, τ. In contrast, the arrival time of the pulse envelope at the sample controlled through the mechanical motion of a translational delay stage is accompanied by an uncontrolled variation in the optical phase since a reference frequency cannot be specified. Equation 3.6 gives the amplitude and phase of a "path-length" delayed pulse in the frequency and time domain.

$$\begin{aligned} E(\omega) &= A(\omega)\exp[i\omega\tau - i\phi^{(0)}] \\ E(t) &= a(t-\tau)\exp[-i\omega_0(t-\tau) - i\phi^{(0)}] \end{aligned} \tag{3.6}$$

In contrast to an SLM-delayed pulse (Eqn. 3.5), the path-length delayed pulse accumulates a phase of $\omega_0\tau$ with respect to delay.

The method by which the excitation pulses are delayed has a profound effect on the signal field, which is centered at the resonance frequency for the transition ω_{ge} and which is generated primarily through the action of incident field components near that frequency. For SLM-delayed pulses, as the relative pulse delays are varied, the relative phases at ω_0 remain constant and the relative phases, and thus the signal field, at ω_{ge} shift slightly, proportional to the frequency difference $\omega_{ge} - \omega_0$. Thus the phase of the signal field shifts only gradually as a function of pulse delay, as depicted in Fig. 3-4(a), and the phase behavior of the signal can be mapped out using rather coarse time delay steps. This is precisely analogous to rotating frame detection in NMR [78].

In contrast, when an incident pulse is delayed by a translational delay stage or a variable-thickness wedge in its path, as is commonly the case, the optical phase of the pulse, and therefore of the signal field, is swept through an entire 2π cycle each time the delay is varied by just one optical period as depicted in 3-4(b). In this case data must be recorded at many delay points within a single optical period in order

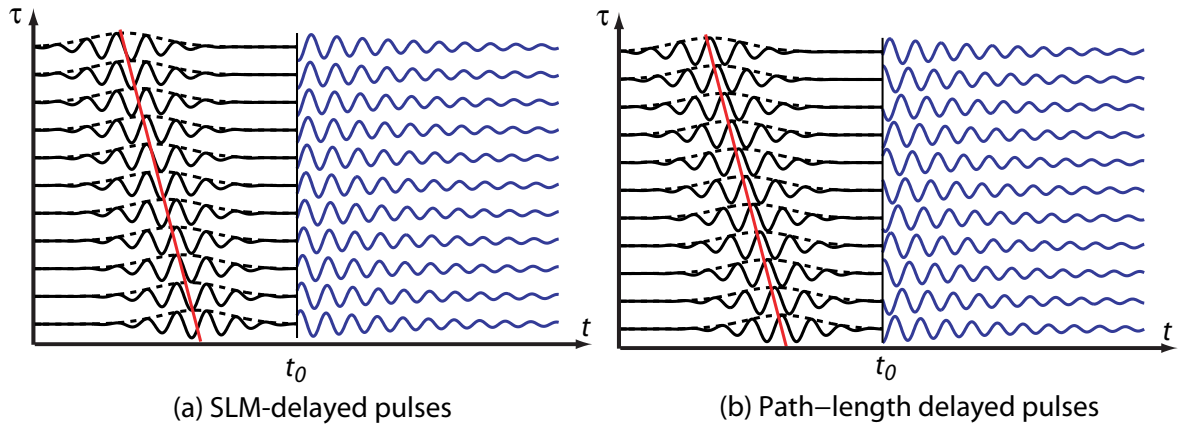

Figure 3-4: Comparison of a generalized third order polarization $P^{(3)}(\tau, t)$ that radiates coherent signal at emission frequency ω_{ge} from a sample when excited by (a) SLM vs. (b) "path-length" delayed pulsed optical fields as one of the relative pulse delays τ is varied. In each case, $P^{(3)}$ (blue, solid) is shown relative to an arbitrarily chosen reference time t_0 and the Gaussian envelope (black, dashed) and field oscillations at the experimentally set reference frequency ω_0 (black, solid) are shown for a variably delayed pulse. The red line connects the maxima of the delayed pulse envelopes. In (a), the carrier phase of the incident pulse remains constant, and the phase of the signal field shifts slowly, proportional to the small frequency difference $\omega_{ge} - \omega_0$, as a function of τ. On the other hand, in (b), the carrier phase shifts a full cycle – causing the signal phase to do essentially the same – each time the envelope delay moves by just one wavelength. The "rotating frame" measurement (a) is preferred since the complete phase behavior of the signal field can be determined accurately with very coarse time steps relative to the optical carrier cycle.

to elucidate the signal phase behavior.

The spatiotemporal pulse shaping approach is naturally compatible with phase-coherent spectroscopy. In practice, for 2D FTOPT with rotating frame detection, the selected carrier frequency ω_0 has its phase held constant in all the beams by keeping all four sawtooth grating patterns at that frequency identical to each other. Specifically, for the pixel pattern shown in Fig. 3-3, fields $\vec{E}_A$ and $\vec{E}_B$ are time-coincident, and the other two fields, $\vec{E}_C$ and $\vec{E}_R$, are delayed in time by different amounts (with the phases at carrier frequency ω_0 held constant).

Figure 3-5 shows how rotating frame detection affects the observed peak positions of the biexciton coherence features in the two-quantum measurements discussed in Section 5.2.2. As the time interval between two pulses is increased, the phase dif-

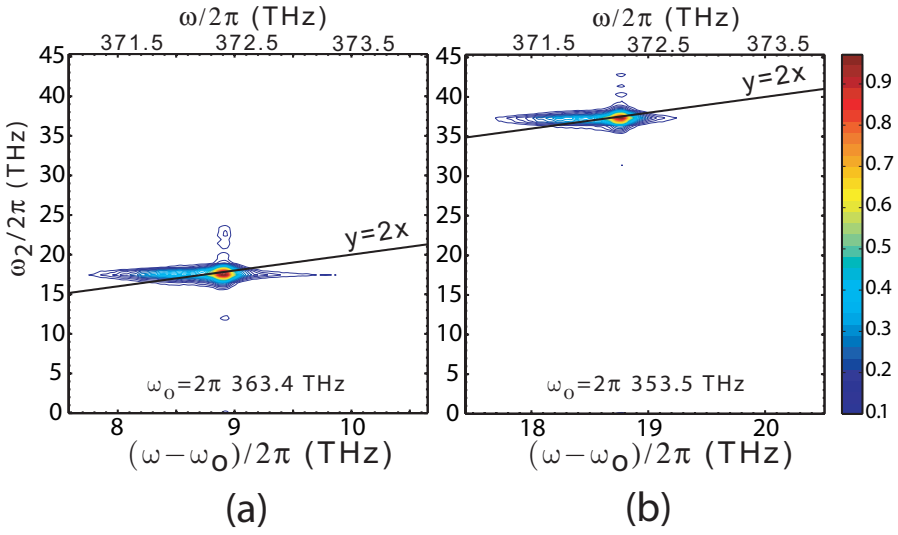

Figure 3-5: Two-quantum 2D FTOPT surfaces generated using linearly polarized excitation pulses in which the reference frequency, ω_0, was changed from (a) 363.4 THz to (b) 353.5 THz. The blue line plotted at $\omega_2 = 2(\omega - \omega_0)$ is shown for reference. Changing the reference frequency by 10 THz caused the position of the biexciton coherence to shift by 20 THz along the ω_2 axis.

ference at any emission frequency ω increases proportional to $\omega - \omega_0$, and signals that depend on such a phase difference show oscillations at that difference frequency. During the two-quantum coherence period, τ_2, the system undergoes coherent oscillations at a frequency which is nearly twice that of the exciton resonance, and the

two-quantum signals depend on the phase difference $2\omega - 2\omega_0$. As the two-quantum coherence time interval is increased, the two-quantum signals show oscillations at that difference frequency. Therefore if the reference frequency is changed by an amount $\Delta\omega_0$, the frequencies at which one-quantum signals appear are shifted by $\Delta\omega_0$ while two-quantum signals are shifted by $2\Delta\omega_0$. Surfaces from different two-quantum 2D FTOPT measurements using linearly polarized excitation pulses are shown in Fig. 3-5 with two different reference frequencies: 363.40 THz and 353.50 THz. The prominent biexciton coherence feature remains at the same absolute emission frequency, ω, plotted on the upper axis, but is shifted along ω_2 depending on the reference frequency selected. In Fig. 3-5(a)/(b), where the reference frequency is 9 THz/19 THz lower than the heavy-hole exciton resonance, i.e. see the $\omega - \omega_0$ axis at the bottom of the plots, the biexciton feature appears at approximately 18 THz/38 THz along the ω_2 axis. It is clear that the main features, resulting from biexciton coherences, shift along the vertical axis by twice the change in the reference frequency and along the horizontal axis by exactly the change in the reference frequency.

The reference frequency of the shaped pulse is user-defined but relies on an accurate calibration of the frequency dispersion of the spectral components of the pulse across the SLM surface. Furthermore, the dispersion of each individual pulse across the SLM surface may be slightly different due to off-axis spherical aberrations introduced by the cylindrical lens in the pulse shaping apparatus. The reference frequency can be confirmed by comparing measurements of the coherent oscillation frequency that evolved during the first time period, τ_1, where the different shaped pulses controlled by phase patterns on different vertical regions of the SLM are used as the first excitation field, to the absorption spectrum of the sample. This is discussed in further detail in connection with 2D FTOPT measurements on semiconductor QWs and Rb vapor in Chapters 5 and 6, respectively.

3.3.2 Phase stability

A tremendous benefit of the Multidimensional Optical Spectrometer apparatus is that all beams propagate through the same set of optics, such that the relative path

length traversed by all beams is interferometrically stable. Ordinarily, small path length variations on the order of the wavelength of the laser pulses cause phase shifts between the excitation fields, which will be imparted to the induced $\chi^{(3)}$ signal, which, in turn, causes the interference fringes between the signal and reference fields used for interferometric detections to shift significantly, introducing crippling distortions in the measured signals. The common path geometry used here makes the apparatus rather insensitive to vibrations in the mounts and holders for each optic. Only relatively high-order vibrational modes, for instance the "warping" of a mirror or lens, or turbulence in the air, are capable of introducing phase shifts between the beams. Stability measurements between a nonlinear signal and the reference are shown in Fig. 3-6. The RMS stability over 8 hours is only 1.5%, or $\lambda/67$, even though no efforts were made to use especially sturdy optical mounts and even though the apparatus was not contained within a box to minimize phase shifts due to air currents.

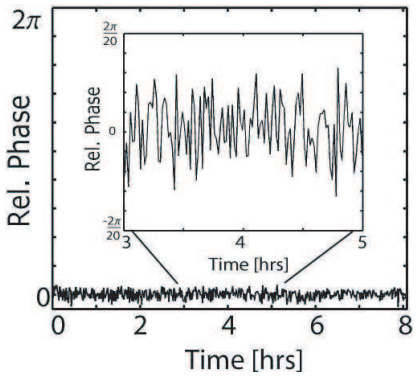

Figure 3-6: Measurement of the phase stability between a nonlinear signal from Rb atoms and the reference field over 8 hours, indicating a root-mean square phase stability of $\lambda/67$.

3.3.3 Pulse intensity roll-off correction

A significant pulse distortion that occurs in temporal pulse shaping is that the intensity of the pulse is modulated with respect to delay. This phenomenon can be explained by considering the pixelated nature of the device and the spectral resolution of the grating-lens pair. As discussed in Section 3.1, the phase profile applied to

the spectral components of the broadband pulse is sampled in frequency space, such that the transfer function defined in Eqn. 3.1 takes the form

$$M(\Omega) = \exp(-\Omega^2/\delta\Omega^2) * \sum_{n=-N/2}^{N/2-1} \mathrm{squ}(\frac{\Omega - \Omega_n}{\Delta\Omega}) A_n \exp(i\phi_n) \tag{3.7}$$

where Ω is the detuning from the frequency at the center pixel of the SLM, ν_o, i.e. $\Omega \equiv \nu - \nu_o$, N is the number of SLM pixels, A_n and ϕ_n are the amplitude and phase modulation, respectively, applied by each pixel, $\delta\Omega$ is the spectral resolution, and $\Delta\Omega$ is the frequency span per pixel. Note that Eqn. 3.7 assumes that the frequency dispersion produced by the grating-lens pair used in the optical setup presented here is linear in space, which is generally not the case, but valid for a small spectral range. Equation 3.7 also assumes that the spatial profile of a given spectral component, $S(x)$, can be approximated as Gaussian, such that $S(x) = \exp(-x^2/\delta x^2)$ where δx is the focal spot size. This spatial profile can be translated to a Gaussian in the spectral domain through a proportionality of the pixel size, Δx, and frequency span per pixel, i.e. $\dfrac{\delta\Omega}{\Delta\Omega} = \dfrac{\delta x}{\Delta x}$. Fourier transformation of the transfer function to the time domain gives

$$m(t) = \exp(-\pi^2\delta\Omega^2 t^2)\mathrm{sinc}(\pi\Delta\Omega t) \sum_{n=-N/2}^{N/2-1} A_n \exp[i(2\pi\nu_n t + \phi_n)]. \tag{3.8}$$

In Eqn. 3.8, the sinc term is the Fourier transformation of the square pixel shape, where the width of the sinc function is inversely proportional to the pixel separation Δx, or equivalently, $\Delta\Omega$. The Gaussian term results from the finite spectral resolution of the grating-lens pair, where the width of the Gaussian function is inversely proportional to the spectral resolution $\Delta\Omega$. Collectively, the product of the Gaussian and sinc terms is known as the total time window. The measured pulse intensity roll-off and the predicted time window for the spatiotemporal pulse shaping apparatus is shown are Fig. 3-7(a). The measured roll-off function does not follow the predicted time window exactly because of modulator replica that arise since the phase profiles applied by the liquid crystal SLM have a smooth shape, i.e. the pixels do not have

sharp edges, which was explained previously [73].

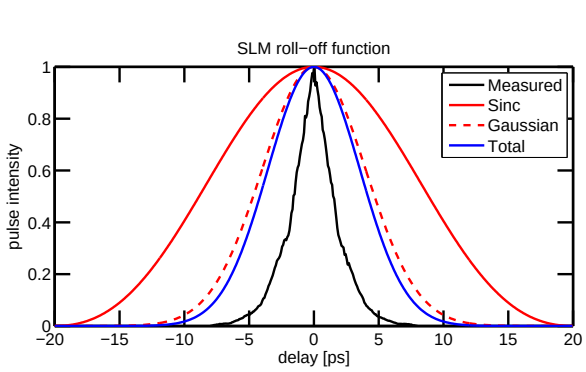

(a) SLM roll-off function

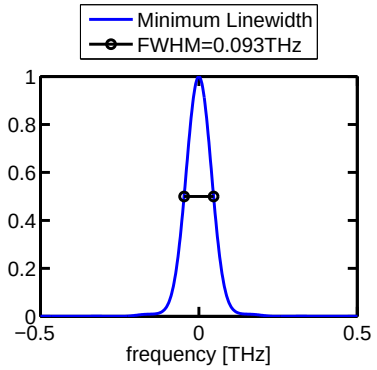

(b) Fourier transform of roll-off

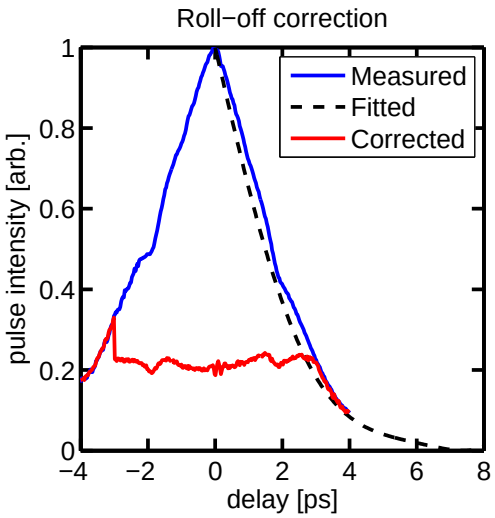

(c) Roll-off correction

Figure 3-7: The measured pulse intensity roll-off is compared to the sinc, Gaussian and total time window functions in (a) where $\Delta\Omega$=0.05 THz and $\delta\Omega$=0.04 THz, while (b) shows the Fourier transform of the roll-off function (fitted to a polynomial) which gives a minimum linewidth of 0.09 THz

The 2D FTOPT signals measured as a function of the interpulse delays that are controlled by the SLM will be convolved with the linewidth of the roll-off function in the frequency domain, which is shown in Fig. 3-7(b). The pulse intensity roll-off can be compensated by designating an upper bound on the amplitude of the output waveform and then modulating the amplitude of the output waveform by changing the overall amplitude of the sawtooth phase profile as the pulse is delayed. This is depicted in Fig. 3-7(c). The measured roll-off function is fit to a polynomial

function. Then, if a desired pulse delay is within the designated range, the amplitude of the sawtooth phase pattern is decreased for every frequency component of the pulse according to the fit function. However, much of the pulse energy is lost by this method. Therefore, another way to compensate for the pulse intensity roll-off would be to characterize it before the 2D FTOPT measurement and then divide it from the resulting signal trace.

3.3.4 Phase cycling

A familiar method in 2D FTNMR, phase cycling, involves the shifting the phase of one or more fields by a known amount, typically π, and subtraction of the resulting signals to eliminate unwanted signal components and selectively enhance desired signal components. The method can be adapted to 2D FTOPT and is based on the fact that the phase of the desired signal can be shifted by a specified amount $\Delta\phi_S$ through corresponding shifts introduced into the optical phases of any of the three excitation fields: $\Delta\phi_S = \Delta\phi_A + \Delta\phi_B - \Delta\phi_C$. Most of the unwanted signal contributions, however, depend only on the phase of one field. Therefore, shifting the phase of any incident field by π (accomplished by shifting the sawtooth grating pattern for every frequency component by half the grating period) and subtraction of the resulting signals yields addition of the desired signal but subtraction of signal contributions that do not depend on the phase-shifted field.

This method is especially useful with spectrally resolved detection of the spatially overlapped (but temporally delayed) signal and reference fields which are superposed at the image plane of a spectrometer, i.e. spectral interferometry. Spectral interferometry measures the spectral fringes produced by the superposition of the signal and reference fields at the image plane of a spectrometer, such that the spectral fringes are proportional to the time delay between the signal and reference fields. Stray light or other unwanted signal components can also interfere with the signal in the spectrometer, creating multiple sets of spectral fringes and complicating the analysis of the signal. Spectral fringes caused by stray light can obscure the signal even if the stray light is weak since the energy of 2D FTOPT signal fields is typically less than

1/1000 of the energy of the excitation fields.

In the case where there is no stray light, the intensity $I(\omega)$ recorded by the spectrometer is given by

$$\begin{aligned} I(\omega) &\propto |E_S(\omega) + E_R(\omega)|^2 \\ &\approx A_S(\omega)^2 + A_R(\omega)^2 + 2 * A_S(\omega)A_R(\omega)\cos[\phi_R(\omega) - \phi_S(\omega)] \end{aligned} \tag{3.9}$$

where $E(\omega) = A(\omega)e^{i\phi}$ such that ϕ is the optical phase. Many additional cross terms will be produced in the presence of stray light (see Eqn. 3.10), but none of them will have the same phase dependence on the three excitation fields and reference field as the desired cross term in Eqn. 3.9.

$$\begin{aligned} I(\omega;\phi_A,\phi_B,\phi_C,\phi_R) \propto &|A_S(\omega)e^{i\phi_S} + A_R(\omega)e^{i\phi_R} \\ &+ A_A(\omega)e^{i\phi_A} + A_B(\omega)e^{i\phi_B} + A_C(\omega)e^{i\phi_C}|^2 \end{aligned} \tag{3.10}$$

Phase cycling of the signal can be accomplished by performing multiple measurements where the phase of excitation fields or reference field is shifted by π and then combining the measurements such that signal components related to the unwanted cross terms stated in Eqn. 3.10 are discarded. This is done in three steps that require a total of eight measurements. In the first step, all terms not dependent upon the phase of field $\vec{E}_A$ are eliminated. This is then repeated with two more measurements to eliminate all terms not dependent upon the phase of field $\vec{E}_B$, and then four more measurements to eliminate all terms not dependent upon $\vec{E}_C$, which then isolates the term of interest. This set of eight measurements is written as

$$\begin{aligned} I_{total}(\omega;\phi_A,\phi_B,\phi_C,\phi_R) = &I(\omega;\phi_A,\phi_B,\phi_C,\phi_R) \\ &- I(\omega;\phi_A+\pi,\phi_B,\phi_C,\phi_R) - I(\omega;\phi_A,\phi_B+\pi,\phi_C,\phi_R) \\ &- I(\omega;\phi_A,\phi_B,\phi_C+\pi,\phi_R) + I(\omega;\phi_A+\pi,\phi_B+\pi,\phi_C,\phi_R) \\ &+ I(\omega;\phi_A+\pi,\phi_B,\phi_C+\pi,\phi_R) + I(\omega;\phi_A,\phi_B+\pi,\phi_C+\pi,\phi_R) \\ &- I(\omega;\phi_A+\pi,\phi_B+\pi,\phi_C+\pi,\phi_R) \end{aligned} \tag{3.11}$$

and yields only the cross term described in Eqn. 3.9 with its magnitude increased eight-fold.

3.3.5 Phasing the complex 2D FTOPT signal

Determining the correct sign for the complex 2D lineshapes of one-quantum measurements is usually performed by comparing their projection to the emission axis to a separate pump-probe experiment via the projection-slice theorem [55]. Some other methods of phasing one-quantum 2D FTOPT lineshapes were explained recently [79, 80]. Here I show how the spatiotemporal pulse shaper can be used to determine the phase offset between the signal and reference fields by measuring the spectral interferogram of the temporally overlapping reference field and time-zero signal field.

The SLM-generated excitation and reference fields are written in the frequency domain in Eqn. 3.5. For this example, assume that the signal field can be written in the frequency domain as a Lorentzian with center frequency ω_e and linewidth γ_e. See Eqn. 3.12. Just as discussed in the phase cycling example, the phase of the signal field depends on the phase of excitation fields.

$$E_S(\omega) \propto ie^{(i(\omega_e-\omega_0)\tau_1-\gamma_e\tau_1-\Gamma_r\tau_2)}\frac{\frac{\gamma_e}{2}}{(\omega-\omega_e)^2+(\frac{\gamma_e}{2})^2} \times \exp[-i(\Delta\phi_A+\Delta\phi_B-\Delta\phi_C)] \tag{3.12}$$

The measured spectral interferogram is described by Eqn. 3.9. Inserting Eqn. 3.12 for the time-zero signal field (i.e. $\tau_1 = \tau_2 = 0$) and Eqn. 3.5 for the reference field gives

$$\begin{aligned} S(\omega) &\propto \cos[\Delta\phi_R - (\Delta\phi_A+\Delta\phi_B-\Delta\phi_C)] \\ &= \cos[\Delta\Phi] \end{aligned} \tag{3.13}$$

where $\Delta\Phi$ is the phase offset. The phase offset can be determined by varying the optical phase of one of the excitation fields or reference field using the SLM such that

the interferogram at a signal emission frequency can be written as

$$S(\delta;\omega_e) = \cos[\Delta\Phi - \delta] \tag{3.14}$$

and this trace can be fitted in order to determine the phase offset. This procedure is discussed in more detail in Section 5.2. To correctly phase the 2D spectrum, the determined phase offset value can be added as a phase factor to one of the excitation pulses during the experiment, or multiplied with the entire data set after the measurement.

3.4 Conclusions

In many respects, spatiotemporal pulse shaping is able to integrate key elements of multidimensional NMR spectroscopy, including complex waveform generation, phase cycling, and rotating frame signal collection, into 2D FTOPT spectroscopy without compromising the wavevector-based signal selectivity of the latter. The absence of active optical elements besides the spatiotemporal pulse shaper and the need for few optical elements altogether, as well as the interferometric stability inherent in the common-path optical apparatus, permit extremely robust operation that should be possible in nonideal environments including commercial instruments outside a laser laboratory. The advantages of spatiotemporal pulse shaping technique outweigh its limitations since one-quantum 2D FTOPT measurements can be performed successfully and two-quantum measurements are also possible. Such measurements on semiconductor QWs and Rb vapor are shown in Chapters 5 and 6.

Chapter 4

Numerical models of exciton interactions

4.1 Introduction

Exciton correlation dynamics are described by the equations of motion for electron and hole wavefunctions governed by a multi-electron Hamiltonian which includes Coulomb correlations between the charged carriers. The equations of motion can be constructed according to different formalisms, namely, the nonlinear exciton equations [81, 82] or a dynamics-controlled truncation scheme [83, 84] for the semiconductor Bloch equations [85]. While the full numerical calculations based on microscopic models are necessary to provide a first-principles explanation for exciton coupling and higher-order correlations, phenomenological models have been used successfully to explain the spectral and temporal features in ultrafast four-wave mixing [20, 18, 21, 22, 86] and one-quantum 2D FTOPT [87, 88] measurements on semiconductor quantum wells. In fact, direct analogies can be drawn between terms in the dynamical equations based on phenomenological "few-level" models and microscopic models [89]. In this chapter, I will demonstrate how many-body effects, such as local fields effects, excitation-induced dephasing and frequency shift, and biexciton formation, affect the spectral signatures resulting from four-particle correlations in one-quantum and two-quantum 2D FTOPT measurements by incorporating phe-

nomenological terms into the dynamical equations for a few-level model. This simple treatment of exciton dynamics demonstrates how one-quantum and two-quantum 2D FTOPT spectra can be calculated by solving a set of coupled differential equations based on the optical Bloch equations that are obtained by a spatial Fourier expansion of the electromagnetic fields and the density matrix elements for a two-level system.

4.2 The optical Bloch equations

A simple way to model light-matter interactions is to consider a single optical transition resonant with a classical electromagnetic field, $\vec{F}(\vec{R},t)$. The matter is treated quantum-mechanically such that the optical transition represents a superposition of the ground ($\mid g\rangle$) and excited ($\mid e\rangle$) state wavefunctions of the system that is coupled to the electromagnetic field through the quantum-mechanical dipole moment, μ_{ge}, where $\mu_{ge} = -e_0\langle e \mid \boldsymbol{\mu} \mid g\rangle$. A macroscopic polarization field, $\vec{P}(\vec{R},t)$, is induced in the system upon application of the external field. The system can be represented as a statistical ensemble of two-level systems using a density matrix formalism where

$$\boldsymbol{\rho} = \sum_j P_j \mid j\rangle\langle j \mid$$

is the general density matrix operator. Therefore the induced polarization field is defined as

$$\begin{aligned} \vec{P}(\vec{R},t) &= \varepsilon_0\chi_e(t)\vec{F}(\vec{R},t) \\ &= N\mathrm{Tr}[\boldsymbol{\mu}\boldsymbol{\rho}] \end{aligned} \tag{4.1}$$

where N is the excitation density, $\chi_e(t)$ is the electronic susceptibility of a dielectric material and ε_0 is the permittivity of free space. For sufficiently intense applied fields, the induced polarization field can be expanded in a Taylor series according to

the number of field interactions, such that

$$\begin{aligned}\vec{P}(\vec{R},t) &= \varepsilon_0(\chi^{(1)}(t)\vec{F}(\vec{R},t) + \chi^{(2)}(t)\vec{F}^2(\vec{R},t) + \chi^{(3)}(t)\vec{F}^3(\vec{R},t) + ...) \\ &= N\mathrm{Tr}[\boldsymbol{\mu}\boldsymbol{\rho}^{(1)}] + N\mathrm{Tr}[\boldsymbol{\mu}\boldsymbol{\rho}^{(2)}] + N\mathrm{Tr}[\boldsymbol{\mu}\boldsymbol{\rho}^{(3)}] + ...\end{aligned} \tag{4.2}$$

If the sample is sufficiently thin, the time-dependent signal field driven is related to the induced polarization by a phase shift, in other words $\vec{E}_S \propto i\vec{P}(\vec{R},t)$. Therefore, in general, a calculation of the signal field depends on the determination of the time-dependent evolution of the density matrix operator.

The time-dependent evolution of the density matrix representing a two-level system (defined in Eqn. 4.4)[1] is obtained by integrating the Liouville equation (Eqn. 4.3) that involves the total Hamiltonian, $\boldsymbol{H}$, defined in Eqn. 4.5.

$$\dot{\boldsymbol{\rho}} = -\frac{i}{\hbar}[\boldsymbol{H},\boldsymbol{\rho}] \tag{4.3}$$

$$\boldsymbol{\rho} = \begin{pmatrix} |\, e\rangle\langle e\,| & |\, g\rangle\langle e\,| \\ |\, e\rangle\langle g\,| & |\, g\rangle\langle g\,| \end{pmatrix} = \begin{pmatrix} n_e & p_{ge} \\ p_{eg} & n_g \end{pmatrix} \tag{4.4}$$

$$\begin{aligned}\boldsymbol{H} &= \boldsymbol{H_0} + \boldsymbol{H_I} + \boldsymbol{H_R} \\ &= \begin{pmatrix} \varepsilon_e & 0 \\ 0 & \varepsilon_g \end{pmatrix} - \begin{pmatrix} 0 & \mu_{ge}\vec{F}(\vec{R},t) \\ \mu_{eg}\vec{F}^*(\vec{R},t) & 0 \end{pmatrix} \\ &- \begin{pmatrix} \Gamma_e & \gamma_{ge} \\ \gamma_{eg} & \Gamma_g \end{pmatrix} \times \boldsymbol{\rho}\end{aligned} \tag{4.5}$$

Here, ε_g and ε_e are the energy levels (depicted in Fig. 4-1(a)) of the ground and excited state wavefunctions, respectively, and population relaxation, Γ_e and Γ_g, and decoherence, γ_{ge} and γ_{eg}, rates have been added phenomenologically. A set of coupled differential equations results (see Eqns. 4.6) when the Liouville equation is expanded,

[1] Assuming an ensemble of pure states such that $\mathrm{Tr}[\boldsymbol{\rho}] = 1$.

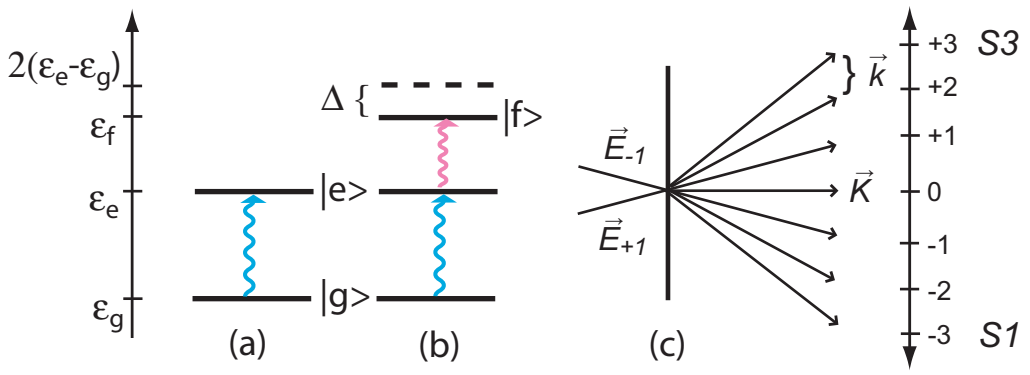

Figure 4-1: Energy level diagram for the (a) two- and (b) three-level systems treated by the optical Bloch equations, which are solved by a (c) spatial Fourier expansion of the incident electromagnetic fields and density matrix elements.

which are also known as the optical Bloch equations (OBE) and treated in several excellent texts [90, 91, 85]. For brevity, only two elements of the density matrix, the excited state population, n_e, and the ground state-excited state coherence, p_{ge}, are detailed here.

$$\dot{n}_e = -\Gamma_e n_e + \Delta_{ge} p_{eg} + \Delta_{eg} p_{ge} \tag{4.6}$$
$$\dot{p}_{ge} = \Omega_{ge} p_{ge} + \Delta_{ge}(n_g - n_e)$$

Note that the following substitutions have been made: $\Omega_{ge} = \frac{i}{\hbar}(\varepsilon_g - \varepsilon_e) - \gamma_{ge} = i\omega_{ge} - \gamma_{ge}$ and $\Delta_{ge} = \frac{i}{\hbar}\mu_{ge}\vec{F}(\vec{R}, t)$. Also, note that $\Delta_{eg} = (\Delta_{ge})^*$.

The response of the system limited to a single interaction with the applied field, i.e. the linear response, can be determined by integrating the OBE, which yields the time evolution of the first-order density matrix operator, $\boldsymbol{\rho}^{(1)}$. The signal field induced by the macroscopic linear polarization field, $\vec{P}^{(1)}(\vec{R}, t)$, is depicted in Fig. 4-2. The real part of the signal field is negative-going and is characterized by an absorptive lineshape, which indicates that the interference between the full signal field and the incident field will result in absorption of light from the incident field.

This semi-classical approach, which results in the equations of motion given by Eqns. 4.6, can be extended to include several field interactions in order to obtain a simple approximation of 2D FTOPT spectra which is successful at explaining the 2D

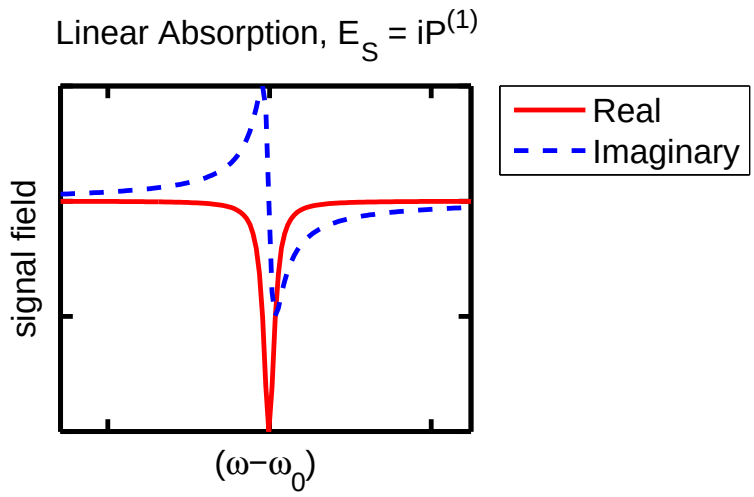

Figure 4-2: Signal field induced by the macroscopic linear polarization field, $\vec{P}^{(1)}(\vec{R},t)$. The real part of the field can be described as "absorptive" while the imaginary part is characterized by a "dispersive" lineshape. The real part is negative-going, indicating that light from the applied field is absorbed by the material. The imaginary part has a positive slope for increasing frequency which indicates positive dispersion of the applied field.

spectral lineshapes measured for an atom such as rubidium vapor shown in Chapter 6. The measured 2D FTOPT signal field, $\vec{E}_S$, is proportional to the macroscopic polarization, $\vec{P}^{(3)}$, induced in the sample by the three excitation fields, $\vec{E}_A$, $\vec{E}_B$ and $\vec{E}_C$.

$$\begin{aligned}\vec{E}_S(\vec{R},t) &\propto i\vec{P}^{(3)}(\vec{R},t) \\ &\equiv i\boldsymbol{\chi}^{(3)}(t)\vec{E}_A(\vec{R},t)\vec{E}_B(\vec{R},t)\vec{E}_C^*(\vec{R},t) \\ &= iN\mathrm{Tr}[\boldsymbol{\mu}\boldsymbol{\rho}^{(3)}(\vec{R},t)]\end{aligned} \tag{4.7}$$

In Eqn. 4.7, $\chi^{(3)}$ is the third-order electronic susceptibility tensor and is related to $\boldsymbol{\rho}^{(3)}$, the time-dependent third-order density matrix of the system. Perturbation theory [91] may be employed at this point to separate and integrate independently terms in Eqn. 4.6 that depend on an increasing number of electromagnetic field interactions with the system in order to isolate $\boldsymbol{\rho}^{(3)}$. However, the wavevector dependence of the signal can also be exploited such that the terms of the density matrix and electromagnetic

field are expanded according to their spatial Fourier components [92], given in Eqns. 4.8 and 4.9, respectively.

$$n_e = \sum_{m=-M}^{M} n_{e,m}\exp[im\vec{k}\vec{R}] \tag{4.8}$$
$$p_{ge} = \sum_{m=-M}^{M} p_{ge,m}\exp[i(\vec{K}+m\vec{k})\vec{R} - i\omega_0 t]$$

$$\vec{F}(\vec{R},t) = A_{-1}(t)\exp[i(\vec{K}-\vec{k})\vec{R}] + A_1(t)\exp[i(\vec{K}+\vec{k})\vec{R}] \tag{4.9}$$

These wavevector components are depicted in Fig. 4-1(c). Note that for the present calculation, the electromagnetic field is written as a sum of two components with wavevectors $\vec{K}+\vec{k}$ and $\vec{K}-\vec{k}$. In other words, two of the excitation fields used in 2D FTOPT experiments, $\vec{E}_A$ and $\vec{E}_B$, have been combined such that they propagate along the same direction, i.e. $\vec{k}_A = \vec{k}_B = \vec{K}+\vec{k}$. Therefore, $\vec{k}_C = \vec{K}-\vec{k}$. In Eqn. 4.9, the pulse envelopes are given by

$$A_m(t) = \exp[-(t-t_m)^2/\sigma^2]\exp[-i\omega_0(t-t_m)] \tag{4.10}$$

where σ is the pulse duration, t_m is the envelope and carrier-wave delay, and ω_0 is the frequency of the carrier wave. Inserting Eqns. 4.8 and 4.9 into 4.6 yields a set of coupled differential equations (Eqn. 4.11) which may be written generally with respect to the wavevector factor, m, of the spatial Fourier expansion.

$$\begin{aligned}
\dot{n}_{e,m} = \{&-\Gamma_e n_{e,m} + \Delta_{ge,-1}p_{eg,(-m-1)} + \Delta_{ge,1}p_{eg,(-m+1)} \\
&+ \Delta_{eg,-1}p_{ge,(m-1)} + \Delta_{eg,1}p_{ge,(m+1)}\} \\
&\times \exp[im\vec{k}\vec{R}] \\
\dot{p}_{ge,m} = \{&\Omega_{ge}p_{ge,m} + \Delta_{ge,-1}(n_{g,(m+1)} - n_{e,(m+1)}) \\
&+ \Delta_{ge,1}(n_{g,(m-1)} - n_{e,(m-1)})\} \\
&\times \exp[i(\vec{K}+m\vec{k})\vec{R} - i\omega_0 t]
\end{aligned} \tag{4.11}$$

Although this approach does not yield a result different from a perturbative treatment of the dynamical equations for the simple two-level model presented here, it was shown that this method was necessary to replicate the variation of the four-wave mixing signal contributions [86, 93] with respect to excitation density when many-body effects were included. This approach will also be required to correctly predict the lineshapes of the one-quantum and two-quantum 2D FTOPT spectral features.

The signal of interest propagates in the direction defined by $\vec{k}_S = \vec{k}_A + \vec{k}_B - \vec{k}_C$. Therefore, if we impose the time constraint that the field with wavevector $\vec{K} + \vec{k}$ precedes the field with wavevector $\vec{K} - \vec{k}$ (i.e. $t_1 < t_{-1}$), the one-quantum rephasing 2D FTOPT signal will propagate along the direction defined by $m = -3$. The two-quantum 2D FTOPT signal can be obtained by reversing the time-ordering of the fields. Or, equivalently, the two-quantum signal can be isolated by taking the signal component that propagates along the wavevector direction defined by $m = 3$. Therefore, Eqn. 4.7 becomes Eqn. 4.12 and Eqn. 4.13 for the rephasing (S1) and two-quantum (S3) signals, respectively.

$$\vec{E}_{S1}(t) \propto iN(\mu_{eg} p_{ge,-3} + c.c.) \tag{4.12}$$

$$\vec{E}_{S2}(t) \propto iN(\mu_{eg} p_{ge,3} + c.c.) \tag{4.13}$$

The excited-ground state coherence terms in Eqns. 4.12 and 4.13 are calculated by integrating the set of coupled differential equations defined by Eqn. 4.11 for $m = \{-3, -2, ...3\}$ using a fourth-order Runge-Kutta method[2] for numerical integration [94]. This calculation is repeated for increasing interpulse delay, τ, where, $\tau \equiv t_1 - t_{-1}$. Subsequent 2D Fourier transformation of $S(\tau, t)$ yields the 2D FTOPT spectrum, $S(\omega_\tau, \omega)$. The calculated rephasing 2D FTOPT spectrum for a simple two-level system is shown in Fig. 4-3. The magnitude spectrum in Fig. 4-3 shows a single feature on the $y = -x$ diagonal line, indicating that the system evolved with

[2]To ensure fidelity of results, the integration step size, h, should be no larger than one-tenth of the optical cycle defined by the exciton polarization frequency, i.e. $h \leq 1/10\omega_{ge}$

the same frequency, ω_{ge}, during τ and t, but with opposite phase. The lineshape is rounded overall because no inhomogeneous broadening was included in this model. If inhomogeneous broadening were included, the 2D lineshape would be elongated along the diagonal such that the width of the peak along the diagonal would give the inhomogeneous linewidth, while the width of the peak taken from a slice perpendicular to the diagonal would give the homogeneous linewidth. The real part of the 2D lineshape shown in Fig. 4-3 is positive-going and has an absorptive lineshape, primarily, which indicates that energy was added to the final field (i.e. stimulated emission) by the sample during the emission time, t. The imaginary part of the 2D lineshape, in Fig. 4-3, is mainly dispersive and has normal, positive dispersion. The calculated two-quantum 2D FTOPT spectrum (not shown) is zero for all frequencies in this case of a two-level system that represents non-interacting excitations.

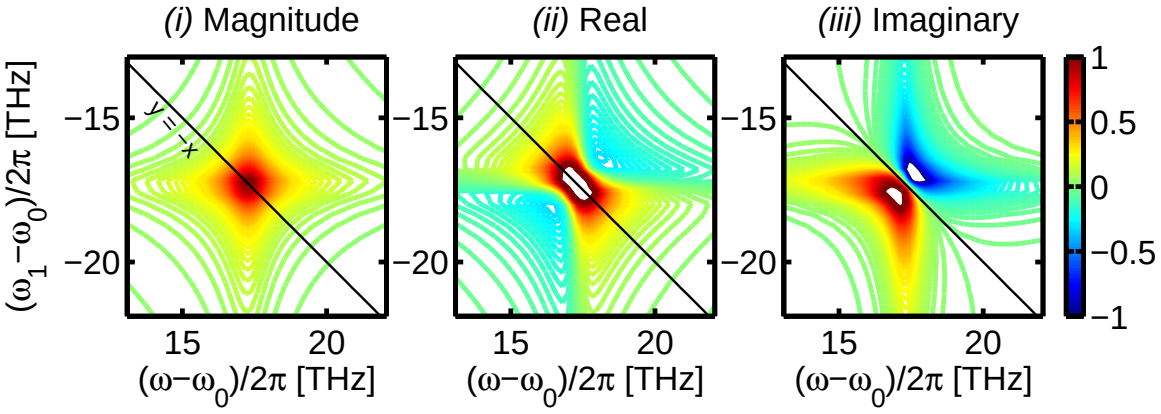

Figure 4-3: Magnitude (i), real (ii) and imaginary (iii) parts of the rephasing 2D FTOPT spectrum calculated for an independent two-level system with the following parameters: $\omega_{ge}/2\pi = 372.3$ THz, $\gamma_{ge}/2\pi = 0.5$ THz, $\omega_0/2\pi = 355.0$ THz and $\sigma = 0.065$ ps.

4.2.1 A cascaded three-level system

The equations of motion of the density matrix elements for a two-level system (Eqns. 4.6) can be extended for the cascaded three-level system depicted in Fig. 4-1(b). Three additional relations are required to describe light-matter interactions for a

three-level system which give the time-dependence of the doubly excited state population, n_f, and the coherent superposition of the doubly excited state with the singly excited state and ground state, p_{ef} and p_{gf}, respectively. The full set of coupled differential equations is then elaborated using the spatial Fourier expansion in order to isolate the third-order density matrix operator. The rephasing and two-quantum 2D FTOPT spectra produced by the optical Bloch equations for a cascaded three-level model are shown in Fig. 4-4 and Fig. 4-5, respectively. In both cases, a new spectral feature which is red-shifted along the emission axis from the main resonance at 372.3 THz appears, which is largely negative going and indicates absorption of the final field.

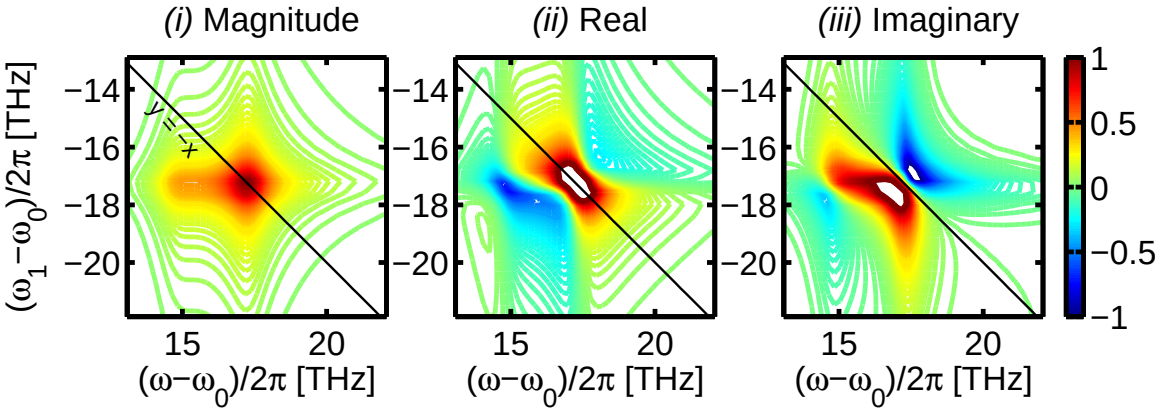

Figure 4-4: Magnitude (i), real (ii) and imaginary (iii) parts of the rephasing 2D FTOPT spectrum calculated for a cascaded three-level system with the following parameters: $\omega_{ge}/2\pi = 372.3$ THz, $\gamma_{ge}/2\pi = 0.5$ THz, $\omega_{ef}/2\pi = 371.5$ THz, $\gamma_{ef}/2\pi = 0.6$ THz, $\gamma_{gf}/2\pi = 1.0$ THz, $\omega_0/2\pi = 355.0$ THz and $\sigma = 0.065$ ps.

4.3 The modified optical Bloch equations

As described in Section 4.1, higher-order correlations of excitons can be treated using the equations of motion derived from a multi-electron Hamiltonian that incorporates the energies and dipole couplings of electron and hole wavefunctions, which can be written as Bloch functions in wavevector, or k, space. In this case, the density matrix would represent an ensemble of carrier states of equal k for all values of k allowed for

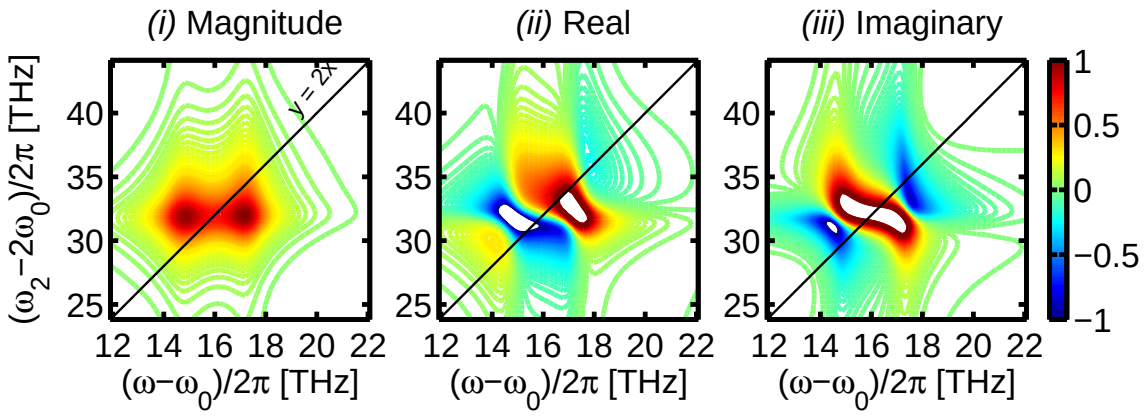

Figure 4-5: Magnitude (i), real (ii) and imaginary (iii) parts of the two-quantum 2D FTOPT spectrum calculated for a cascaded three-level system with the following parameters: $\omega_{ge}/2\pi = 372.3$ THz, $\gamma_{ge}/2\pi = 0.5$ THz, $\omega_{ef}/2\pi = 371.5$ THz, $\gamma_{ef}/2\pi = 0.6$ THz, $\gamma_{gf}/2\pi = 1.0$ THz, $\omega_0/2\pi = 355.0$ THz and $\sigma = 0.065$ ps.

the specific conduction and valence bands of the material. Correlations are introduced into the Hamiltonian through Coulomb interactions between density matrix elements with different wavevector.

The equations of motions derived for the wavevector-space density matrix for a multi-electron Hamiltonian are known as the semiconductor Bloch equations [85] and can be simplified using several approximations. A basic approximation is to assume that the energies, dephasing rates and field interactions of the electrons and holes are renormalized such that the carriers do not react to the external electromagnetic field alone, but to an internal dipole field generated by all nearby electron-hole excitations as well. This approximation is equivalent to a mean-field, or Hartree-Fock, approach and can be incorporated into the optical Bloch equations (Eqn. 4.6) by introducing a Lorentz local field. See Section 4.3.1 for further discussion.

Coulomb interactions introduced by a multi-electron Hamiltonian give rise to driving terms in the dynamical equations of the density matrix elements that depend on products between populations and coherences of different wavevectors, which can be realized through a dynamics-controlled truncation of the semiconductor Bloch equations. These four-particle correlations can be approximated by replacing correlations between populations and coherences of different k with correlations between density

matrix elements of equal k. This simplifies the problem to a two-level model, similar to the OBE, where exciton correlations, described phenomenologically as excitation-induced dephasing (EID) and excitation-induced frequency shift (EIS), can be incorporated into the dynamical equations for a two-level model by including terms that modify the exciton dephasing rate, γ_{ge}, and exciton coherence frequency, ω_{ge}, proportional to the excitation density, N. The resulting equations (see Eqns. 4.14) are known as the modified optical Bloch equations (MOBE).

$$\begin{aligned} \dot{n}_e &= -\Gamma_e n_e + (\Delta_{ge} + \Delta_{ge}^L) p_{eg} + (\Delta_{eg} + \Delta_{eg}^L) p_{ge} \\ \dot{p}_{ge} &= i(\omega_{ge} + n_e N\omega') p_{ge} - (\gamma_{ge} + n_e N\gamma') p_{ge} \\ &\quad + (\Delta_{ge} + \Delta_{ge}^L)(n_g - n_e) \end{aligned} \tag{4.14}$$

The MOBE can be expanded to include field interactions to third order by spatial Fourier expansion, similar to the method described above for the optical Bloch equations. Therefore, exciton interaction contributions to the signal are introduced through the phenomenological excitation-induced dephasing, γ', and frequency shift, ω', parameters. Mean-field contributions to the signal are introduced through Δ_{ge}^L which is proportional to the Lorentz local field, $\vec{F}^L(\vec{R}, t)$, i.e.

$$\Delta_{ge}^L = \frac{i}{\hbar} \mu_{ge} \vec{F}^L(\vec{R}, t) \tag{4.15}$$

Here I will present the one-quantum rephasing and two-quantum 2D FTOPT spectra obtained when incorporating many-body effects using the modified optical Bloch equations. The resulting 2D FTOPT spectra presented here differ from those calculated by the two-level optical Bloch equations in two ways. The complex parts of the rephasing 2D spectral features exhibit a phase shift or a phase "twist," depending on the type and strength of the many-body effect included in the model. Also, new spectral features appear in the two-quantum 2D FTOPT spectra at a frequency of $2\omega_{ge}$ along the ω_τ axis. These new spectral features are analogous to contributions to the two-pulse four-wave mixing signal at "negative delay" (see Section 5.1 for further

discussion) observed in measurements on semiconductor QWs without the possibility of resolving their origins. The new spectral features and modified 2D lineshapes will be present in the one-quantum and two-quantum measurements on GaAs QWs in Chapter 5 due to signal contributions that arise from Coulomb interactions between excited carriers and mean-field effects. In contrast, one-quantum and two-quantum measurements on dense Rb vapor (see Chapter 6) will only exhibit signal contributions that arise from mean-field effects.

4.3.1 Local field effects

The linear and nonlinear optical responses of a dense system of oscillators, i.e. $N > 10^{22}/\mathrm{m}^3$, are driven not only by the macroscopic, or "Maxwell", electromagnetic field, but also by a local, or "Lorentz", field which originates from interferences with the polarization field emitted by a nearby oscillator. Essentially, the definition stated in Eqn. 4.1 is no longer true, i.e. the proportionality of the polarization field, $\vec{P}$, to the excitation fields through the electronic susceptibility, χ_e, breaks down. In other words, the electronic susceptibility is modified in order to incorporate the effect of local fields [95]. See Section 6.1 for further discussion. Therefore, local field effects can drive new time-dependent coherent contributions to the one-quantum and two-quantum 2D FTOPT signals.

Local field effects can be incorporated into the two-level model presented in Section 4.2 by separating the general electromagnetic field introduced in Eqn. 4.5 into two pieces, such that $\vec{F}(\vec{R},t) = \vec{F}_M(\vec{R},t) + \vec{F}_L(\vec{R},t)$, where the first term on the right is equivalent to the total field defined in Eqn. 4.9 and the second term is the Lorentz local field and has a dependence on the number density of excitations, N, such that

$$\begin{aligned} \vec{F}_L(\vec{R},t) &= l\vec{P}^{(1)}(\vec{R},t) \\ &\equiv lN\mathrm{Tr}[\boldsymbol{\mu}\boldsymbol{\rho}^{(1)}(\vec{R},t)] \end{aligned} \tag{4.16}$$

where l is the Lorentz local field factor.[3] The elements of the time-dependent first-

[3]The Lorentz local field is calculated by delineating a sphere within a uniformly polarized medium

order density matrix, $\boldsymbol{\rho}^{(1)}(\vec{R},t)$, which represents the wavefunctions of the system after one interaction with the field $\vec{F}_M(\vec{R},t)$, can be calculated by simply integrating numerically the Liouville equation stated in Eqn. 4.3 for different wavevector components of the macroscopic field. Therefore, the Δ_{ge} and Δ_{ge}^L terms in the MOBE (Eqns. 4.11) may also be expanded in terms of their spatial Fourier components, as stated below in Eqn. 4.17.

$$\begin{aligned}\Delta_{ge}+\Delta_{ge}^L = &\frac{i}{\hbar}\mu_{ge}[A_{-1}(t)+lN\mu_{eg}p_{ge,-1}(t)]\times\exp[i(\vec{K}-\vec{k})\vec{R}] \\ &+\frac{i}{\hbar}\mu_{ge}[A_1(t)+lN\mu_{eg}p_{ge,1}(t)]\times\exp[i(\vec{K}+\vec{k})\vec{R}]\end{aligned} \tag{4.17}$$

The calculated rephasing 2D FTOPT spectra including local field effects for different values of the excitation density N are shown in Fig. 4-6. At low N, the real part of the complex 2D lineshape resembles the largely absorptive lineshape characteristic of resonant atom-light interactions explained by the optical Bloch equations. The linewidth of the peak along ω_1 and ω decreases for increasing N. This is possible because the radiative excitations are being driven by the first-order polarization fields of nearby excitations which persist long after the applied field has left the sample. At very high N the entire peak shifts to a higher (i.e. more negative) value along the ω_1 coordinate so that it is no longer centered on the diagonal. This phenomenon can be described in terms of the Lorentz-Lorenz frequency shift which was predicted long ago [96] and has been observed previously in frequency domain [97] and time domain [98] measurements.

The calculated two-quantum 2D FTOPT spectra including local field effects for different values of N are shown in Fig. 4-7. Most prominent is the presence of a signal at $2\omega_{ge}$ which is not predicted by the optical Bloch equations for a two-level system. The width of the real part of the complex 2D lineshape along the ω_2 axis decreases as N increases. This is likely due to the fact that the locally generated fields effectively add a "tail" to the pulsed excitation fields which drive the resonant

containing only one excitation at its center and determining the value of the electric field at the center of the sphere. The Lorentz local field factor reflects the volume of the sphere, therefore, $l=\frac{4\pi}{3}$.

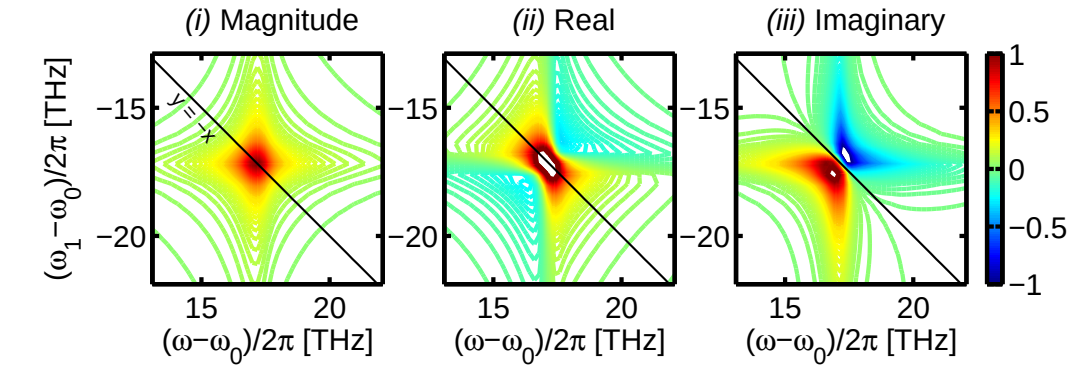

(a) $N{=}10^{22}/\mathrm{m}^3$

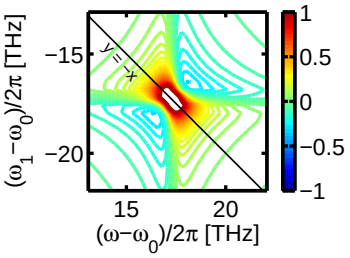

(b) $N{=}10^{19}/\mathrm{m}^3$

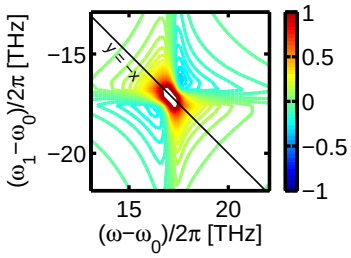

(c) $N{=}10^{24}/\mathrm{m}^3$

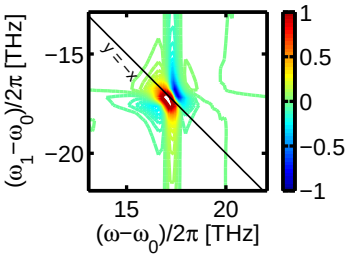

(d) $N{=}10^{25}/\mathrm{m}^3$

Figure 4-6: Calculated rephasing 2D FTOPT spectrum for a two-level system with LFE. Part (a) gives the magnitude, real and imaginary 2D spectra for a moderate excitation density. Parts (b) through (d) show the dependence of the real 2D lineshapes on excitation density.

excitations [98]. At low N the tail is weak, and therefore the width of the two-quantum 2D FTOPT spectral feature approximates the pulse bandwidth. In the present simulations the pulse bandwidth (at FWHM) was 11.6 THz. As N increases, the pulse tail becomes stronger, and therefore, the linewidth shrinks. The presence of a pulse tail also explains the asymmetrical lineshape of the peak along the ω_2 axis. Also, at high N, the lineshape is largely dispersive, similar to contributions driven by excitation-induced shift. See Section 4.3.2.

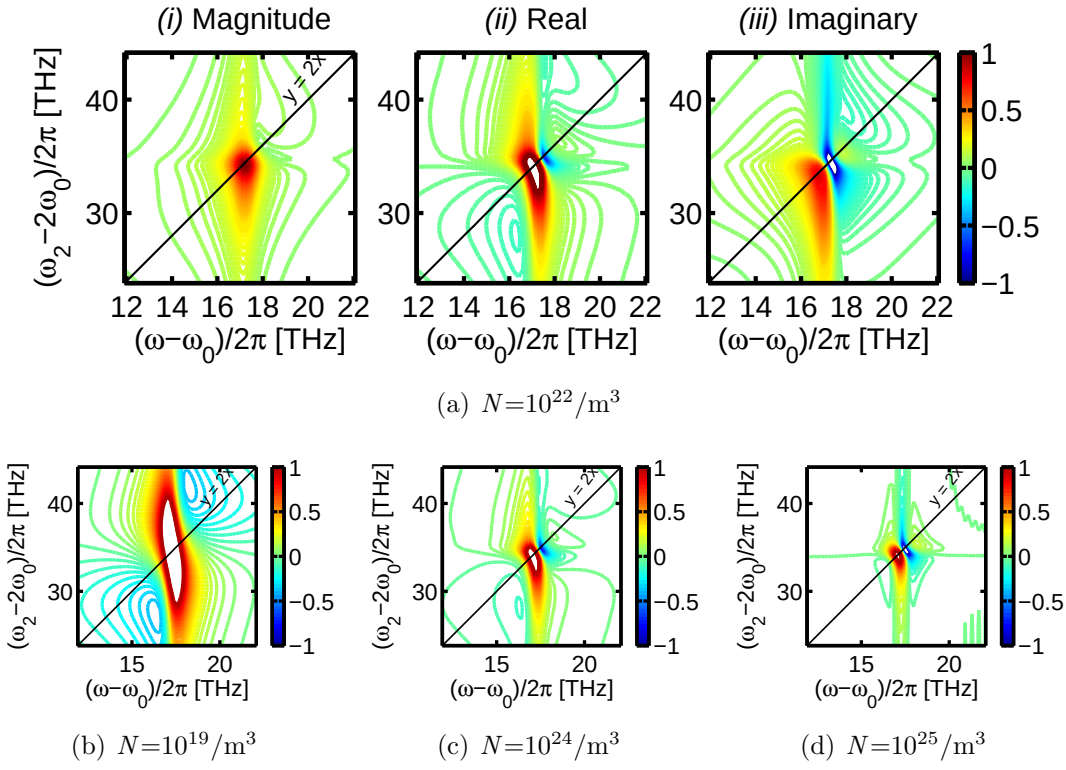

(a) N=10^{22}/m^3

(b) N=10^{19}/m^3 (c) N=10^{24}/m^3 (d) N=10^{25}/m^3

Figure 4-7: Calculated two-quantum 2D FTOPT spectrum for a two-level system with LFE. Part(a) gives the magnitude, real and imaginary 2D spectra for a moderate excitation density. The excitation density was varied and the resulting real 2D lineshapes are shown in part (b) through (d).

4.3.2 Excitation-induced dephasing and frequency shift

Introduction of the phenomenological excitation-induced dephasing and shift parameters, γ' and ω', respectively, into the optical Bloch equations creates new terms in the spatial Fourier expansion of the dynamical equations which depend on products of

the population and coherence terms of the density matrix which satisfy the relations described by Eqn. 4.18, where $\Omega' = N(i\omega' - \gamma')$.

$$\dot{p}_{ge,m}^{MOBE} = \begin{cases} \Omega' \sum_{v=-M}^{M+m} n_{e,(m-v)} p_{ge,v} & \text{for } m \leq 0 \\ \Omega' \sum_{v=-M+m}^{M} n_{e,(m-v)} p_{ge,v} & \text{for } m > 0 \end{cases} \tag{4.18}$$

The complex 2D FTOPT rephasing and two-quantum spectra calculated using the MOBR with excitation-induced dephasing are shown in Fig. 4-8. The real part of the rephasing 2D spectrum continues to have an absorptive lineshape, similar to that predicted by the optical Bloch equations, but rather than being symmetric about the diagonal, it shows a slight twist. The two-quantum spectra also show a feature at $2\omega_{ge}$, similar to the contributions from local field effects. The 2D lineshape for the real two-quantum spectrum is also asymmetric about the diagonal.

Contributions to the rephasing and two-quantum 2D spectra from excitation-induced frequency shift are shown in Fig. 4-9. The two-quantum spectra also show a feature at $2\omega_{ge}$. As opposed to contributions from excitation-induced dephasing, the real part of the rephasing and two-quantum 2D lineshapes are dispersive rather than absorptive. Actually, the lineshapes caused by EIS contributions are similar to changes in the 2D lineshapes caused by LFE, which is reasonable considering that both of these mechanisms contribute a phase shift to the dynamical equations for a two-level model.

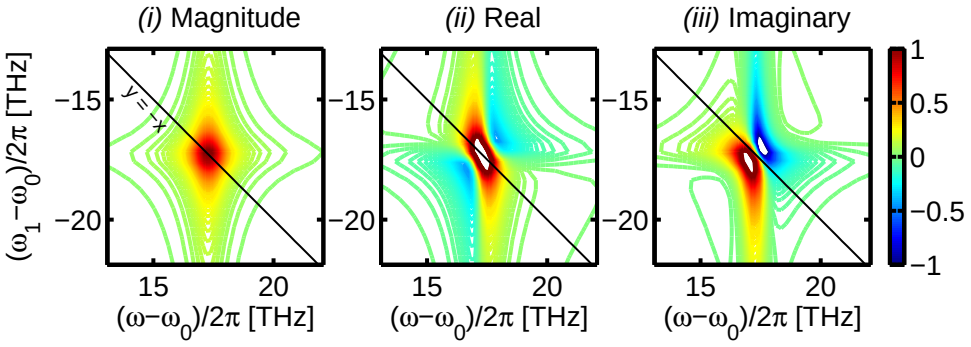

(a) Rephasing 2D FTOPT spectra with EID

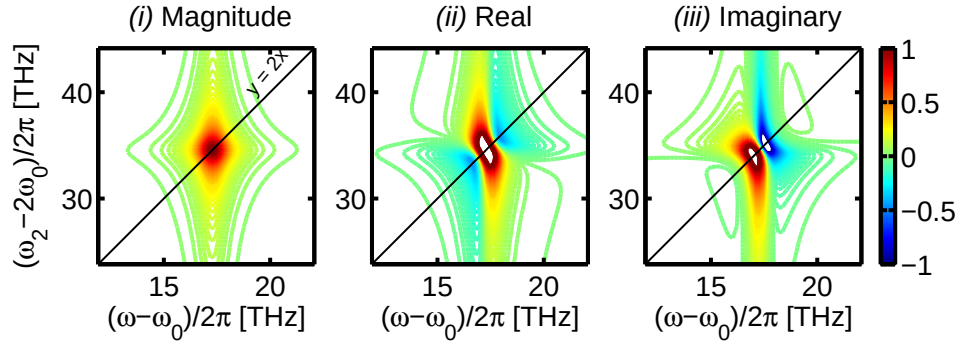

(b) Two-quantum 2D FTOPT spectra with EID

Figure 4-8: Calculated 2D FTOPT spectrum for a two-level system with excitation-induced dephasing. Part(a) shows the one-quantum spectra and part (b) shows the two-quantum spectra. The excitation density, N, is $10^{22}/\mathrm{m}^3$ and the EID parameter, γ', is 25 $\mathrm{THz}/\mathrm{m}^3$.

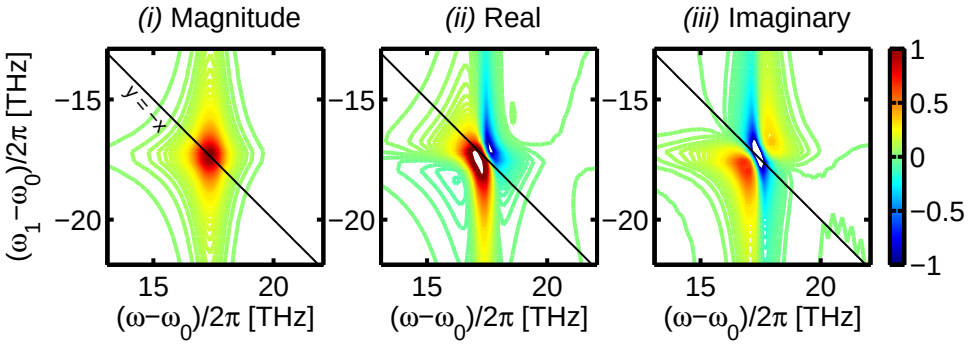

(a) Rephasing 2D FTOPT spectra with EIS

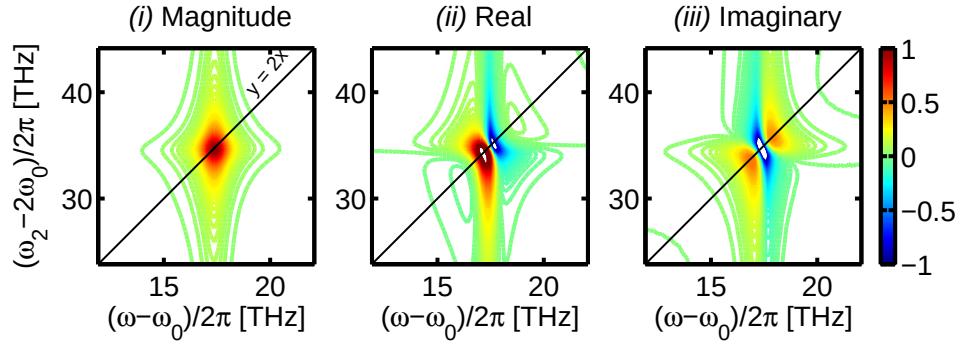

(b) Two-quantum 2D FTOPT spectra with EIS

Figure 4-9: Calculated 2D FTOPT spectrum for a two-level system with excitation-induced shift. Part(a) shows the one-quantum spectra and part (b) shows the two-quantum spectra. The excitation density, N, is $10^{22}/\mathrm{m}^3$ and the EIS parameter, ω', is 25 $\mathrm{THz}/\mathrm{m}^3$.

4.4 Conclusions

While numerical calculations based on microscopic models of exciton interactions are necessary in order to provide a first-principles explanation of the origins and lineshapes of 2D FTOPT spectra, phenomenological models, such as the modified optical Bloch equations presented here, can approximate their general features and provide valuable physical interpretations which are sometimes becomes lost in microscopic models. While a perturbative solution to the modified optical Bloch equations would predict the frequency positions of new features in two-quantum spectra, the solution by spatial Fourier expansion is necessary in order to model the dependence of the spectral features on the excitation density. The results presented here will help interpret the spectral features obtained in one-quantum and two-quantum 2D FTOPT measurements on semiconductor QWs (see Chapter 5) and rubidium vapor (see Chapter 6). One-quantum and two-quantum 2D FTOPT measurements on semiconductor QWs will exhibit characteristics resembling excitation-induced shift and local fields contributions at high N with respect to features at twice the exciton resonance frequency, but characteristics resembling excitation-induced dephasing contributions for spectral features originating from exciton-free carrier interactions. Two-quantum 2D FTOPT measurements on dense Rb vapor will show new spectral features resembling local field contributions at low N.

Chapter 5

Coupled and interacting excitons in semiconductors

5.1 Introduction

The coupling and interactions of correlated electron-hole pairs, or excitons, play a significant role in the optical responses of several types of novel nanostructured materials as discussed in Chapter 1. Exciton interactions, or many-body effects, are especially important in semiconductors because they have a high dielectric constant and a large exciton Bohr radius. Furthermore, exciton interactions, mediated by the far-reaching Coulomb force, strongly influence the electronic and optical properties of confined systems such as semiconductor quantum wells and quantum dots at at excited-state densities ($\sim 10^{10}$ excitations/cm^2 in quantum wells or > 1 excitation in single quantum dots) that are reached routinely in applications and experimental studies. Semiconductors are ideally suited for the study of exciton interactions due to the fact that correlated electron-hole pairs can be generated optically at precisely specified times and densities. As illustrated in Fig. 5-1(a), the electronic energy levels of atoms at different lattice sites combine to form collective electronic band states of the material. Absorption of a photon excites an electron to the conduction band, leaving a positively charged hole in the valence band, as illustrated in Fig. 5-1(b). The Coulomb interactions between these charged carriers result in profound changes

to the linear absorption spectrum of a semiconductor which can be explained in the context of two-particle correlations. For instance, absorption above the bandgap (i.e. Sommerfeld enhancement [85]) is increased and indicates excitation of uncorrelated (free) electron-hole pairs. Below the bandgap, strong narrow absorption lines are observed and indicate the formation of correlated (bound) electron-hole pairs, i.e. excitons. See Fig. 5-1(c). The energetic separation of the exciton absorption lines from the free electron-hole pair absorption is proportional to the exciton binding energy.

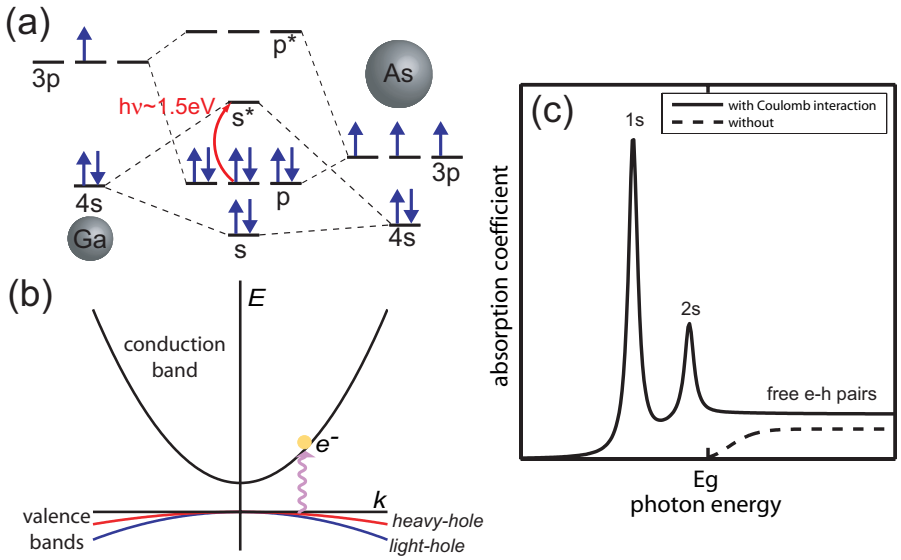

Figure 5-1: (a) Energy level diagram in the electron and hole representation showing the origin of different exciton states in bulk GaAs based on the underlying atomic orbital and spin states. (b) Typical band diagram for a bulk semiconductor. The valence bands are formed from p-like states (see Fig. 5-2(b)) and at the band edge (i.e. k=0) the heavy-hole (red line) and light-hole (blue line) valence bands are degenerate. The conduction band (black line) is formed from s-like states and is energetically separated from the valence bands such that, at room temperature, k_BT is much less than the bandgap. (c) Illustration of the linear absorption spectrum of a bulk semiconductor with (solid line) and without (dashed line) Coulomb interactions. Free electron-hole pairs absorb photons with energy higher than the bandgap, E_g. Coulomb interactions increase the absorption coefficient of the free electron-hole pairs and create excitons, which absorb below E_g and have hydrogen-like wavefunctions.

The linear absorption spectrum of a semiconductor quantum well differs from the bulk absorption spectrum because the exciton is confined by an energy potential whose size (in one dimension) is smaller than the exciton Bohr radius for that particular

material. For instance, the exciton binding energy for a quantum well is larger than for a bulk semiconductor. As the exciton wavefunction is confined by the one-dimensional potential formed by the energetic difference between the bandgaps of the alternately-layered semiconductor materials with similar lattice constants (see Fig. 5-2(a)) it assumes more s-orbital character in order to conserve a more energetically favorable spherical symmetry. For instance, in bulk GaAs the exciton binding energy is 4.9 meV [99] compared to 10 meV for GaAs/$Al_{0.3}Ga_{0.7}As$ quantum wells [100].

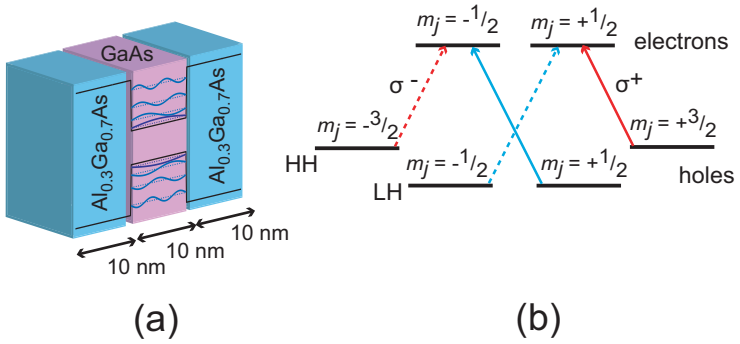

Figure 5-2: (a) Schematic of a GaAs/$Al_{0.3}Ga_{0.7}As$ multiple quantum well. The "well" material is GaAs, which as a bandgap of 1.424 eV, and is 10 nm thick. The "barrier" material is $Al_{0.3}Ga_{0.7}As$, which has a bandgap of 1.798 eV, and is also 10 nm thick. The barrier is thick enough to prevent tunneling such that the excitons in adjacent wells are uncoupled. The exciton Bohr radius in GaAs is 11.2 nm [99]. An illustration of the confined electron (in the upper potential energy well) and hole (in the lower potential) wavefunctions is included. (b) Expanded view of p and s^* states in Fig. 5-1(a) from which excitons are formed. The excited electron is in an s-type state with orbital, spin, and total quantum numbers $L = 0$, $S = \frac{1}{2}$, $J = L + S = \frac{1}{2}$, with degenerate spin sublevels $m_j = \pm\frac{1}{2}$. The hole is in a p-type state with $L = 1$, $S = \frac{1}{2}$, $J = \frac{3}{2}$ or $J = \frac{1}{2}$. The $J = \frac{1}{2}$ level (not shown) has higher energy and compose the split-off valence band. The $J = \frac{3}{2}$ level has spin sublevels $m_j = \pm\frac{3}{2}$ and $\pm\frac{1}{2}$ whose energies are split due to quantum confinement, labeled heavy-hole (HH) and light-hole (LH) due to their effective masses in GaAs of $0.51m_e$ and $0.082m_e$, respectively (the electronic state has effective mass $0.063m_e$). Red (blue) arrows represent excitation of the HX (LX) exciton. Solid (dashed) arrows represent right-hand (left-hand) circularly polarized light.

Also, the exciton linewidth for a quantum well is smaller than for a bulk semiconductor. The exciton dephasing, mainly due to scattering with acoustic [101] and optical [102] phonons, is sensitive to quantum confinement because an increasing

number of electron and hole subbands, from which the exciton is formed, become energetically accessible for a given temperature as the well width increases. Quantum confinement also splits the degenerate spin-orbit states of the valence band, called heavy-hole (HH) and light-hole (LH), because their effective masses differ. Valence band splitting occurs because the bulk electron and hole wavefunctions, which are Bloch functions that are defined in reciprocal space with respect to wavevector k, must now satisfy a new minimum boundary condition, specifically $k = \pi/d$, where d is the well width, instead of $k = 0$. Therefore, exciton absorption lines formed from the HH and LH bands, named heavy-hole (HX) and light-hole (LX) excitons, respectively, will appear in the linear absorption spectrum of a quantum well. Since the HH and LH bands have different angular momentum projections, the optical selection rules for the two excitons differ with respect to circular polarization of the light [99]. Polarization selection rules for photon absorption for hole and electron states at the valence and conduction band edges of a semiconductor quantum well are shown in Fig. 5-2(b).

The significance of exciton coupling and interactions to the coherent nonlinear responses of semiconductor quantum wells was realized from two-pulse four-wave mixing (FWM) experiments using pulsed laser sources which can deliver short bursts of coherent photons to such materials [8]. Here, the sample is irradiated by two ultrafast pulses $\vec{E}_1$ and $\vec{E}_2$ that propagate in two separate beams with wavevectors $\vec{k}_1$ and $\vec{k}_2$.[1] At positive delay times, field $\vec{E}_1$ arrives first and generates an exciton coherence. After a time delay τ the $\vec{E}_2$ field arrives and interacts twice with the sample. The first $\vec{E}_2$ field interaction generates a population grating pattern with wavevector $\vec{k}_2 - \vec{k}_1$, and the second $\vec{k}_2$ field interaction yields coherent scattering, or "self-diffraction," from this grating pattern to produce the signal field at the phase-matched wavevector direction $\vec{k}_S = 2\vec{k}_2 - \vec{k}_1$. The signal can be measured with a slow detector (time-integrated) or gated by another ultrafast laser pulse such that its time-dependent intensity after the final field interaction is resolved. Oscillations

[1]The $\vec{k}_1$ beam plays a role analogous to the $\vec{k}_C$ beam of 2D FTOPT measurements while the $\vec{k}_2$ beam plays the role of the combined $\vec{k}_A$ and $\vec{k}_B$ beams, with the same wavevector direction as $\vec{k}_A + \vec{k}_B$ and with its field interacting twice with the sample.

observed in time-integrated two-pulse FWM measurements at positive delay with a frequency proportional to the energy splitting between the HH and LH valence bands were evidence for coupling of HX and LX excitons through the conduction band [103]. However, time-resolved measurements of the signal field [104] were necessary to distinguish the origin of the oscillations as quantum beating, which is characteristic of a coupled system, as opposed to polarization interferences resulting from two uncoupled excitons.

The range of the Coulomb force mediating two-particle correlations is long so the behavior of excitons may be influenced by higher-order correlations that arise through interactions with other multiple-particle complexes such as excitons or unbound electron-hole pairs. Thus, spectroscopically measured optical responses can be described by the coherent motions of a hierarchy of multiple-particle correlations. At the level of four-particle correlations, a pair of excitons may form bound quasiparticle, known as a biexciton. The energy of the biexciton state, ε_b, differs from the sum of energies of the exciton states by the biexciton binding energy, Δ. In another instance of four-particle correlations, an exciton may scatter from another bound or unbound electron-hole pair. From early optical FWM experiments [105, 17] on semiconductor quantum wells it was evident that the oscillation frequency of exciton coherences, ω_e, (which is related to the exciton energy $\varepsilon_e = \hbar/\omega_e$) and dephasing rate, γ_e, of exciton coherences were dependent on the excited carrier density, the effects dubbed excitation-induced shift (EIS) and excitation-induced dephasing (EID), respectively.

Higher-order particle correlations were soon observed [106] and recognized [107] as one of the contributions to signal at "negative delay" in the two-pulse FWM experiments described above. For such measurements on a system composed of non-interacting excitations (with a single excited state), no signal should be possible if field $\vec{E}_2$ arrives at the sample before $\vec{E}_1$ (typically denoted as $\tau < 0$) because a population grating at wavevector $\vec{k}_2 - \vec{k}_1$ does not diffract one of the fields into the signal direction. In similar one-dimensional measurements with a single time delay period between the two incident pulses, several many-body correlations, described phenomenologically as excitation-induced dephasing [18], excitation-induced energy

shift [86] and biexciton formation [20], were shown to give rise to signal contributions at negative delay, but these contributions were heavily convolved because they all had dephasing times on the order of 1–2 ps. Furthermore, these higher-order correlations may also be convolved with contributions that can be described as "mean-field" effects [21, 108, 22], such as the Lorentz local field effects that also occur for a dense atomic vapor as described in Chapter 6. In addition, demanding first-principles calculations that include the full complement of particle interactions and correlations were also performed to understand the role of exciton interactions in these observations [83, 109, 110, 111]. All of these many-body phenomena are the subject of several reviews [112, 113, 114, 115].

The clearest experimental signature of exciton interactions would be direct observation of the coherences and dynamics of biexcitons – four-particle (or two-quasiparticle) correlations – and higher-order correlated motions. Biexciton states are more conveniently displayed in a quasiparticle picture, as in Fig. 5-3, where three tiers of states represent the sample with increasing levels of collective excitation: the ground state (no excitation), the exciton, X, states (one-quantum excitations) and the biexciton, X_2, states (two-quantum excitations). Biexciton-ground state coherences generally do not radiate since the corresponding two-quantum transitions are formally forbidden. Rather they are probed indirectly through sequential single-quantum transitions. Therefore frequency domain experiments such as photoluminescence [19] and spectrally resolved FWM measurements [116] on these materials may reveal biexciton energetics and some dephasing information if the biexciton binding energy is larger than the low-temperature exciton linewidth ($\sim$ 1 meV). Otherwise, as in GaAs/AlGaAs QWs, biexciton contributions to the signal appear as no more than a shoulder on the much stronger ground state-exciton absorption band.

High-order *nuclear spin* coherences have been isolated and observed through multiple-quantum techniques [117] used in two-dimensional Fourier transform nuclear magnetic resonance (2D FTNMR) spectroscopy. The dipolar interaction strength between neighboring spins excited by two RF fields differs when the precessing moments are aligned parallel or perpendicular to the direction between the two nuclei. The

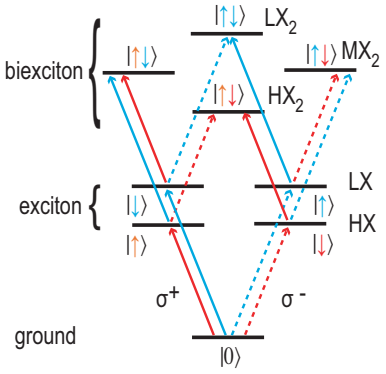

Figure 5-3: Energy level diagram in the quasiparticle (i.e. exciton) representation illustrating the polarization selection rules for excitons (HX and LX) and biexcitons (HX_2, MX_2 and LX_2.) Red (blue) arrows represent excitation by a photon with energy proportional to the HX(LX) exciton transition frequency. Solid (dashed) arrows represent right-hand (left-hand) circularly polarized light. Since the HX and LX excitons are composed of an electrons and holes of opposite spin, see Fig. 5-2(b), the cross-circular polarization of fields $\vec{E}_A$ and $\vec{E}_B$ in our 2D FTOPT experiments will excite pure HX_2 and LX_2 biexciton coherences whereas co-circular polarization will excite mixed (MX_2) biexciton coherences.

maxima and minima in the interaction strength occur twice each precession cycle such that if the one-quantum precession frequency is ω_s then the interaction has a component that oscillates at $2\omega_s$. The resulting *two-quantum* coherence at the same frequency does not have a net magnetic moment and cannot be measured directly. Therefore the measurement must include a third field, phase-coherent with the first two fields, which produces a new one-quantum spin coherence that is also phase-coherent with the two-quantum coherence. The resulting free induction decay is measured while the arrival time τ_2 of the third field is incremented. The amplitude and phase of the signal emitted during time t after the third field depend on the phase relationships among the RF fields and the one- and two-quantum coherences they generated. A 2D-FT of the complex signal, $S(\tau_2, t)$, yields a 2D spectrum, $S(\omega_2, \omega)$, where groups of one-quantum spin coherences (appearing along the emission frequency coordinate, ω) sharing the same two-quantum coherence frequency along ω_2 are revealed to originate from equivalent pairs of coupled nuclei, and in this way the skeleton of even a large protein can be constructed. This scenario suggests

how higher-order electronic correlations, such as biexciton coherences, could be observed through an optical analog to two-quantum 2D FTNMR, i.e. two-quantum 2D FTOPT spectroscopy.

In this chapter, I will present one-quantum and two-quantum 2D FTOPT measurements on a $GaAs/Al_{0.3}Ga_{0.7}As$ quantum wells that reveal distinct signatures of exciton coupling and interactions. The one-quantum 2D FTOPT spectra reveal spectral signatures which indicate exciton coupling, but that are typically convolved in the conventional two-pulse FWM measurements described above. The complex one-quantum 2D FTOPT lineshapes reveal contributions from higher-order correlations such as the EID and EIS mechanisms discussed above [87]. Therefore, unlike 2D FT spectra of weakly interacting excitations, the rephasing and nonrephasing spectral surfaces cannot be combined to yield a purely absorptive 2D spectrum, as discussed in Section 2.1. Rather the complex 2D spectral lineshapes contain valuable information about about higher-order correlations in their own right, albeit convolved with the coupled two-particle (exciton) correlations. Similar to the spectrally resolved one-dimensional FWM measurements described above, biexciton contributions are largely overlapped with the spectral contribution from exciton coherences observed in the temporally-resolved one-quantum 2D FTOPT measurements presented here.

The two-quantum 2D FTOPT measurements presented here isolate higher-order correlations, such as biexcitons, from two-particle correlations. Unlike previous four-wave mixing experiments on single quantum dots [118] and quantum wells [119], the two-quantum measurements not only track the phase evolutions of two-quantum coherences at optical frequencies, but also correlate them to optical one-quantum coherences, allowing the phenomena to be isolated and studied even when their signatures cannot be separated spectrally. The two-quantum 2D FTOPT results include measurements obtained with a variety of experimental conditions, such as varying excitation wavelength, polarization, and density of excited carriers which are relevant to the different types of many-body phenomena. For instance, the proportion of free electron-hole pairs that are excited may be adjusted by tuning the excitation wavelength, thereby modifying the strength of spectral signatures resulting from exciton-

free carrier interactions. Varying the polarizations of the excitation fields controls which types of exciton interaction phenomena contribute to the signal. Varying the carrier density influences the strength of many-body effects that modify exciton and biexciton dephasing.

5.2 2D FTOPT experiments on GaAs quantum wells

The 2D FTOPT measurements presented here (obtained using the optical setup described in Chapter 3) were made on a multiple quantum well sample that consisted of 10 alternating layers of 10 nm thick GaAs separated by 10 nm thick barriers of $Al_{0.3}Ga_{0.7}As$ which was grown by molecular-beam epitaxy on a GaAs substrate. The substrate was etched away and the sample was affixed to a sapphire disc. The sample was held below a temperature of 10 K in a cold-finger cryostat for all 2D FTOPT measurements. The absorption spectrum of the sample at 10 K is shown in Fig. 5-4(a). The HX and LX absorption peaks differ by approximately 1.5 THz, or 6 meV, due to quantum confinement as discussed above.

The average power in the four beams produced by the multidimensional optical spectrometer apparatus described in Section 3.2, each of which carried either one pulsed excitation field or reference field, was maintained at or below 2 mW by passing the beam from the unamplified Ti:sapphire laser (with a pulse repetition rate of 92.5 MHz) through a half-wave plate/polarizer pair prior to the experimental setup. The range of coherently generated carrier densities over which the measurements were obtained is given in Fig. 5-4(b). The reference field propagated through the sample 1.00 ps before emission of the signal, but its power was reduced by a factor of 1000 compared to the power of the excitation beams, which was achieved by inserting a neutral density filter that was chemically etched in order to remove three-quarters of the coated area such that only the reference field would be attenuated.

The polarizations of the fields $\vec{E}_A$ and $\vec{E}_C$ can be used to select the spin of the

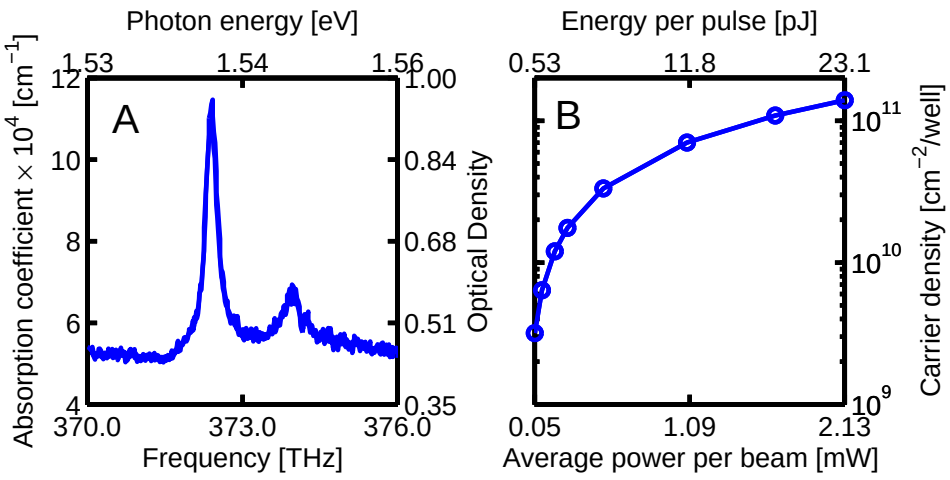

Figure 5-4: (a) Absorption coefficient (left axis) and optical density (right axis) as a function of photon energy and frequency for the GaAs QW sample at 10 K. The HX and LX exciton absorption frequencies are 372.35 THz and 373.96 THz (1.539 and 1.546 eV), respectively. (b) The coherently generated density of carriers in the GaAs quantum wells sample as a function of the excitation pulse energy and average power per beam when using a 15 cm focal length lens to focus the beams to an excitation spot radius of 40 μm.

exciton population that exists during τ_2 in the rephasing and non-rephasing measurements. Right (σ^+) or left (σ^-) co-circularly polarized fields create populations of spin-up or spin-down excitons, respectively, while cross-circularly polarized fields do not create any population gratings. Collinearly polarized fields create two population gratings of spin-up and spin-down excitons that have the same spatial phase as shown in Fig. 5-5(a). Cross-linearly polarized fields create two population gratings that are 180° out of phase, as illustrated in Fig. 5-5(b), such that there is no net population grating. The coherent contributions to the 2D FTOPT signal resulting from EID and EIS depend on the presence of an exciton population grating (see Section 4.3), whereas biexciton formation requires the excitation of two exciton coherences of opposite spin. Therefore, sequences of cross-linearly or cross-circularly polarized excitation fields can be used to distinguish between the features resulting from different many-body phenomena. Circular polarizations of the input beams, controlled via individual quarter-wave plates, selected which biexciton coherences (pure or mixed) were observed, as described in Fig. 5-3. A separate quarter-wave plate common to

all beams was used in conjunction with the individual wave plates to change the fields to v-polarized or h-polarized, eliminating the interaction-induced many-body contributions, but keeping only the exciton and biexciton contributions to the signal. The polarization of the reference field was adjusted to match the polarization of the signal, which depends on the polarization of the excitation fields.

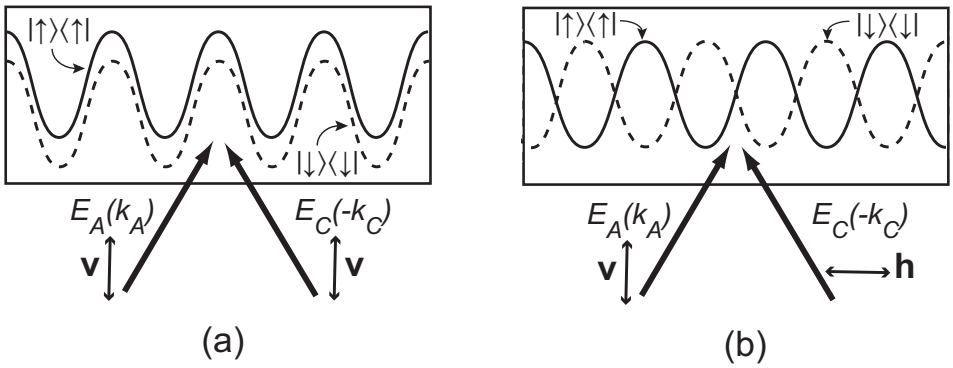

Figure 5-5: (a) Collinearly polarized excitation fields $\vec{E}_A$ and $\vec{E}_C$ produce two exciton populations (spin-up and spin-down) in a cosinusoidally-modulated spatial grating pattern in the sample with the same spatial phase. (b) Cross-linearly polarized excitation fields produce two exciton population gratings that are sinusoidally modulated and 180° out of phase, yielding no spatial modulation of the total exciton population.

The fields, $\vec{E}_A$, $\vec{E}_B$ and $\vec{E}_C$, were used to excite the third-order polarization which results in signal, $\vec{E}_S(\tau_1, \tau_2, t)$, that propagates into the background-free, phase-matched direction $\vec{k}_S = \vec{k}_A + \vec{k}_B - \vec{k}_C$ collinear with the reference field, $\vec{E}_R$. The signal emission and reference fields were superposed in a spectrometer ("spectral interferometry" [75]) and a record of the spectral fringes as a function of ω, which have a periodicity proportional to the time delay between the two fields, was accumulated as the excitation pulse delays, τ_1 and τ_2, to obtain the complex signal $\tilde{S}(\tau_1, \tau_2, \omega)$ without the need for numerical Fourier transformation over the signal emission time, t. The one-quantum rephasing and non-rephasing pulse sequences (also called "S1" and "S2" using nonlinear spectroscopy terminology [91]), illustrated in Fig. 5-6(a) and (b), were used with $\tau_2 = 0$, and Fourier transformation of $\tilde{S}(\tau_1, \omega)$ yielded the one-quantum complex 2D FTOPT spectral surfaces $\tilde{S}(\omega_1, \omega)$ which exhibited exciton absorption peaks along ω_1 and their associated emission along ω. The two-quantum

pulse sequence (also known as "S3") illustrated in Fig. 5-6(c) was used with $\tau_1 = 0$, and Fourier transformation of $\tilde{S}(\tau_2, \omega)$ yielded the complex two-quantum 2D FTOPT spectral surfaces $\tilde{S}(\omega_2, \omega)$ which revealed the two-quantum coherences along ω_2 and their associated exciton emission along the ω coordinate. In recent experiments not presented here, both τ_1 and τ_2 have been varied and 3D spectral solids, $\tilde{S}(\omega_1, \omega_2, \omega)$, have been extracted [120].

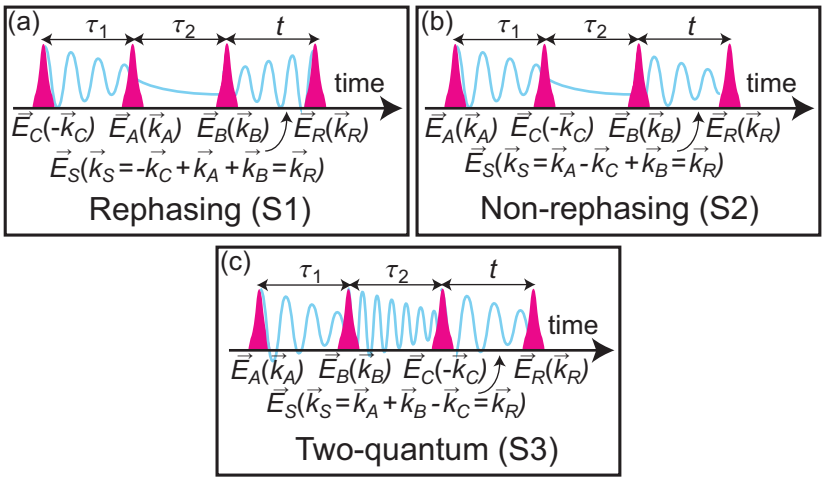

Figure 5-6: The time-ordering of the excitation fields $\vec{E}_A$, $\vec{E}_B$ and $\vec{E}_C$ determines the type of multiple particle correlations that contribute to the signal, which is measured by interferometric detection of the signal field, $\vec{E}_S$, by the reference field, $\vec{E}_R$, obtained in 2D FTOPT spectroscopy experiments. Specifically, the arrival time of the field which contributes its negative wavevector component to the signal, designated as $\vec{E}_C$, and the scanned interpulse delay, τ_1 or τ_2, determines whether (a) rephasing, (b) non-rephasing, or (c) two-quantum signal is observed. One-quantum coherences are observed during the delay τ_1 in (a), (b), and (c), but two-quantum coherences are only observed during the delay τ_2 in (c). The signal field is detected during the emission time, t.

As described in Chapter 3 the pulse shaper permits relative delay times between pulses to be varied while maintaining the relative optical phase relationships constant. In particular, a reference frequency ω_0 within the spectral bandwidth of the pulse is selected and its phase in all four fields is held constant by leaving the four corresponding phase profiles implemented by the pulse shaper fixed throughout the experiment. As relative pulse delays are varied, the relative phases at ω_0 remain constant and the relative phases, and thus the signal field, at ω_e shift slightly, proportional to the

frequency difference $\omega_e - \omega_0$. This is precisely analogous to rotating frame detection in NMR [78]. The reference frequency selected for these measurements was $\omega_0 =$ 368.00 THz based on careful calibration of the dispersed frequencies of the pulses versus horizontal SLM pixel. The calibration was confirmed by measuring the HX coherent oscillation frequency, $\omega_X = 4.35$ THz, in non-rephasing measurements and the quantum well absorption peak at 372.35 THz. See Fig. 5-7.

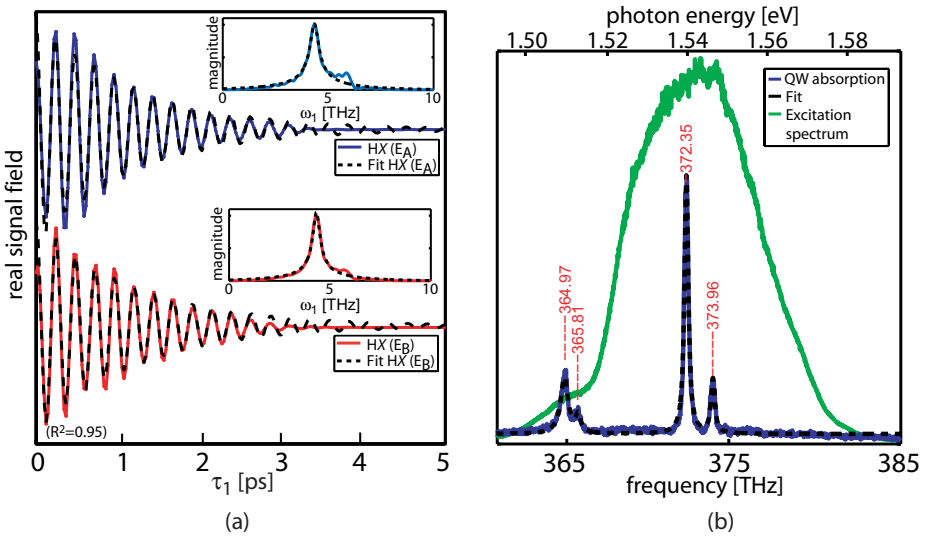

Figure 5-7: (a) HX transients vs. τ_1 extracted from non-rephasing measurements where field $\vec{E}_A$ (blue line) or $\vec{E}_B$ (red line) acted as the excitation pulse. The oscillations are shifted into the rotating frame because only the envelopes, not the carrier waves, of $\vec{E}_A$ and $\vec{E}_B$ are delayed. Fourier transforms of the transients to the absorption frequency domain, ω_1, are shown in the corresponding insets. The data were fitted (dotted lines) with a single-exponentially decaying cosine function in the time domain and a single Lorentzian function in the frequency domain. For excitation field $\vec{E}_A$ ($\vec{E}_B$) the fitted center frequency, ω_X, was 4.35±0.01 (4.33±0.01) THz within a 95% confidence interval. (b) The absorption spectrum (blue line) of the quantum well sample at 10 K with nonlinear least-squares fit (black line). The peaks with center frequencies 372.35±0.00 THz and 373.96±0.01 THz are the HX and LX absorptions. We confirm the experimentally specified value for the carrier frequency ω_0 (368.0 THz) by comparing the HX absorption with the fitted HX transient in (a). The two peaks centered near 365 THz are due to absorption by the bulk GaAs substrate upon which the quantum well sample was deposited. The spectrum of the excitation and reference fields (green line) is centered at approximately 373 THz.

For the complex one-quantum and two-quantum spectral surfaces, the spatiotemporal pulse shaper was employed to determine the phase shift between the signal and

reference fields by temporally overlapping the time-zero emission signal with the reference pulse and varying the carrier-envelope phase shift of one of the excitation fields. This determines the phase offset of the signal field from the reference field, which can be added as a phase shift to one of the excitation pulses during the experiment or multiplied with the entire data set after the measurement. The value of signal-reference phase offset used to correctly phase the complex 2D FTOPT spectra presented here was determined by temporally overlapping the time-zero signal field with the reference field, which were spatially overlapped in a spectrometer, and separately scanning the carrier-envelope phase shift, $\phi^{(0)}$, of each of the excitation pulses over several cycles of 2π. The resulting spectral interferogram was integrated over the HX exciton emission frequency which yielded the traces $S(\omega_{HX}, \phi^{(0)})$ presented in Fig. 5-8. Each trace was

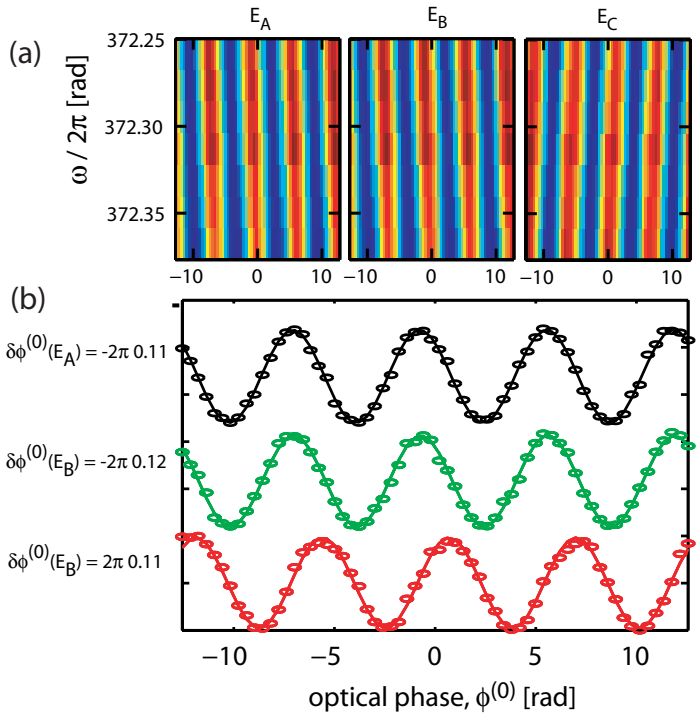

Figure 5-8: An example of how the overall signal-reference phase shift was determined for 2D FTOPT measurements. In (a) are the spectral interferogram versus optical phase of each excitation field is plotted for a frequency region that covers the HX exciton resonance. In (b), the spectral interferograms are integrated (dots) and fitted (lines) to determine the optical phase shift, $\delta\phi^{(0)}$, for each excitation field. The fit results are listed to the left of (b).

fitted to a cosine of the form $S(\omega_{HX}, \phi^{(0)}) = A \times \cos(\Omega\phi^{(0)} - \delta\phi^{(0)}) + C$ to determine the phase shift $\delta\phi^{(0)}$. The average of the three values of $\delta\phi^{(0)}$ was then applied to one of the excitation fields, in addition to linear spectral phase shifts applied during the measurement. This phasing procedure was repeated for each measurement where the excitation polarization was varied.

5.2.1 One-quantum 2D FTOPT measurements

Rephasing (S1) measurements

For rephasing 2D FTOPT measurements, field $\vec{E}_C$ arrives first at the sample to generate exciton coherences which oscillate with frequency ω_e, and after a variable delay τ_1, interaction with $\vec{E}_A$ produces exciton populations in a transient grating pattern with wavevector $\vec{k}_A - \vec{k}_C$. The presence of the exciton population spatial grating diffracts field $\vec{E}_B$, incident at the phase-matching or Bragg angle, to yield the coherently scattered signal $\vec{E}_S$ with wavevector defined as $\vec{k}_S = -\vec{k}_C + \vec{k}_A + \vec{k}_B$. The last field $\vec{E}_B$ also reverses the temporal phases of the exciton coherences that evolved during τ_1 such that the decay of $\vec{E}_S(t)$ yields the homogeneous dephasing time since any inhomogeneous dephasing due to local variation in the frequency is reversed due to the "rephasing" imparted by $\vec{E}_B$. The rephasing signal contributions can be described in terms of the double-sided Feynman diagrams summarized in Fig. 5-9 for the nine-level system illustrated in Fig. 5-3. Since the last field $\vec{E}_B$ also reverses the temporal phase of the exciton coherences that evolve during τ_1, by convention, the exciton coherence frequency is displayed on the negative ω_1 axis after 2D FT of the measured signal.

Here I will present one-quantum rephasing (S1) 2D FTOPT spectra that were obtained with varied excitation field polarizations and pulse sequences. The complex 2D lineshapes reveal contributions from higher-order correlations (such as the EID and EIS mechanisms discussed above) that are convolved with the coupled two-particle (exciton) correlations. Note that in the rephasing measurements presented here, all the 2D spectral magnitudes have been normalized so that the relative amplitudes of

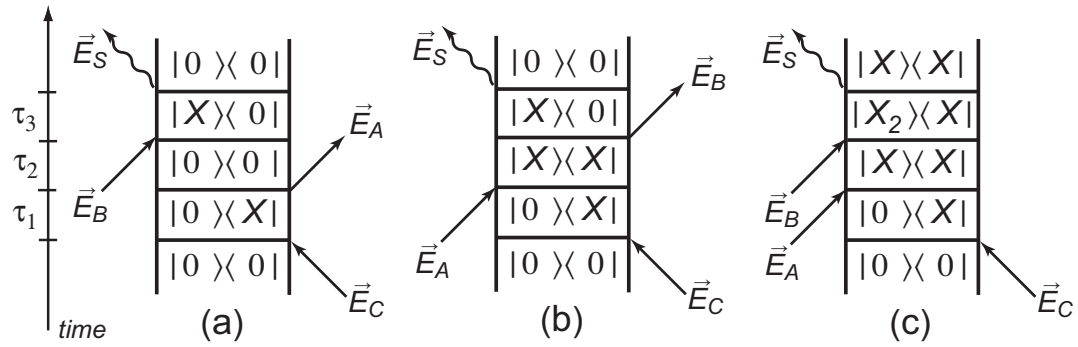

Figure 5-9: Feynman pathways relevant to one-quantum rephasing 2D FTOPT measurements. Pathways illustrated by diagrams (a) and (b) describe the diagonal and off-diagonal peaks observed in the 2D spectra since the first and last excitation fields, $\vec{E}_C$ and $\vec{E}_B$, respectively, are broadband such that they are resonant with both the HX and LX exciton coherence frequencies. In (a) the second field $\vec{E}_A$ stimulates emission from the exciton state such that a ground state population exists during τ_2. In (b), power from the second field $\vec{E}_A$ is absorbed such that either a HX or LX population exists, or a superposition of HX and LX states evolves, during τ_2. In (c), light from the final field can be absorbed such that a superposition of biexciton and exciton states evolves during the final emission time period. According to the selection rules defined in Fig. 5-3, co-circularly polarized fields will excite mixed (MX_2) biexciton-exciton coherences while cross-circularly polarized fields will excite pure (HX_2 and LX_2) biexciton-exciton coherence. Due to the biexciton binding energy, the signal contribution described by this pathway will appear red-shifted from the signals resulting from the diagrams in (a) and (b).

peaks within each spectrum can be compared for the different excitation polarization cases. However, the ratio of spectral magnitudes integrated over all frequencies for the series of rephasing spectra (co-circular:cross-circular:cross-linear) presented here goes as 1.9 : 1.0 : 1.1. The contour intervals of the 2D spectra are plotted at 2% of the maximum peak amplitude. The reported coordinates, (ω, ω_1), of the salient 2D spectral features are the positions along the emission and absorption coordinates.

(I) Co-circularly polarized S1

The one-quantum rephasing 2D spectra for co-circularly polarized excitation are shown in Fig. 5-10. The magnitude of the 2D spectrum exhibits four distinct spectral features. Note that spectral interferometry detection gives the signal field as a function of the absolute emission frequency, ω, so the carrier frequency, ω_0, was subtracted from the emission frequency so both coordinates are represented in the rotating frame. The diagonal peaks along the $\omega_1 = -(\omega - \omega_0)$ line are HX and LX exciton resonances,

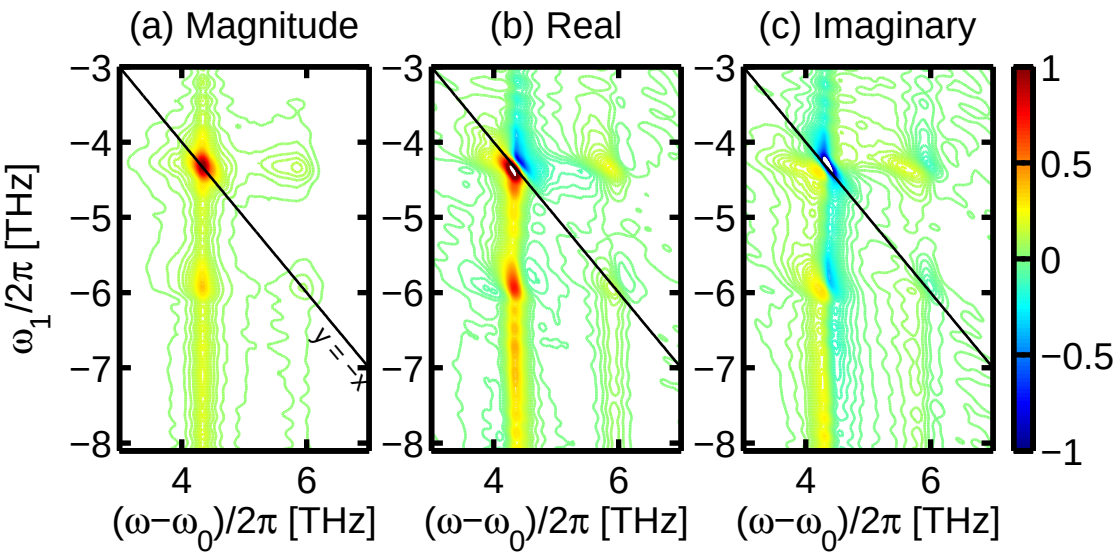

Figure 5-10: The (a) magnitude, (b) real, and (c) imaginary parts of the one-quantum rephasing 2D FTOPT spectra of GaAs quantum wells obtained with co-circularly polarized excitation fields. The contour lines are plotted at 2% intervals of the maximum signal magnitude.

and the off-diagonal peaks indicate coupling of these states. The separation of these spectral features on a two dimensional surface allows one to discriminate the quantum

mechanical pathways through which the optically excited coherences evolved. Typically, in rephasing 2D FT spectra the diagonal and off-diagonal peaks are elongated along the diagonal which indicates inhomogeneous broadening of the resonances, and the inhomogeneous and homogeneous linewidths can be extracted from the widths of the features parallel and perpendicular to the diagonal, respectively. However, for the GaAs quantum well sample in the present measurements, the dephasing time of the exciton coherence, which is approximately 10 ps, is longer than the intensity roll-off of the SLM delayed pulses (see section 3.3.3 for further discussion) and this causes the four main one-quantum rephasing spectral features to appear rounded with the instrumentally limited width rather than elongated.

The off-diagonal peak that represents the quantum mechanical pathway where a HX coherence evolved during τ_1 but a LX coherence evolved during t with approximate coordinates of (5.9, -4.3) THz exhibits a red-shifted shoulder, which is indicative of a mixed MX_2 biexciton-LX exciton coherent oscillation during the emission period. However, the opposite off-diagonal peak with approximate coordinates of (4.3, -5.9) THz is rounded uniformly, in other words, it does not exhibit a red-shifted shoulder, although mixed MX_2 biexciton–HX exciton coherences are also expected to emit during the emission time. The absence of the feature is likely due to interference with signal contributions from higher-order correlations and this is discussed further in connection with rephasing 2D FTOPT measurements obtained using cross-linearly polarized excitations fields which are presented below. Biexciton-exciton signal contributions are shifted from exciton signal contributions proportional to a binding energy, which is discussed further in connection with results from two-quantum 2D FTOPT measurements in Section 5.2.2.

A vertically elongated feature that extends from the LX exciton absorption to an ω_1 frequency of approximately -10 THz indicates the excitation of free electron-hole pairs during τ_1 that interact with the HX exciton through an EID mechanism and emit at the HX exciton coherence frequency, as was shown previously [88]. A vertically elongated feature also extends from the LX exciton emission, which is more prominent in the real and imaginary spectral surfaces.

As described previously [87], the complex 2D spectral lineshapes indicate contributions from higher-order correlations. The real part of spectral surface, shown in Fig. 5-10(b), has a mainly dispersive lineshape, rather than an absorptive lineshape which would be characteristic of non-interacting excitations. The imaginary part of the spectral surface, shown in Fig. 5-10(c), is largely absorptive but negative, whereas a largely positive absorptive lineshape is expected given the Feynman pathways in 5-9(a) and (b) that should describe the signal contribution. The reversal of the lineshapes between real and imaginary surfaces indicates a phase shift in the signal field, however, I was careful to remove any phase offset between the excitation fields and reference fields using the phasing procedure described in Section 5.2. Rather, the changes in the complex spectral 2D lineshapes are induced by higher-order correlations which were explained in Chapter 4 in the context of the optical Bloch equations (OBE) where phenomenological EID and EIS terms have been included. These so-called modified optical Bloch equations (MOBE) were used to model the one-quantum 2D lineshapes of the real spectral surfaces presented in Fig. 5-10(b) for co-circularly polarized excitation fields. The measured real spectral surface for the HX diagonal peak is presented in Fig. 5-11 alongside the results obtained with the MOBE model for a two-level system which represents exciton-ground state coherences only. The predominantly dispersive lineshape in the measured 2D spectrum is comparable to the MOBE results where only EIS effects are included.

(II) Cross-circularly polarized S1

The one-quantum rephasing 2D spectra for cross-circularly polarized excitation are shown in Fig. 5-12. The magnitude of the 2D spectrum exhibits the four main diagonal and off-diagonal peaks and the vertically elongated feature as in the co-circular polarization case. However, for cross-circularly polarized light, only HX_2 and LX_2 biexcitons should be excited, therefore the HX diagonal peak exhibits a shoulder at ω_{eb} which is red-shifted from the exciton coherence frequency ω_e due to a binding energy, which is indicative of a HX_2 biexciton–HX exciton coherent oscillation during the emission period. The LX_2 biexciton-exciton feature is too weak to be seen here

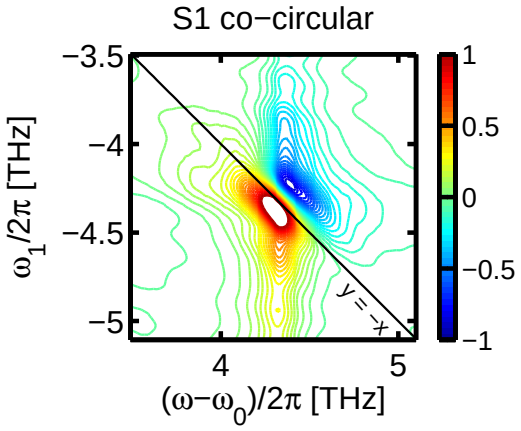

(a) Real part of the measured S1 spectrum using co-circular excitation

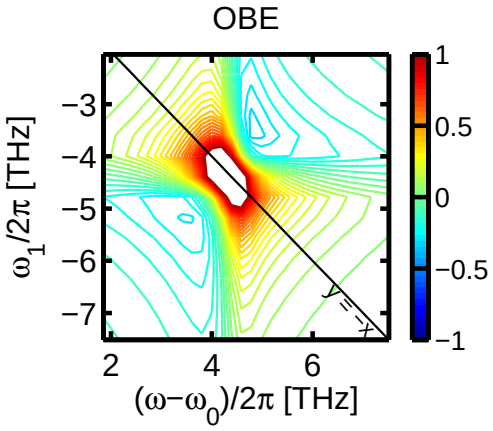

(b) Calculated using the optical Bloch equations

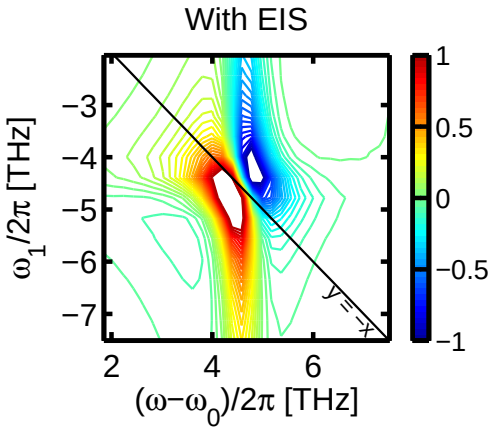

(c) Calculated using the MOBE with excitation-induced shift (ω'=25 THz/m^3)

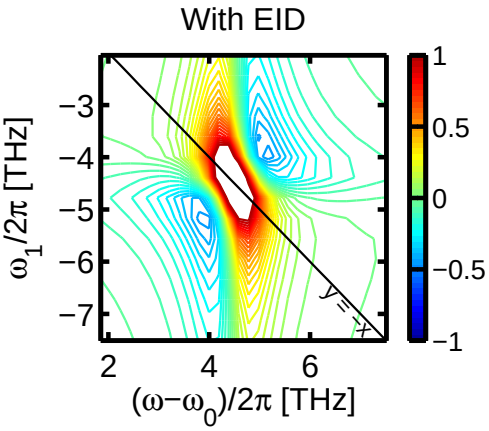

(d) Calculated using the MOBE with excitation-induced dephasing (γ'=25 THz/m^3)

Figure 5-11: Real part of the rephasing 2D FTOPT spectra of GaAs quantum wells using co-circularly polarized excitation fields compared to results from the modified optical Bloch equations (MOBE).

since the LX transition dipole is one-third that of the HX exciton transition dipole. In the real part of the rephasing spectral surface, the diagonal peak is mostly positive for higher emission frequencies, but mostly negative for lower emission frequencies. The change in sign indicates that the HX-ground state coherence emits into the final field, $\vec{E}_B$, while the HX_2 biexciton–HX exciton coherence absorbs from $\vec{E}_B$. Note that overall the real 2D lineshape is largely dispersive, indicating that a higher-order correlation, namely EIS, is highly convolved with the one-quantum coherences observed.

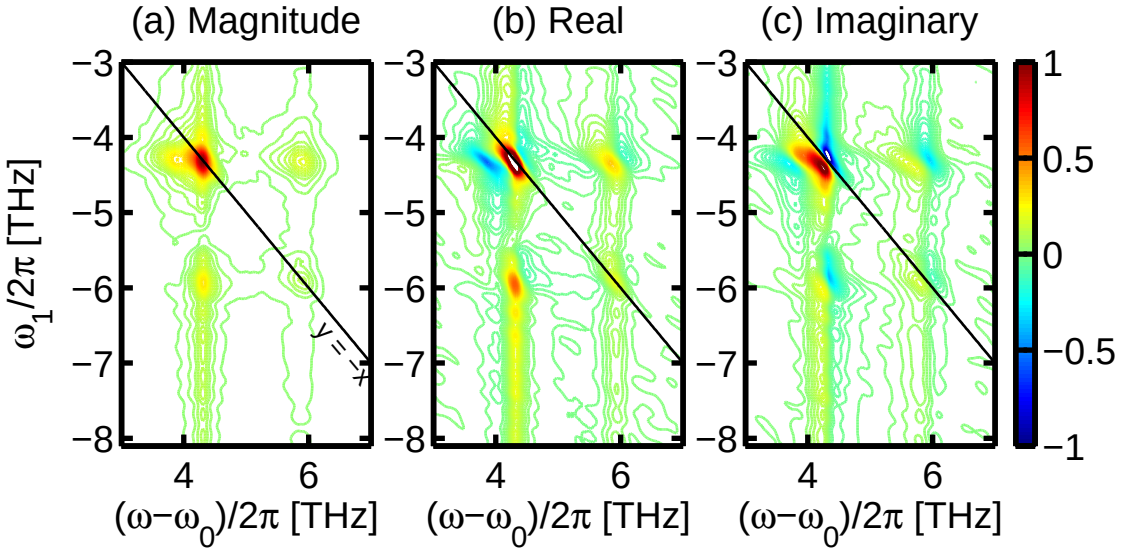

Figure 5-12: The (a) magnitude, (b) real, and (c) imaginary parts of the one-quantum rephasing 2D FTOPT spectra of GaAs quantum wells obtained with cross-circularly polarized excitation fields, i.e. the first field, $\vec{E}_C$, was right (σ^+) circularly polarized and the second field, $\vec{E}_A$, was left (σ^-) circularly polarized. The final excitation field, $\vec{E}_B$, was σ^--polarized and the reference field, $\vec{E}_R$, was σ^+-polarized.

(III) Cross-linearly polarized S1

The one-quantum rephasing 2D spectra for cross-linearly polarized excitation are shown in Fig. 5-13. As described in Section 5.2, this excitation polarization scheme should eliminate the spectral contributions that are due to many-body effects such as EID and EIS, but keeps signal contributions from biexciton coherences. Since linearly polarized light can be described as a superposition of right and left circularly polarized

light, both pure and mixed biexciton-exciton coherences will be excited. In general, the biexciton-exciton contributions appear stronger relative to the HX exciton feature at approximately (4.3, -4.3) THz. Unlike the four main peaks in Fig. 5-10 and Fig. 5-12, a red-shifted shoulder is observed for both the diagonal and off-diagonal peaks. This observation supports the claim that contributions from higher-order correlations involving the HX exciton could account for the rounded 2D lineshape of one of the off-diagonal peaks in Fig. 5-12.

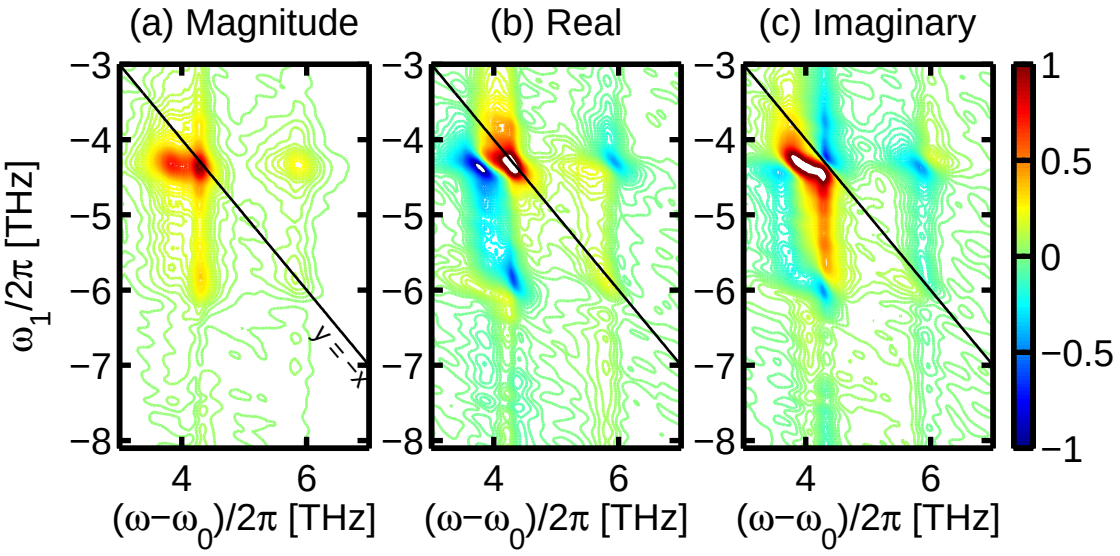

Figure 5-13: The (a) magnitude, (b) real, and (c) imaginary parts of the one-quantum rephasing 2D FTOPT spectra of GaAs quantum wells obtained with cross-linearly polarized excitation fields, i.e. the first field, $\vec{E}_C$, was vertically (v) polarized and the second field, $\vec{E}_A$, was horizontally (h) polarized. The final excitation field, $\vec{E}_B$, was h-polarized and the reference field, $\vec{E}_R$, was v-polarized.

The real part of the 2D spectral surface, shown in Fig. 5-13(b), exhibits a primarily absorptive lineshape and this lineshape differs from the real 2D lineshapes for the co-circular and cross-circular excitation cases presented above where the lineshapes were largely dispersive. This observation is consistent with the interpretation that excitation by cross-linearly polarized fields eliminates signal contributions due to interaction-induced many-body effects since a net exciton population which would drive those contributions does not exist for this measurement. Rather, in this

measurement, the real 2D lineshapes are generally equivalent to the 2D lineshapes produced by the optical Bloch equations for a cascaded three-level model, which is presented in Section 4.2.1.

Non-rephasing (S2) measurements

For non-rephasing 2D FTOPT measurements, field $\vec{E}_A$ arrived first to generate exciton coherences followed by interaction with field $\vec{E}_C$ after a variable time delay τ_1 which produces exciton populations in a transient grating pattern with wavevector $\vec{k}_A - \vec{k}_C$. The presence of the exciton population spatial grating diffracts field $\vec{E}_B$ to produce the signal field which propagates in the same wavevector-matched direction as the rephasing signal. However, in this case, the last field $\vec{E}_B$ does not reverse the temporal phase of the exciton coherences excited by $\vec{E}_A$, therefore, their oscillation frequency is displayed on the positive ω_1 axis by convention. The non-rephasing signal contributions can be described in terms of the double-sided Feynman diagrams summarized in Fig. 5-14 for the nine-level system illustrated in Fig. 5-3.

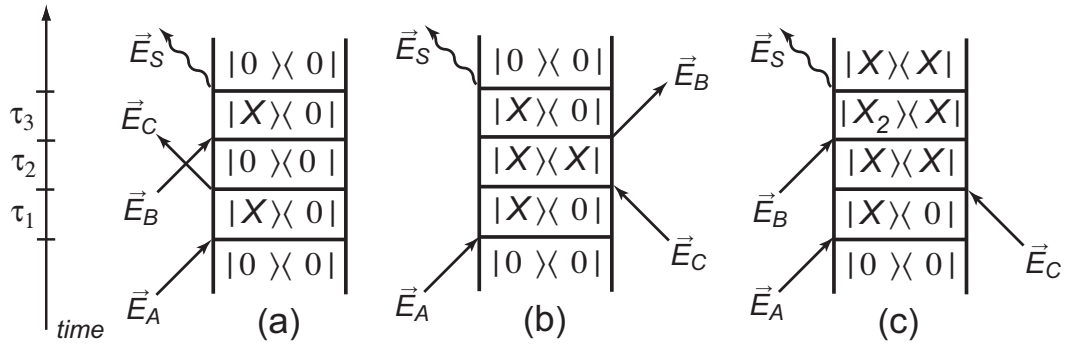

Figure 5-14: Feynman pathways relevant to one-quantum non-rephasing 2D FTOPT measurements. The coherences or populations that evolve during the interpulse delays describe signals similar to the diagrams for the rephasing measurements given in Fig. 5-9. The rephasing and non-rephasing diagrams only differ by a sign change with respect to the exciton-ground state coherence frequency that evolves during the absorption time, τ_1.

The one-quantum non-rephasing (S2) 2D FTOPT spectra that were obtained with varied excitation field polarizations and pulse sequences, similar to the rephasing spectra presented above, are shown in Fig. 5-15. Spectral features similar to

those found in rephasing spectra, such as diagonal and off-diagonal peaks (where the diagonal is now defined as $\omega_1 = \omega - \omega_0$) and complex 2D spectral lineshapes that indicate many-body contributions convolved with spectral signatures from coupled two-particle correlations, are also present in the non-rephasing 2D spectra. For instance, the real parts of the non-rephasing 2D FTOPT spectra for the cases of co-circular and cross-circular excitation polarization exhibit primarily dispersive lineshapes which indicate contributions from EIS, as was shown using the numerical calculations involving the modified optical Bloch equations in Chapter 4. Furthermore, the real part of the non-rephasing 2D spectrum obtained using cross-linearly polarized excitation fields has 2D lineshapes that are absorptive, indicating that contributions from higher-order correlations have been suppressed. All the 2D spectral magnitudes have been normalized so that the relative amplitudes of peaks within each spectrum can be compared for the different excitation polarization cases. The ratio of spectral magnitudes integrated over all frequencies for the series of non rephasing spectra (co-circular:cross-circular:cross-linear) presented here goes as $1.5 : 1.2 : 1.0$.

Distortions in non-rephasing (S2) measurements

As stated above, field $\vec{E}_A$ is first to arrive at the sample to generate an exciton coherence which evolves during τ_1. It contributes one of the positive wavevector components to the signal field $\vec{E}_S$ which propagates in the wavevector-matched direction $\vec{k}_S = \vec{k}_A + \vec{k}_B - \vec{k}_C$. Since field $\vec{E}_B$ also contributes its positive wavevector component to the signal field, a non-rephasing 2D FTOPT signal can be obtained by switching the time-ordering of the fields such that $\vec{E}_B$ is the first field to interact with the sample and $\vec{E}_A$ is the last field to arrive at the sample. For all intents and purposes, the two non-rephasing 2D FTOPT spectra obtained when field $\vec{E}_A$ or $\vec{E}_B$ is first to interact with the sample are identical, however, in practice, differences in the pulse intensities, frequency content, phase profiles, etc. can cause differences between the resulting spectra. When using spatiotemporal pulse shaping to generate the interpulse delays between the excitation fields, some distortions to the these fields can be caused by aberrations from the imaging optics in the apparatus.

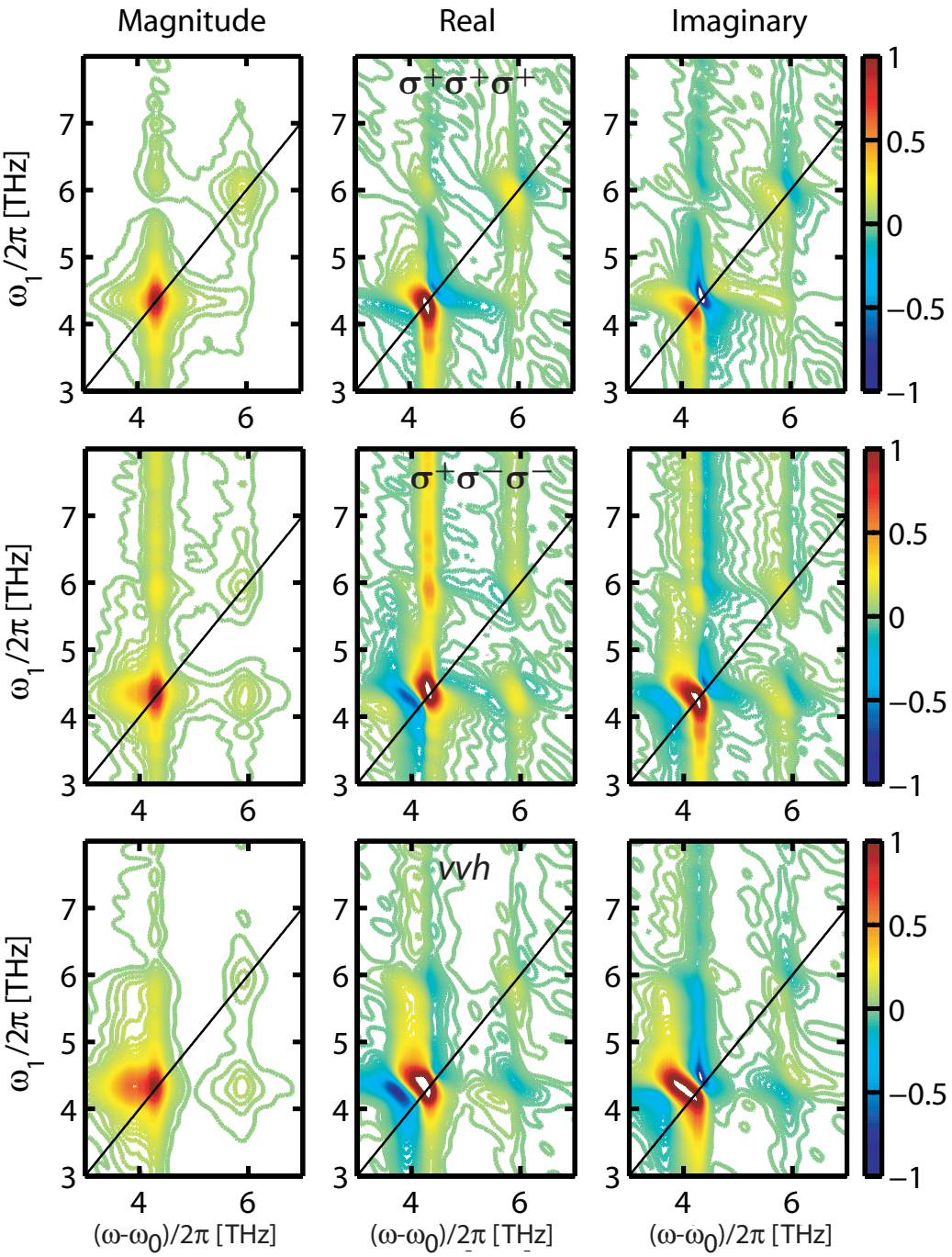

Figure 5-15: Magnitude (left column), real (middle column) and imaginary (right column) parts of the complex non-rephasing 2D FTOPT spectra of GaAs quantum wells for different excitation polarizations. First row: co-circularly polarized excitation. Second row: cross-circularly polarized excitation. Third row: cross-linearly polarized excitation. The contours are plotted in intervals that are 2% of the maximum peak amplitude.

One of the pulse distortions is also relevant to two-quantum 2D FTOPT measurements. Specifically, the beams containing the fields $\vec{E}_A$ and $\vec{E}_B$ may not be properly focused to the 2D spatial light modulator (SLM) after spatial separation of their frequency components by the diffraction grating because of off-axis spherical aberrations produced by the cylindrical lens. Such aberrations could cause differences in the SLM pixel-to-frequency calibrations for each field, and if these differences are not carefully measured, the carrier frequency referenced by each individual field will be different. This could cause an incorrect interpretation of the spectral features found in two-quantum 2D FTOPT spectra that are caused by higher-order correlations excited by fields $\vec{E}_A$ and $\vec{E}_B$, and, therefore, depend not only on the phases, but the carrier frequencies of those fields as well, since 2D FTOPT signals generated by SLM-delayed pulses are detected in the rotating frame.

Differences in the frequency dispersion of fields $\vec{E}_A$ and $\vec{E}_B$ across the SLM surface can be observed in the non-rephasing 2D FTOPT spectra obtained using co-circular excitation presented in Figs. 5-16(a) and 5-16(b). The projections of the spectral magnitudes to the ω_1 axis were fitted separately to a Lorentzian function in order to compare the center frequencies of the diagonal peaks at the HX exciton resonance. For the non-rephasing measurement where field $\vec{E}_A$ or $\vec{E}_B$ excited one-quantum exciton coherences, the fitted center frequency was 4.35±0.01 or 4.43±0.01 THz, respectively. Since the values obtained by the fit differ by more than the frequency resolution of the SLM, which is approximately 0.05 THz per pixel for a 1400 groove/mm diffraction grating and 12.5 cm focal length cylindrical lens where the pixel size is 24 μm, I shifted the previously determined frequency-to-pixel calibration curve corresponding to the frequency dispersion of field $\vec{E}_B$ across the SLM by approximately 0.10 THz, or two pixels. The calibration for field $\vec{E}_A$ was kept unchanged since the fitted center frequency along the ω_1 axis (4.35 THz) corresponded to the HX exciton transition frequency in the measured linear absorption spectrum (see Fig. 5-7(b)) when added to the chosen reference frequency, 368.00 THz. The frequency of one-quantum exciton coherence excited by field $\vec{E}_C$ could be characterized as well using a rephasing measurement, but since this field remains at time-zero for S2 and S3 measurements,

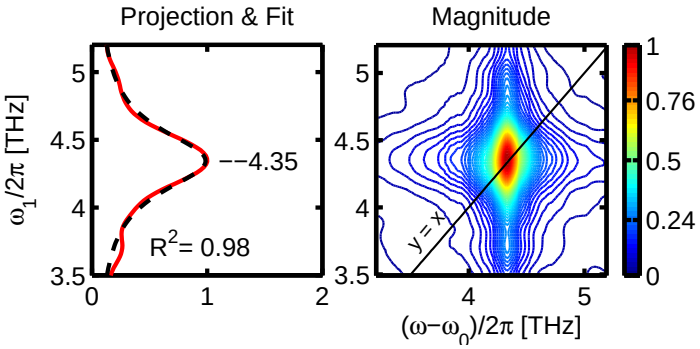

(a) S2 spectrum where field $\vec{E}_A$ arrives first.

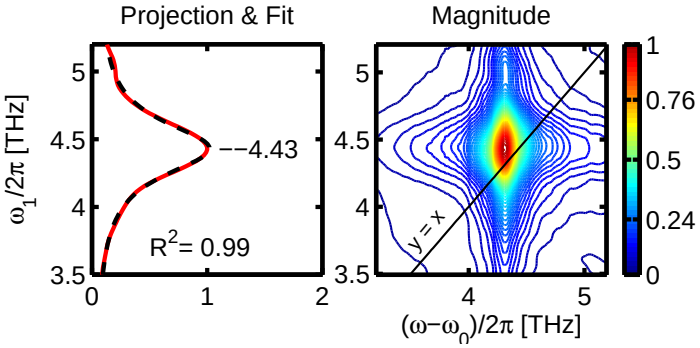

(b) S2 spectrum where field $\vec{E}_B$ arrives first.

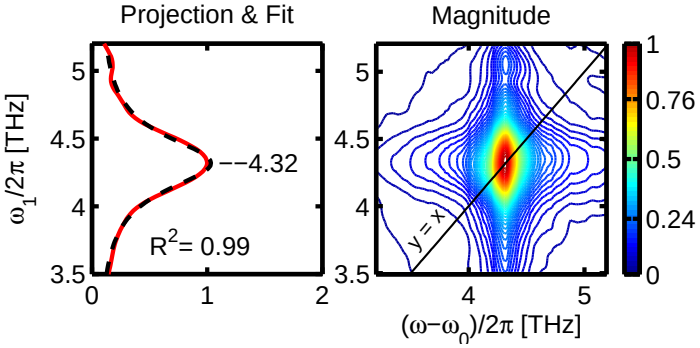

(c) Field $\vec{E}_B$ arrives first with corrected SLM frequency dispersion

Figure 5-16: The effect of an incorrect SLM pixel to frequency calibration on the 2D FTOPT spectral magnitude.

Table 5.1: Center frequency in THz along the ω_1 axis of the diagonal peaks from non-rephasing 2D FTOPT spectra where the fields $\vec{E}_A$ or $\vec{E}_B$ served as the first excitation field. The absorption peaks were fitted to multiple-Lorentzian lineshapes using nonlinear regression. The uncertainties reported represent the 95% confidence interval for the fitted parameters.

One-quantum absorption frequency	First field was $\vec{E}_A$	First field was $\vec{E}_B$
HX (co-circular)	4.35±0.01	4.32±0.01
LX (co-circular)	5.97±0.01	5.96±0.02
HX (cross-circular)	4.35±0.01	4.33±0.01
LX (cross-circular)	5.97±0.01	5.98±0.05
HX (cross-linear)	4.34±0.01	4.33±0.01
LX (cross-linear)	5.98±0.02	5.93±0.02

the actual frequency referenced for this field is not significant. The actual value of the reference frequency for the reference field $\vec{E}_R$ may be ignored as well, since ultimately, field $\vec{E}_R$ is used in the frequency domain for interferometric detection of the signal and its delay is not adjusted during the experiment.

The non-rephasing 2D FTOPT spectrum was measured for excitation by field $\vec{E}_B$ with the new frequency-to-pixel calibration and the center frequency of the HX exciton resonance was fitted to 4.32±0.01 THz, shown in Fig. 5-16(c). The HX and LX exciton absorption frequencies in the rotating frame were determined for non-rephasing 2D FTOPT measurements using excitation fields $\vec{E}_A$ and $\vec{E}_B$ for different polarizations and the fitted values, listed in Table 5.1, were used to determine the biexciton binding energy in conjunction with two-quantum 2D FTOPT measurements in Section 5.2.2. The real 2D spectral lineshapes in Fig. 5-17(b) and Fig. 5-17(c) are nearly identical, with the only difference being that the peak in Fig. 5-17(b) is slightly red-shifted along the ω_1 coordinate. This confirms that distortions of the excitation fields imparted by non-ideal imaging optics in the pulse shaper, which creates differences in the SLM pixel-to-frequency calibration, only changes the position of peaks and not their complex 2D lineshapes.

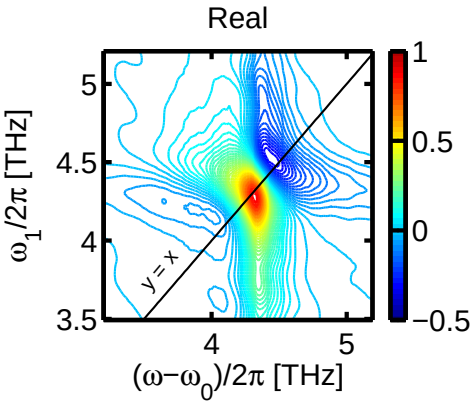

(a) Real part of S2 spectrum where field $\vec{E}_A$ arrives first.

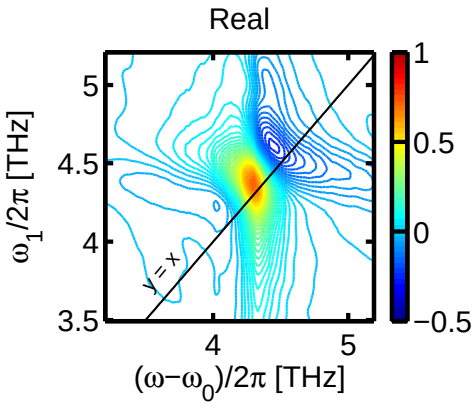

(b) Real part of S2 spectrum where field $\vec{E}_B$ arrives first.

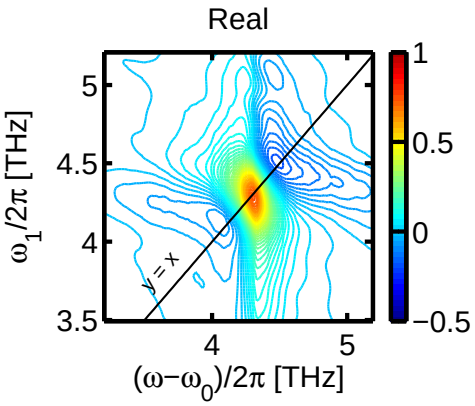

(c) Field $\vec{E}_B$ arrives first with corrected SLM calibration

Figure 5-17: The effect of an incorrect SLM pixel to frequency calibration on the complex 2D FTOPT spectra.

5.2.2 Two-quantum 2D FTOPT measurements

Here I will discuss the features in two-quantum 2D FTOPT spectra that indicate direct observation and separation of two-quantum coherences, which include biexciton-ground state coherences, and other higher-order correlated motions. The two-quantum signal contributions are excited by the first two fields, $\vec{E}_A$ and $\vec{E}_B$, which separately excite exciton coherences that oscillate with frequency ω_e and induce macroscopic linear polarization fields, $\vec{P}_A^{(1)}$ and $\vec{P}_B^{(1)}$, in the sample. If the excitation density is high enough, the "local" fields [95, 91] associated with exciton coherences can superpose with the excitation light fields to produce a nonlinear component to the net coherent response which is proportional to the product of the fields and which has wavevector $\vec{k}_A + \vec{k}_B$. Thus nearby exciton coherences can be correlated through the local field effects (LFE) of each one on the other.

Higher-order correlations also can result from direct interactions between nearby excitons, without mediation by a local field. As the electrons in nearby electron-hole pairs move away from their parent holes during their coherent oscillation cycles, the screening forces provided by the holes are diminished and the electron-electron repulsions are felt more strongly, leading to motions of the electrons away from each other. This occurs twice during each cycle of the exciton coherences, so, analogous to the nuclear spin case in 2D FTNMR spectroscopy described in Section 5.1, the interparticle forces and the particle responses to them oscillate at twice the exciton coherence frequency, $2\omega_e$. The holes also may move alternately farther from and closer to each other at frequency $2\omega_e$ as the screening between them provided by the electrons varies at that frequency. These exciton-exciton interactions give rise to measurable changes in the exciton energy (EIS) and dephasing rate (EID) and are not sensitive to the exciton spin [18] since the spin of electrons does not influence their electrostatic screening. As in the local field case, interactions between excitons that originated from the two different fields $\vec{E}_A$ and $\vec{E}_B$ give rise to two-quantum coherences a frequency $2\omega_e$ with the sum wavevector $\vec{k}_A + \vec{k}_B$. It has been shown that responses driven by EIS and local field effects are in phase with each other and 90°

out of phase with those driven by EID [87, 121].

Furthermore, as the exciton coherences oscillate, the holes may find new time-averaged locations, forming a bound, four-particle biexciton state whose binding energy is reflected directly in the biexciton coherence oscillation frequency, $\omega_b = 2\omega_e - \Delta/\hbar$. This occurs only between excitons of opposite spin as indicated in 5-3. Therefore, if $\vec{E}_A$ and $\vec{E}_B$ have opposite circular polarizations, biexciton coherences consisting of two HX or two LX excitons are excited, which we denote as HX_2 and LX_2, respectively. If the fields have the same circular polarization, then biexciton coherences of mixed character (MX_2) consisting of one HX and one LX exciton are excited. Unlike the LFE, EIS, and EID interactions (which I will collectively call "interaction-induced" effects), biexciton coherences are sensitive to exciton spin. In a two-quantum 2D FTOPT measurement, excitation fields $\vec{E}_A$ and $\vec{E}_B$ polarized perpendicular to the polarization of field $\vec{E}_C$ will only induce biexciton coherences that give rise to coherent scattering of probe light from $\vec{E}_C$ into the signal direction. Note that while exciton interaction mechanisms have been described here in largely phenomenological terms, four-particle correlations arise naturally in the equations of motion for excitonic wavepackets derived from a many-particle Hamiltonian [83].

Two-quantum measurements for different excitation polarization schemes

The 2D spectrum determined from the magnitude of the full signal field under cross-circular excitation is displayed in Fig. 5-18(a) with features denoted *a*–*e*. The positions of features along the two-quantum frequency coordinate, ω_2, and along the emission frequency coordinate, ω, allow us to assign their origins to different exciton interaction phenomena. Peak positions for some of the features labeled in Fig. 5-18, obtained by a least-squares multiple-Lorentzian fit, are listed in Table 5.2. Note that spectral interferometry detection gives the signal field as a function of the absolute emission frequency, ω, so I have subtracted the carrier frequency, ω_0, from the emission frequency so both coordinates are represented in the rotating frame. The most prominent features, *a* and *b*, centered slightly below the $y = 2x$ line belong to HX_2 coherences. Signal from all two-quantum biexciton coherences arises through emission

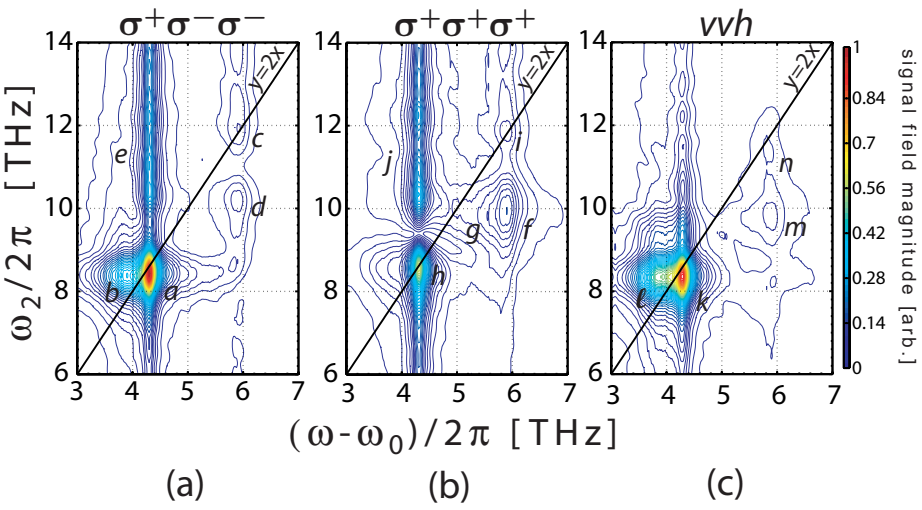

Figure 5-18: Spectral magnitudes of two-quantum 2D FTOPT measurements using (a) cross-circularly, (b) co-circularly, and (c) cross-linearly polarized excitation pulse sequences. The excitation pulse sequence is listed at the top of each spectral surface, so, for instance, in (a), field $\vec{E}_A$ was right-circularly polarized (σ^+), fields $\vec{E}_B$ and $\vec{E}_C$ were left-circularly polarized (σ^-), and field $\vec{E}_R$ was right-circularly polarized. The magnitudes are scaled to the maximum of (a) and the contour lines are spaced in intervals that are 2% of the maximum.

by one-quantum exciton coherences through two different pathways, illustrated by the double-sided Feynman diagrams shown in Fig. 5-19. The final field, $\vec{E}_C$, can either collapse the biexciton-ground state coherence to a radiative exciton coherence 5-19(a) or excite a new exciton coherence 5-19(b) such that the final macroscopic polarization evolves as a biexciton-exciton coherence whose emission is red-shifted along the ω coordinate (b). The LX_2 coherence, c, about ten times weaker than a because of the lower light-hole exciton absorption cross-section, is actually shifted above the $y = 2x$ line probably due to interference with another many-body contribution as discussed further below in connection with Fig. 5-18(c). The peak labeled d appears along ω_2 at the sum of the HX and LX emission frequencies. Since mixed biexcitons are not expected for cross-circular excitation, this feature results from an interaction-induced two-quantum coherence between HX and LX excitons. The vertical ridges, e, along the ω_2 coordinate are due to four-particle correlations, namely EID [88], between the excitons and free electron-hole pairs excited by the broadband pulses.

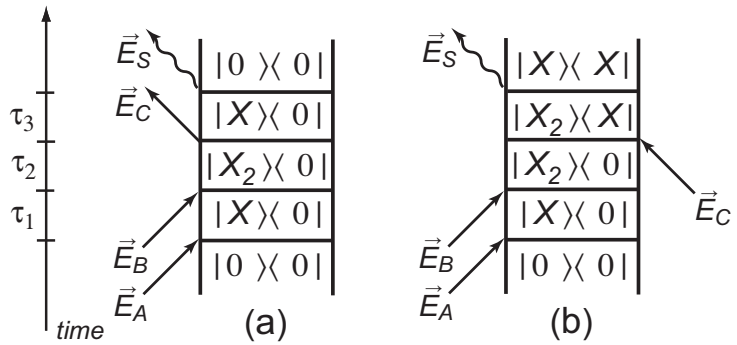

Figure 5-19: Feynman pathyways involving X_2 coherences during τ_2 that emit through (a) an exciton-ground state coherence or (b) a biexciton-exciton coherence.

Mixed biexciton coherences (MX_2) are observed in the 2D spectrum, shown in Fig. 5-18(b), obtained using co-circular excitation, with features denoted *f*–*j*. The feature belonging to the MX_2 coherence, *f*, appears along the ω_2 axis at a frequency slightly less than the sum of the HX and LX emission frequencies. It also exhibits a red-shifted shoulder, *g*, due to emission from an exciton-biexciton coherence. These features are directly analogous to *a* and *b*, respectively, for the HX_2 biexciton. The peaks labeled *h* and *i* are centered on the $y = 2x$ line and result from two HX and LX excitons, respectively, interacting through higher-order correlations. Again, vertical ridges, *j*, appear along ω_2 that arise due to exciton and free electron-hole pair interactions. The proportion of free carriers excited during the measurements can be adjusted by tuning the excitation fields away from the free-carrier absorption band. The effect of wavelength detuning of the excitation fields on the two-quantum 2D FTOPT measurements for co-circular and cross-circular polarizations is shown in Fig. 5-20. Specifically, the vertical feature, which is due to free-carrier absorption, is suppressed in 2D FTOPT spectra obtained with red-detuned (Fig. 5-20(b) and Fig. 5-20(d)) versus blue-detuned (Fig. 5-20(c) and Fig. 5-20(e)) excitation fields.

Excitation fields polarized perpendicularly to the probe field, $\vec{E}_C$, only induce two-quantum signals that arise from biexciton coherences. The 2D spectrum for perpendicular excitation is shown in Fig. 5-18(c) with features denoted *k*–*n*. The HX_2 peak, *k*, and its red-shifted shoulder, *l*, are analogous to *a* and *b* from the cross-

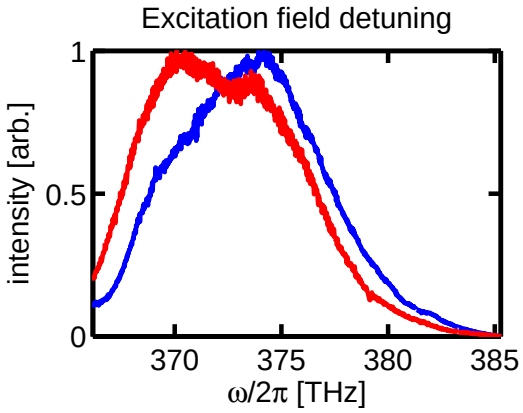

(a) Spectrum of excitation fields

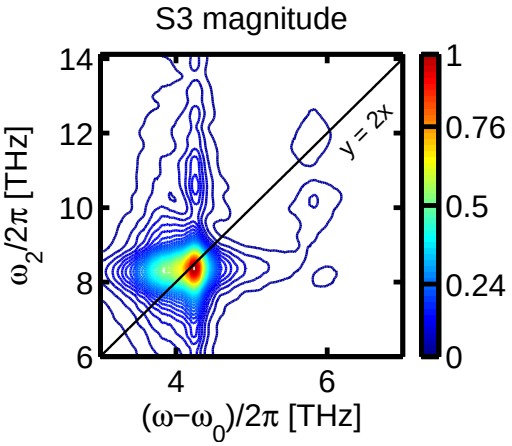

(b) Red-detuned cross-circularly polarized excitation fields

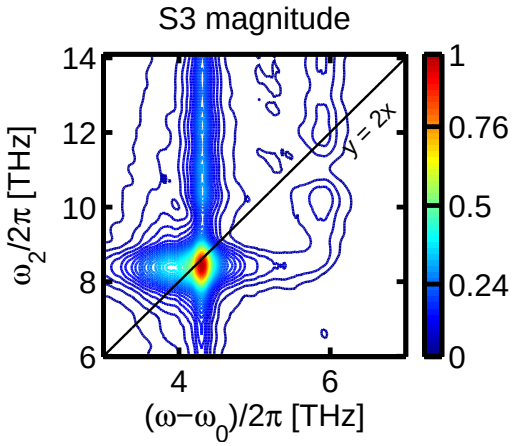

(c) Blue-detuned cross-circularly polarized excitation fields

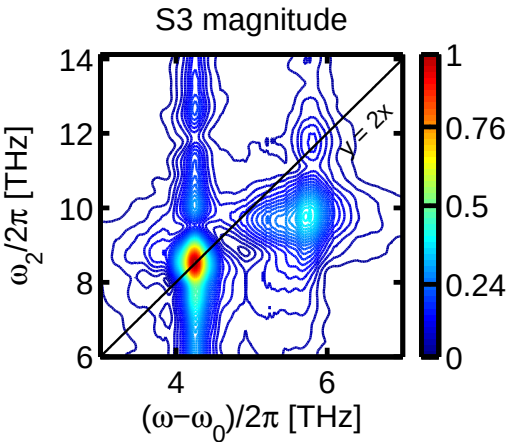

(d) Red-detuned co-circularly polarized excitation fields

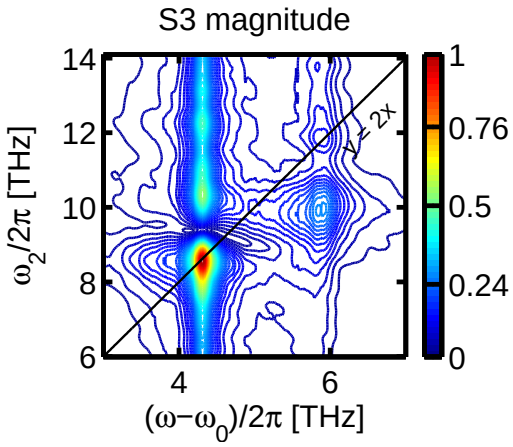

(e) Blue-detuned co-circularly polarized excitation fields

Figure 5-20: The effect of excitation wavelength detuning on two-quantum 2D FTOPT measurements. The amount of detuning is approximately 2 nm.

circularly polarized data in Fig. 5-18(a). The MX_2 peak, m, also appears to have a red-shifted feature but the signal level is too low for the shoulder peak value to be determined reliably. The LX_2 coherence, which results in the peak labeled n, is now shifted below the $y = 2x$ line as expected. The vertical ridges that were present in Fig. 5-18(a) and Fig. 5-18(b) are strongly suppressed here, confirming their origin from interaction-induced contributions, as discussed previously.

Biexciton binding energy

The peak positions, listed in Table 5.2, and linewidths were determined by fitting multiple Lorentzian functions to the projections along ω_2 and ω of the 2D spectral magnitudes displayed in Fig. 5-18. The spectral projections and their least-squares fits are displayed in Fig. 5-21(a) and Fig. 5-21(b). Two Lorentzian functional forms were used in fitting the projected magnitude. Equation 5.1 was used to fit the peaks projected to the ω_2 axis, while Eqn. 5.2 was used to fit the peaks projected to the emission axis, ω, The former multiple Lorentzian function includes a phase shift parameter which was necessary in order to properly fit the node present in the projected magnitude of the two-quantum 2D FTOPT measurement made with co-circularly polarized excitation fields.

$$L_1(\omega_2) = |\sum_n \frac{A_n}{\omega_{c,n}^2 - \omega_2^2 + i\Gamma_n} e^{i\phi_n}| \tag{5.1}$$

$$L_2(\omega) = \sum_n \frac{A_n(\frac{1}{2}\Gamma_n)^2}{(\omega - \omega_{c,n})^2 + \frac{1}{2}\Gamma_n} \tag{5.2}$$

The biexciton binding energies, Δ, were determined by subtracting the biexciton coherent oscillation frequency (center frequency in ω_2 from Fig. 5-21(a) and listed in Table 5.2) from the sum of its component exciton coherence frequencies obtained from separate one-quantum non-rephasing measurements (see Table 5.1). We calculated binding energies of 0.96±0.15 meV and 1.36±0.26 meV for the HX_2 and MX_2 biexcitons, respectively, using the peak positions of features a and f from the cross-circular

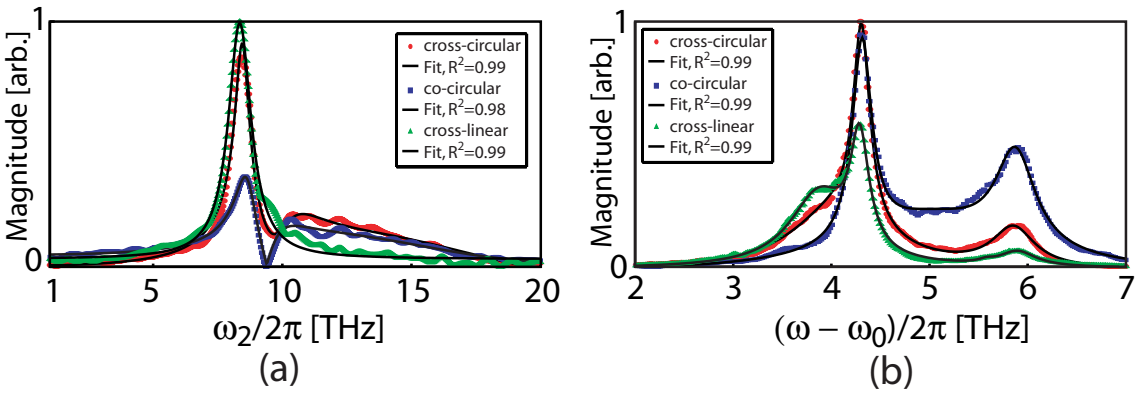

Figure 5-21: Biexciton or exciton-biexciton energetics and dephasing information was obtained by projecting the 2D spectral magnitudes obtained with different excitation polarization to the (a) ω_2 or (b) ω axis, respectively, and performing a nonlinear least-squares regression using a multiple Lorentzian fit to the spectral lineshape. The fitted center frequencies are given in 5.2. In (a) the 2D spectrum was only integrated over ω in a range around the HX emission frequency, while in (b) integration over the entire ω_2 dimension was performed.

and co-circular excitation measurement, respectively. The binding energies calculated from the peak positions from the perpendicularly-polarized excitation measurement for the HX_2 and MX_2 (peaks k and m) yield binding energies of 1.30±0.13 meV and 2.08±0.58 meV, respectively, which are slightly larger but just within experimental uncertainties of the other values. In both cases, the MX_2 biexciton binding energy is larger than the HX_2 binding energy, consistent with the expectation that the binding energy should increase with decreasing electron-hole effective mass ratio [122] since the LX has a larger effective mass in the unconfined dimension of the QW. The uncertainty in the fitted center frequency for the weak LX_2 peak was too large for the LX_2 binding energy to be determined.

A binding energy also may be extracted from the red-shifted biexciton-exciton emission shoulder, b, which may be compared to the exciton-ground state emission frequency ω_e. A value of 1.38±0.10 meV, similar to those reported earlier [123, 124, 125], was found from the cross-circular polarized data. This value, which might be labeled Δ_{b-e}, differs from the binding energy Δ=0.96 meV determined from the biexciton-ground state frequency of feature a. A simple definition of the binding energy is

Table 5.2: Frequency values in THz of peaks from Fig. 5-18 along the ω_2 and ω axes with uncertainties which are 95% confidence intervals from nonlinear regression to multiple-Lorentzian lineshapes. The user-defined carrier frequency, ω_0=368.00 THz, was subtracted from the fitted emission center frequency, ω.

Label	Two-quantum coherence frequency	One-quantum emission frequency
a) HX_2	8.45±0.02	4.31±0.00
b) HX_2–HX	8.45±0.02	3.97±0.02
c) LX_2	11.87±0.11	5.85±0.02
d) HX–LX	10.43±0.05	5.85±0.02
f) MX_2	9.97±0.04	5.87±0.01
g) MX_2–LX	9.97±0.04	5.47±0.21
h) HX–HX	8.63±0.04	4.31±0.00
i) LX–LX	11.68±0.12	5.87±0.01
k) HX_2	8.35±0.02	4.29±0.00
l) HX_2–HX	8.35±0.02	3.87±0.02
m) MX_2	9.79±0.12	5.90±0.05
n) LX_2	11.47±0.11	5.90±0.05

the energy difference between uncorrelated and correlated four-particle states, which corresponds to Δ. The value Δ_{b-e} is extracted from the biexciton-exciton transition, which is weighted by the transition dipole between subsets of biexciton and exciton configurations. As in the case of Δ, the value of Δ_{b-e} for HX_2 that is extracted from the perpendicularly polarized data in Fig. 5-18(c) is slightly larger, 1.71±0.08 meV, reflecting the very slight shift of both features k and l to slightly lower frequencies along the ω_2 axis than the analogous features a and b.

Real parts of the complex two-quantum 2D FTOPT spectra

The real parts of the 2D spectral magnitudes for the two-quantum measurements shown in Fig. 5-18 are displayed in Fig. 5-22. The nodes belonging to the two-quantum features are perpendicular to the $y = 2x$ line, consistent with a two-quantum non-rephasing interpretation of the measurements. The real part of the 2D spectrum for the cross-circular excitation case is shown in Fig. 5-22(a). The HX_2 peak, a, is largely positive which indicates that the final field, $\vec{E}_C$, stimulated emission from the biexciton to the exciton state. The red-shifted shoulder, b, which is due to an biexciton-exciton coherence that evolved during the emission time period, is largely

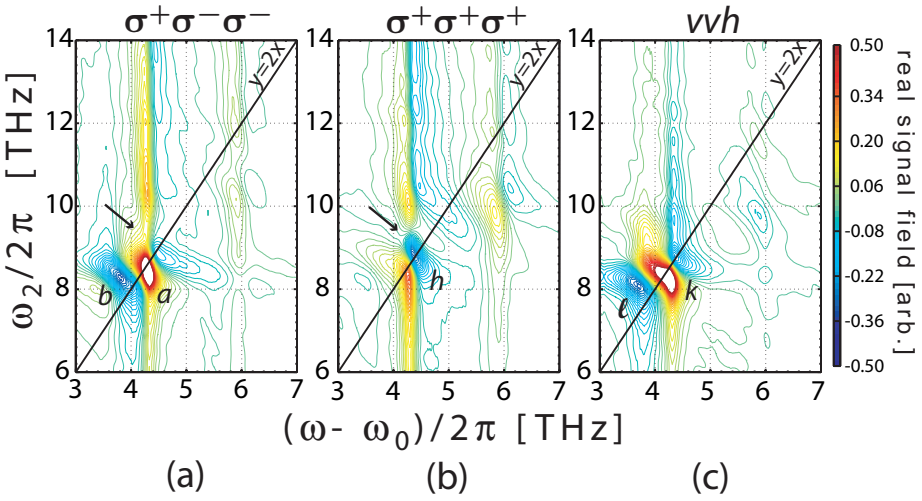

Figure 5-22: Real parts of the complex signal displayed in Fig. 5-18 for (a) cross-circularly, (b) co-circularly, and (c) perpendicularly polarized excitation pulse sequences. The arrows highlight (a) the absence of a phase shift between the HX_2 and vertically elongated features, or as in (b), the presence of a phase shift between the interaction-induced coherence peak and the vertically elongated feature. Since the vertically elongated feature was previously shown (see main text) to originate from EID contributions, the presence of a phase shift indicates that the interaction-induced peak is mainly due to EIS and local field effects.

negative which indicates absorption of a photon from the final field. The vertically elongated feature is in phase with the HX_2 peak. The real part of the 2D spectrum for the co-circular excitation case is shown in Fig. 5-22(b). Unlike the HX_2 peak, the interaction-induced coherence peak, h, is out of phase with the vertically elongated feature. The vertically elongated feature was previously explained to arise from interaction between an exciton and free electron-hole pair mediated by EID [88]. Since EID and EIS/local field interactions were found to be 90° out of phase, as discussed above, we can conclude that the interaction-induced coherence peak largely results from an EIS/local field interaction between excitons. In fact, EIS and local field contributions should still be present in the measurements using cross-circular excitation which may explain the change in the lineshapes of a and b when compared to the lineshapes of k and l in the perpendicularly polarized excitation measurement, shown in Fig. 5-22(c), where contributions from interaction-induced many-body effects are largely suppressed.

Phenomenological modeling of EIS and EID contributions to the two-quantum 2D FTOPT spectrum of a two-level system (which represents interactions in an ensemble of exciton states where biexciton contributions are neglected) can reveal the origin of the interaction-induced coherence peak for the co-circular excitation case. The measured real spectral surface for peak h from Fig. 5-22 is presented in Fig. 5-23 alongside the results obtained with the MOBE model for a two-level system which represents exciton-ground state coherences only. The predominantly dispersive lineshape in the measured 2D spectrum is comparable to the MOBE results where only EIS or local field effect contributions were included.

Biexciton dephasing time and carrier density dependence

The HX_2 and MX_2 dephasing times were determined from fits of the Lorentzian linewidths of the 2D spectral magnitudes projected to the ω_2 axis for the peaks a and f of Fig. 5-18, respectively, yielding values of 1.84±0.12 ps and 0.91±0.05 ps, respectively. The dephasing times also may be determined from the time-dependent transients as shown for HX_2 in Fig. 5-24.

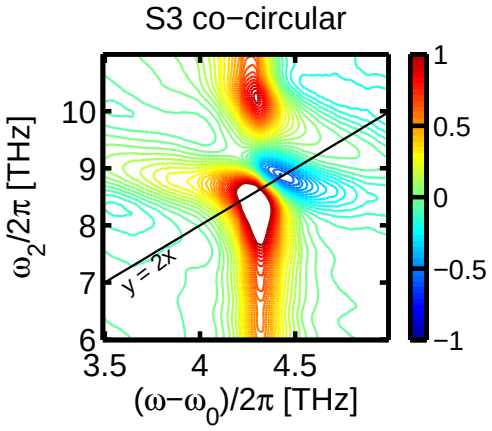

(a) Real part of the measured S3 spectrum using co-circular excitation

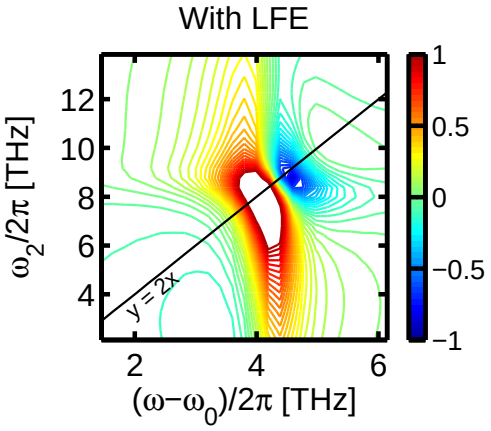

(b) Calculated using the optical Bloch equations with local field effects ($N_d = 10^{10}$ carriers/cm^2/well)

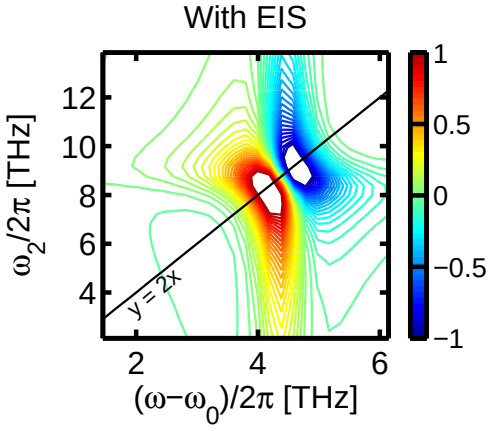

(c) With excitation-induced shift (ω'=25 THz/m^3)

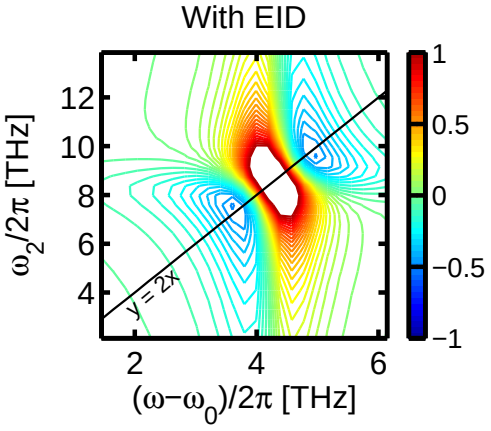

(d) With excitation-induced dephasing (γ'=25 THz/m^3)

Figure 5-23: Real part of the two-quantum 2D FTOPT spectrum of GaAs quantum wells using co-circularly polarized excitation fields compared to results from the modified optical Bloch equations.

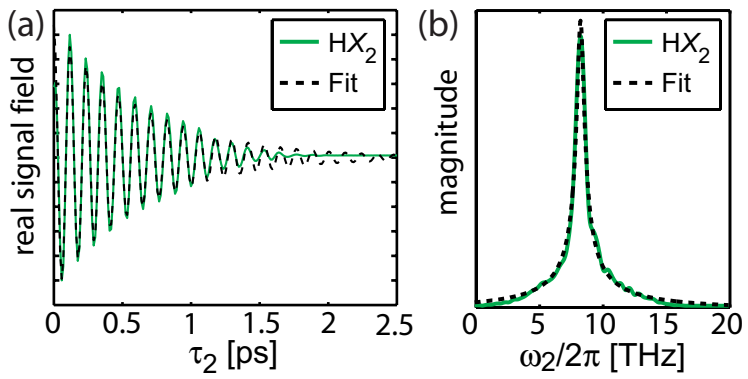

Figure 5-24: (a) HX_2 transient vs. τ_2 extracted from the two-quantum 2D FTOPT measurement shown in Fig. 5-18(c) where fields $\vec{E}_A$ and $\vec{E}_B$ excited the sample time-coincidentally (i.e. τ_1=0) and were linearly polarized perpendicular to the final field, $\vec{E}_C$. As before, the oscillations are shifted into the rotating frame. (b) Fourier transform of the transient shown in (A) to the ω_2 frequency domain. The fitted functions in the time and frequency domains (dotted lines) had a center frequency, ω_{HX_2}, of 8.35±0.01 THz and a dephasing time, Γ_{HX_2}, of 1.86±0.08 ps.

The coherently generated carrier density was varied by changing the average power of the excitation fields. In this series of measurements the center wavelength of the excitation fields was tuned away from the free-carrier absorption band as shown for the 2D FTOPT spectra in Fig. 5-20(a). Figure 5-25 shows a previously undiscovered dependence of the biexciton dephasing time on the excitation density. Both the HX_2 and MX_2 biexciton dephasing times decreased as the power was increased, revealing excitation-induced biexciton dephasing which results from six-particle (exciton-biexciton) interactions. Biexciton-free carrier interactions are less likely because the laser wavelength is red-detuned from the free-carrier absorption band. Furthermore, the moderate excitation density limits still higher-order biexciton-biexciton interactions. Six-particle correlations have been observed in previous nonlinear spectroscopy measurements [126], but only in a highly convolved manner without isolation of their distinct effects. The biexciton binding energy was found to be essentially independent of excitation density in the present study. Note that the HX_2 and MX_2 biexciton dephasing times obtained from measurements using cross-linearly polarized excitation fields followed the same trend as the dephasing times obtained from measurements

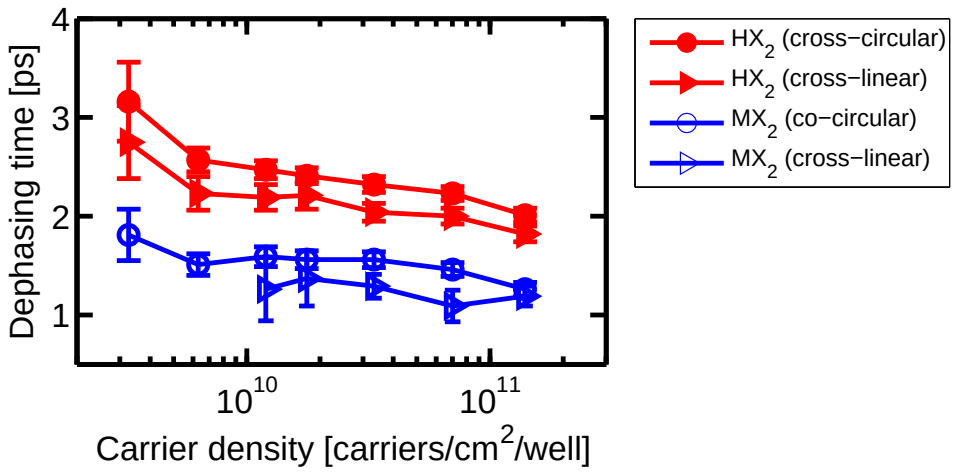

Figure 5-25: Carrier density dependence of the HX_2 and MX_2 biexciton dephasing times for circularly and cross-linearly polarized excitation fields.

using circularly polarized excitation, because the interactions that cause the phenomena still occur in the sample, even though the experiment does not probe their coherent contributions to the signals, as in the case of cross-linear excitation. In general, the MX_2 mixed biexciton coherence dephases faster than the HX_2 biexciton coherence. This is likely due to the influence of the LX exciton which has a faster dephasing time than the HX exciton. Furthermore, the dephasing time extracted for the mixed biexciton from the blue-detuned two-quantum 2D FTOPT measurements found in Fig. 5-18 is smaller than the dephasing time extracted from the red-detuned measurements, i.e. 0.91 ps versus 1.81 to 1.26 ps.

The dephasing time of the two-quantum signal at $2\omega_e$ may also be extracted from a fit of the signal magnitude projected to the ω_2 using Eqn. 5.2. The fit results are plotted with respect to the carrier density in Fig. 5-26. Note that the dephasing time extracted for the higher-order correlations that contribute to the signal at $2\omega_e$ seem to follow a trend opposite of the biexciton dephasing. However, more measurements are required before making any conclusions since the uncertainty in the fitted linewidth is quite large compared to the total range of dephasing values. This supposed trend may simply be due to the fact that signal contributions from many-body phenomena depend on the excited state population, as discussed in Chapter 4. Also note that

the HX_2 and "many-body effect" dephasing times cross at a certain carrier density, however the location of this feature of the data was not reproducible.

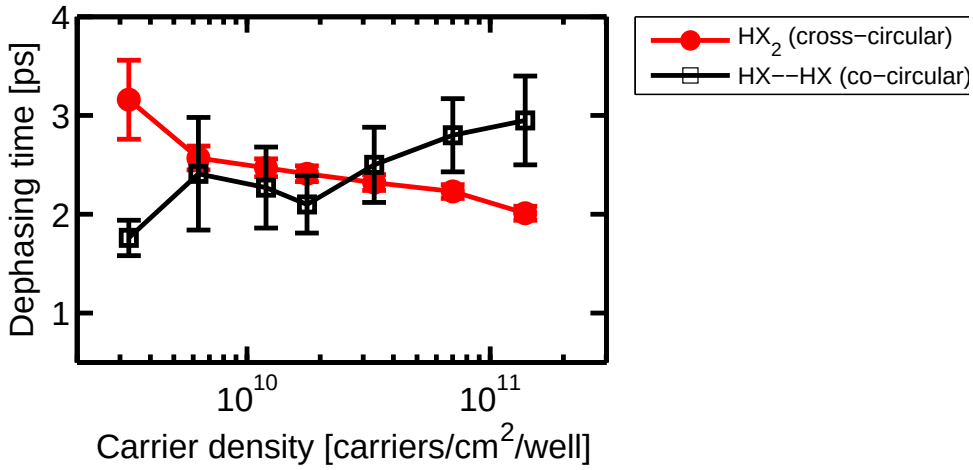

Figure 5-26: Carrier density dependence of the HX_2 biexciton dephasing time compared to the dephasing time of the higher-order correlation that contributes to the two-quantum 2D FTOPT signal at $2\omega_e$.

5.3 Conclusions

The one-quantum and two-quantum 2D FTOPT measurements presented here represent a decisive step in the isolation and elaboration of many-body interactions in the prototype GaAs system that cannot be treated using a mean-field approximation. The present results demonstrate the unique capabilities of fully coherent multidimensional optical spectroscopy for accessing "dark" states using multiple-photon transitions and the simplicity of the spatiotemporal pulse shaping approach for execution of otherwise daunting measurements. The same apparatus and measurements can be used for feedback-directed quantum control over the coherences.

Chapter 6

Local field effects in dense rubidium vapor

6.1 Introduction

Typical treatment of the linear and nonlinear electronic susceptibilities of a material assumes that the electromagnetic field interacting with a single resonant atom or molecule is equivalent to the macroscopic field, $\vec{E}$, that appears in Maxwell's equations. However, a general treatment requires that the field experienced by each atom or molecule, also known as the Lorentz local field, $\vec{E}_L$ [96], must be considered in order to describe fully the electronic susceptibility of the material. For a first-order interaction, the Lorentz local field induces a *microscopic* polarization field, $\vec{p}$, equal to the linear polarizability of the atom, α, such that

$$\vec{p} = \alpha \vec{E}_L. \tag{6.1}$$

The Lorentz local field incorporates the first-order polarization in the dielectric medium surrounding a single atom induced by the macroscopic field, $\vec{E}$, such that

$$\vec{E}_L = \vec{E} + \frac{4\pi}{3}\vec{P} \tag{6.2}$$

where $\vec{P} = N\vec{p}$. Thus, the electronic susceptibility of a material is modified due to local field effects when the number density of atoms becomes sufficiently large ($> 10^{22}$ atoms/m^3). The change in the linear susceptibility can be derived by combining Eqn. 6.1 and Eqn. 6.2, such that

$$\begin{aligned} \vec{P} &= N\vec{p} \\ &= N\alpha\vec{E}_L \\ &= N\alpha(\vec{E} + \frac{4\pi}{3}\vec{P}) \end{aligned} \tag{6.3}$$

Equation 6.3 can be simplified for the linear susceptibility, $\chi^{(1)}$, using the definition $\vec{P} \equiv \chi^{(1)}\vec{E}$. The result (see Eqn. 6.4) shows that local field effects increase the linear susceptibility nonlinearly with respect to N beyond its predicted value of $N\alpha$

$$\chi^{(1)} = \frac{N\alpha}{1 - \frac{4\pi}{3}N\alpha} \tag{6.4}$$

Similar relations can be derived for the dependence of the nonlinear electronic susceptibility [95] on local field effects, which can explain the enhancement of the nonlinear optical coefficients of nanocomposite materials [127]. Local field effects, sometimes referred to as near dipole-dipole interactions, have implications for quantum control of semiconductor quantum dots [128]. At even higher densities, the Lorentz local field can shift the resonance frequency, related to the Lorentz-Lorenz energy shift, and dephasing rate, as evidenced by transient four-wave mixing experiments [98].

In this chapter, I will present one-quantum and two-quantum 2D FTOPT measurements on a dense rubidium vapor. The two-quantum spectra exhibit features whose frequency position, at twice the optical resonance along the ω_2 coordinate, and complex 2D lineshapes indicate contributions from local field effects, which were modeled using the modified optical Bloch equations in Section 4.3. These measurements are distinct from previous two-dimensional spectra of rubidium vapor measured using a purely frequency domain technique based on spatiotemporal pulse shaping [43]

that could not provide the full complex signal field. Such frequency domain measurements would not resolve signal contributions due to local field effects which requires a specific time-ordering of the excitation fields (i.e. the two-quantum 2D FTOPT pulse sequence) and detection of the full signal field. Local field contributions should manifest in the the two-quantum 2D FTOPT spectrum of any dense system of oscillators, such as semiconductors excitons. Therefore, 2D FTOPT measurements made for a simpler system such as rubidium vapor can help to clarify the interpretation of spectral contributions due to such effects.

6.2 Experiment

Atomic rubidium vapor has four electronic transitions accessible by ultrafast Ti:Sapphire pulses, which are shown in Fig. 6-1(a). In the experiments presented here, the spectra of the broadband excitation fields, shown in Fig. 6-1(b), were resonant with the D1 (at 377.11 THz) and D2 (at 384.23 THz) transitions of rubidium only, as evidenced by the spectrum of 2D FTOPT signal taken with the reference field blocked, also shown in Fig. 6-1(b). The commercially available (Triad Technology Inc.) rubidium sample cell consisted of a 5 mm path length quartz cell which contained 650 mTorr of helium buffer gas in addition to a small amount of rubidium. The vapor pressure of rubidium [129] was used to determine the number density of atoms, N, in the sample for a given temperature. The relation between sample temperature and N determined for the sample cell is shown in Fig. 6-1(b). In the present measurement, the sample temperature was maintained at approximately 110^oC, therefore N was approximately 10^{19} atoms/m^3

The excitation fields $\vec{E}_A$, $\vec{E}_B$ and $\vec{E}_C$ used to excite the one-quantum and two-quantum 2D FTOPT signal fields, $\vec{E}_S$, were provided by an unamplified Ti:sapphire laser with a pulse repetition rate of 92.5 MHz and a pulse width of 65 fs. The average power in each of the four beams produced by the multidimensional optical spectrometer apparatus described in Section 3.2 was 10 mW. The pulse sequences used to measure exciton coupling and interaction in GaAs quantum wells, presented

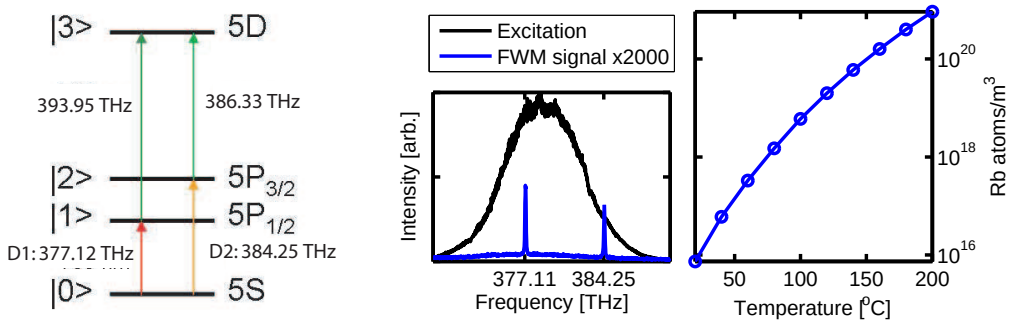

(a) Energy level diagram for Rb (b) Excitation/signal spectra and the number density of Rb atoms vs. sample temperature

Figure 6-1: Experimental parameters relevant to 2D FTOPT measurements of Rb vapor

in Section 5.2, were used here as well to excite and probe coupled optical resonances and two-quantum signal contributions originating from local field effects in Rb vapor. Similar to the measurements made on semiconductor quantum wells in Chapter 5, the reference field, $\vec{E}_R$, propagated through the sample 1.00 ps before emission of the signal, with power reduced by a factor of 1000 compared to the power of the excitation beams.

The carrier frequency of the excitation fields was defined as 373.00 THz. Therefore, the one-quantum signals for the D1 and D2 transitions will appear at frequencies of approximately 4.11 and 11.22 THz along the ω_1 coordinate, while two-quantum signals will be present at sums of the atomic resonances along the ω_2 coordinate, i.e. 8.22, 15.33 and 22.44 THz. Interferometric detection of the signal field by superposition of its spectrum with the spectrum of the temporally delayed reference field gave the signal field as a function of the absolute emission frequency, ω, so I have subtracted the carrier frequency, ω_0, from the emission frequency so both coordinates of the 2D FTOPT spectra are represented in the rotating frame. The overall phase shift parameter, determined using the same technique described by Fig. 5-8, was $-2\pi \times 0.4$ and the entire data set was multiplied by this factor after the measurement. Contour lines in all of the 2D spectra presented here are drawn at intervals of 10% of the maximum amplitude.

6.3 Results and Discussion

6.3.1 One-quantum 2D FTOPT measurements

The four main spectral features found in the one-quantum 2D spectra can be described by the sixteen double-sided Feynman diagrams shown in Fig. 6-6 located at the end of this chapter. Two of the spectral features are located on the $y = x$ diagonal and the other two, referred to as cross peaks, are located off the diagonal. The Feynman pathways contributing to the cross peaks are numbered 7, 8, 11, 12, 15, and 16. Diagrams 11 and 12 contribute to the non-rephasing 2D spectra, while diagrams 7, 8, 15 and 16 contribute signals to the rephasing 2D spectra. All the other numbered diagrams contribute to one of the two diagonal peaks.

(I) Rephasing (S1)

Figure 6-2(a) shows the rephasing (S1) 2D spectra obtained for a dense Rb vapor. The peaks on the diagonal are the D1 and D2 resonances of Rb while the cross peaks indicate that the D1 and D2 resonances are coupled. Each of the spectral features, labeled in Fig. 6-2(b), results from signal contributions that are described by two of the Feynman pathways in Fig. 6-6. The ratio of the peak magnitudes (A:B:C:D) in the rephasing 2D spectrum is 2.1 : 1.4 : 2.1 : 1.0. This is consistent with the signal magnitude given for each of the Feynman pathways, which predicts the ratio of peak magnitudes as 2 : 1 : 2 : 1. Note that this calculation takes into account that the excitation spectrum has twice the magnitude at the D1 transition than the D2 transition, as shown in Fig. 6-1(b). Also note that the D2 transition has a larger dipole moment, such that $\mu_{D2} = \sqrt{2}\mu_{D1}$. The fitted center frequencies for the 2D spectral features projected to the ω_1 and ω axes are given in Table 6.1.

Figure 6-2(c) details the D1 resonance (peak A) from the rephasing 2D spectra. The real part of the 2D spectrum is largely positive and has a primarily absorptive lineshape, which is consistent with the calculated rephasing 2D spectra obtained using the optical Bloch equations presented in Chapter 4, and indicates stimulated emission from the sample. The lineshape remains primarily absorptive since contributions from

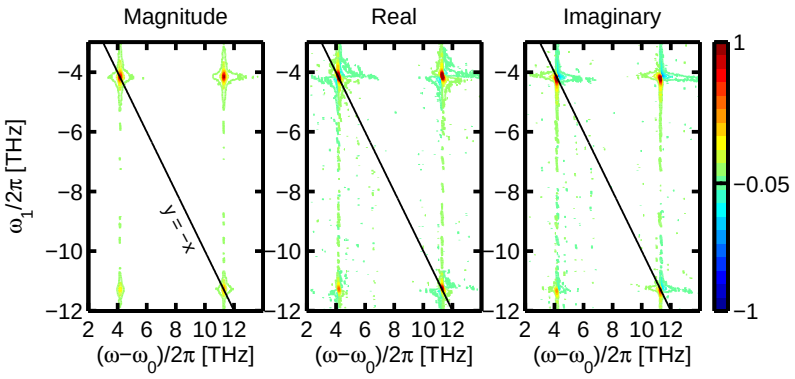

(a) Rephasing 2D spectra including both the D1 and D2 transitions

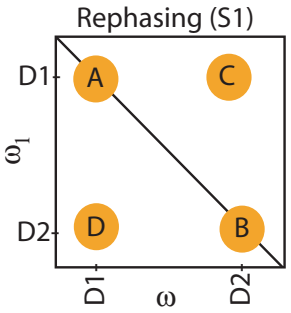

(b) Diagonal (A and B) and cross (C and D) peaks

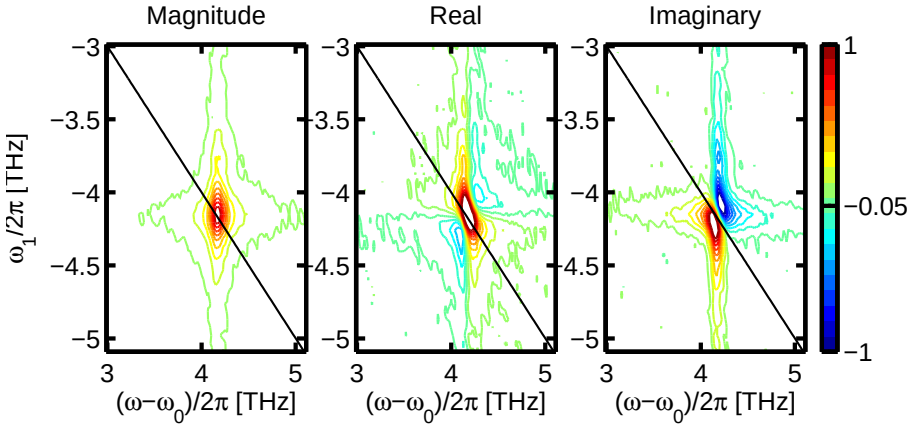

(c) Complex 2D FTOPT spectra for the D1 transition only.

Figure 6-2: Rephasing 2D FTOPT spectral magnitude (left), real (middle) and imaginary (right) surfaces for Rb vapor. The Feynman pathways for each peak are as follows: A: $R_2(5) + R_3(13)$, B: $R_2(6) + R_3(14)$, C: $R_2(8) + R_3(16)$, D: $R_2(7) + R_3(15)$.

local field effects are not very significant at this density and the many-body effect is largely convolved with the one-quantum coherences in this measurement.

(II) Non-rephasing (S2)

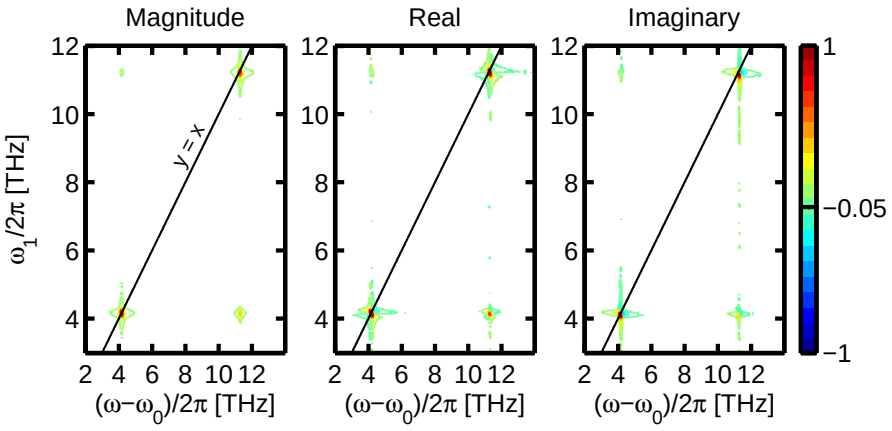

(a) Non-rephasing 2D spectra (field $\vec{E}_A$ interacts first)

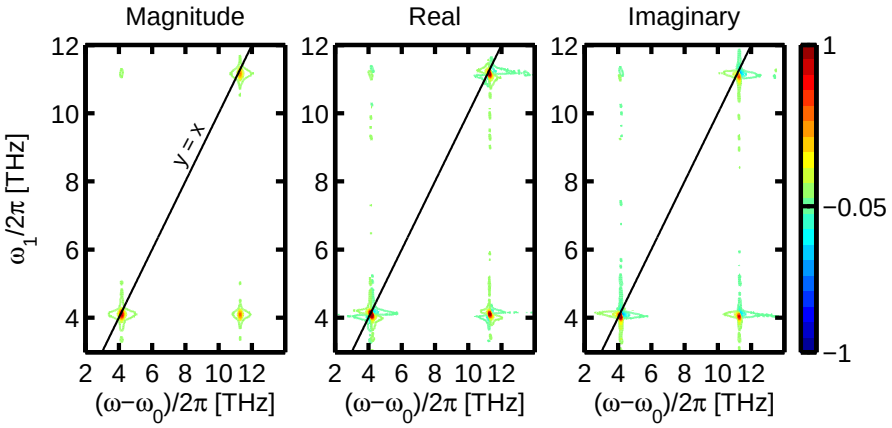

(b) Non-rephasing 2D spectra (field $\vec{E}_B$ interacts first)

Figure 6-3: Non-rephasing 2D FTOPT spectral magnitude (left), real (middle) and imaginary (right) surfaces for Rb vapor including both the D1 and D2 transitions. The Feynman pathways for each peak are as follows: A: $R_4(9) + R_1(3) + R_1(1)$, B: $R_4(10) + R_1(4) + R_1(2)$, C: $R_4(12)$, D: $R_4(11)$.

Figure 6-3 shows the non-rephasing (S2) 2D spectra obtained for a dense Rb vapor where either of two different excitation fields, $\vec{E}_A$ and $\vec{E}_B$, arrived at the sample first to excite the D1 and D2 resonances of Rb. In this measurement, three Feynman pathways describe the signal contributions for the diagonal peaks, while only one pathway describes each off-diagonal peak, which explains why the cross peaks are very

weak compared to the diagonal peaks. The ratio of the peak magnitudes (A:B:C:D) in the non-rephasing 2D spectrum for $\vec{E}_A$ excitation shown in 6-3(a) is 4.2 : 3.8 : 1.9 : 1.0. Similarly, for the 2D spectrum in Fig 6-3(b) where $\vec{E}_B$ served as the first excitation field, the ratio of peak magnitudes is 4.5 : 3.8 : 3.0 : 1.0. Note that the predicted ratio of peak magnitudes is 5 : 4 : 2 : 1 for an excitation spectrum centered on the D1 transition. The fitted center frequencies for the 2D spectral features projected to the ω_1 and ω axes are given in Table 6.1.

Figure 6-4 details the D1 resonance peak from the non-rephasing 2D spectra using different excitation fields. The two spectral surfaces obtained using the two different excitation fields $\vec{E}_A$ and $\vec{E}_B$ as the first field interaction should be identical, since both fields contribute their positive wavevector component to the signal. However, a small difference in positions of peaks along the ω_1 coordinate can occur if the grating-lens dispersion in the spatiotemporal pulse shaper is slightly different along different vertical regions of the 2D SLM where the phase profiles of the excitation fields are specified. This shift in the peak position is depicted in the 2D magnitude spectrum of Fig. 6-4 and in the fitted center frequencies along the ω_1 axis for these spectral surfaces are 4.15 THz and 4.09 THz. Unlike for the GaAs quantum well non-rephasing measurements, I will not correct the SLM pixel-to-frequency calibration in order to demonstrate similar effects in the two-quantum 2D spectra.

Similar to the S1 measurement presented above, the real parts of the 2D spectra are largely positive and have a primarily absorptive lineshape. The 2D spectral lineshapes in Fig. 6-4(a) and Fig. 6-4(b) are nearly identical, with the only difference being that the peak in Fig. 6-4(b) is slightly red-shifted along the ω_1 coordinate. This confirms that slight distortions in the SLM pixel-to-frequency calibration only change the positions of peaks and not their complex 2D lineshapes.

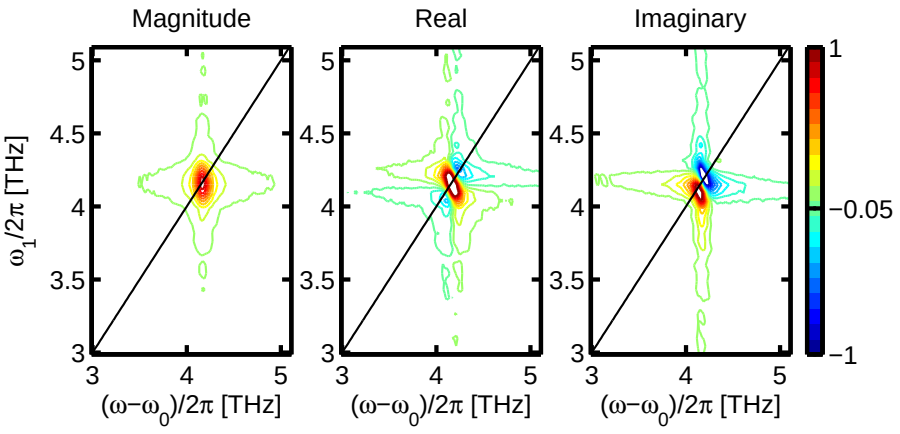

(a) 2D spectra for the D1 transition only (field $\vec{E}_A$ interacts first)

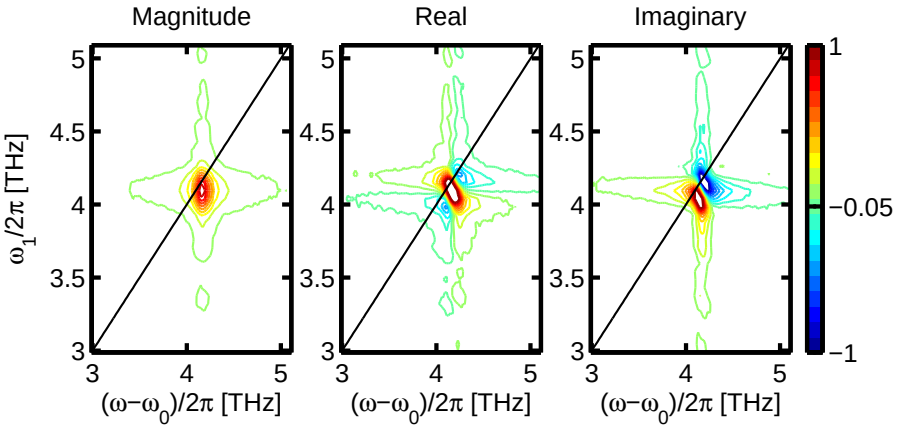

(b) 2D spectra for the D1 transition only (field $\vec{E}_B$ interacts first)

Figure 6-4: Non-rephasing 2D FTOPT spectral magnitude (left), real (middle) and imaginary (right) surfaces for Rb vapor for the D1 transition only.

Table 6.1: Fitted center frequency for peaks in the 2D FTOPT spectra projected to the ω_1 and ω coordinates shown in Fig. 6-2, Fig. 6-3 and Fig. 6-5. The peaks were fitted to multiple-Lorentzian lineshapes using nonlinear regression. The uncertainties reported represent the 95% confidence interval for the fitted parameters.

Peak	ω_1/ω_2 position	ω position
Rephasing (S1)		
D1	4.14±0.02	377.18±0.01
D2	11.27±0.03	384.29±0.01
Non-rephasing (S2) with $\vec{E}_A$ excitation		
D1	4.15±0.01	377.17±0.01
D2	11.22±0.01	384.29±0.01
Non-rephasing (S2) with $\vec{E}_B$ excitation		
D1	4.09±0.01	377.17±0.01
D2	11.17±0.01	384.29±0.01
Two-quantum (S3)		
D1+D1	8.23±0.04	377.18±0.01
D2+D2	22.40±0.05	384.29±0.01
D1+D2	15.31±0.02	384.29±0.01

6.3.2 Two-quantum 2D FTOPT measurements

Figure 6-5 shows the two-quantum 2D spectra measured for dense rubidium vapor. Recall that for this measurement, the interpulse delay, τ_2, is scanned by delaying fields $\vec{E}_A$ and $\vec{E}_B$ together. No one-quantum signal for this time-ordering of the excitation fields is expected given the three-level 'V' energy level diagram for the D1 and D2 transitions of rubidium. However, local field effects can drive new signal contributions, which were shown to contribute new spectral features at twice the one-quantum coherent oscillation frequency using the modified optical Bloch equations presented in Section 4.3.1. The fitted center frequencies along the ω_2 axis of the peaks in Fig. 6-5(a), also given in Table 6.1, are 8.23, 15.31, and 22.40 THz and correspond to sums of the one-quantum coherence frequencies measured using the non-rephasing pulse sequence where field $\vec{E}_A$ or $\vec{E}_B$ was first to excite the sample. The ratio of the peak magnitudes, which are labeled A, B, C, D as shown in Fig. 6-5(b), is 2.6 : 1.7 : 1.0 : 2.9. The ratio of peak magnitudes given by the Feynman diagrams for a cascaded five-level system (not shown) is 2 : 1 : 1: 2, which is in close agreement to

the measured ratio. Figure 6-5(c) shows in detail peak A from the two-quantum 2D spectra. The real part of the complex 2D lineshape is largely absorptive and positive, which is consistent with the calculated two-quantum 2D spectra using the modified optical Bloch equations for a low density of atoms, i.e. $< 10^{23}$ atoms/m^3. See Section 4.3.1.

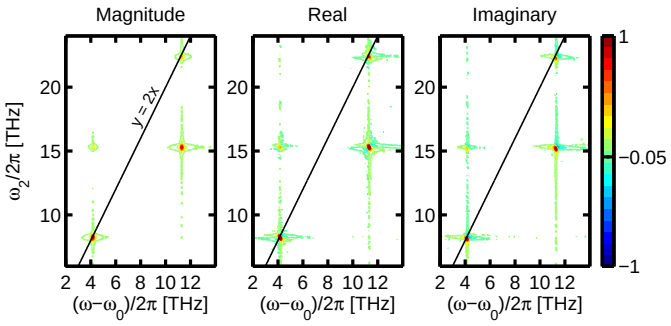

(a) 2D spectra for the D1 and D2 transitions

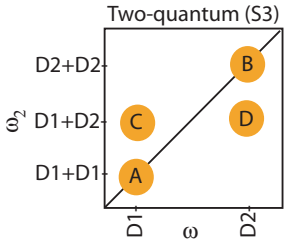

(b) S3 map

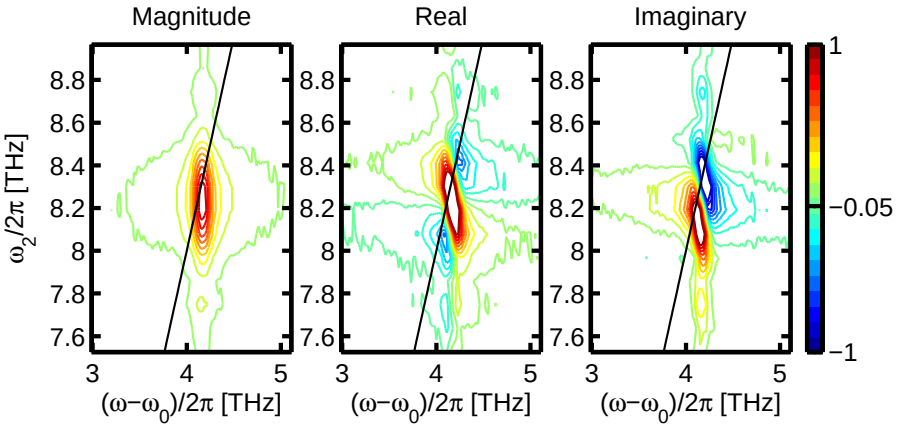

(c) 2D spectra for the D1 transition only

Figure 6-5: Two-quantum 2D-FTOPT spectral magnitude (left), real (middle) and imaginary (right) surfaces for Rb vapor.

6.4 Conclusions

The one-quantum and two-quantum 2D FTOPT measurements on dense Rb vapor presented here serve as a useful contrast to similar measurements on GaAs quantum wells. Correlations between excitations in Rb are mediated by local fields, which can

be treated in a mean-field approximation, whereas the correlations among excitons in semiconductors due to Coulomb interactions and biexcitons cannot. The number density of Rb atoms in these experiments is quite low, and in fact, it is so low that no qualitative change in the lineshape is observed in the one-quantum measurements since the signal contributions from local field effects are convolved with the stronger D1 and D2 resonances. In contrast, two-quantum signal contributions from local field effects have been discriminated from one-quantum signals using the two-quantum 2D FTOPT measurements, such that the origins of the signals are easy to discern. Lastly, two-quantum measurements on a simple system about which much is known, like Rb vapor, are useful for understanding the types of distortions which may be present in the optical setup.

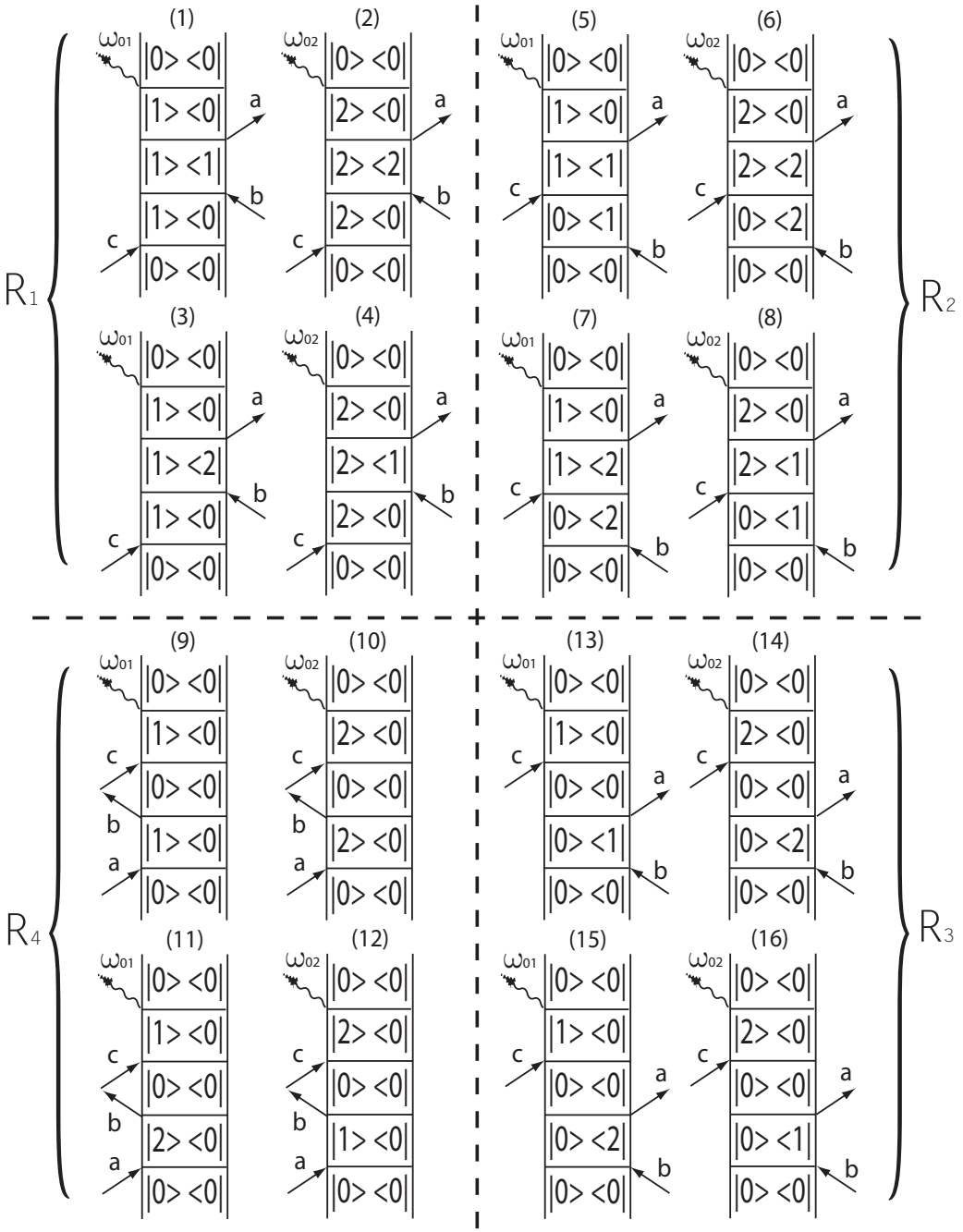

Figure 6-6: Double-sided Feynman diagrams for a three-level ('V') system. Diagrams on the right, labeled R_2 and R_3 depict rephasing pathways. Non-rephasing pathways are labeled R_1 and R_4.

Chapter 7

Outlook

The one-quantum and two-quantum 2D-FTOPT measurements presented here permit isolation and elaboration of many-body interactions in the prototype GaAs system that cannot be treated using a mean-field approximation. The robustness of the spatiotemporal pulse shaping approach simplifies and enhances the execution of the otherwise daunting 2D FTOPT measurements, which are amenable to the study of exciton coupling and interactions in a variety of nanomaterials. Of particular interest would be higher-order correlations whose signal contributions may be isolated from the two-particle correlations typically probed by one-quantum techniques using the two-quantum 2D FTOPT techniques presented here. For example, in quantum dots, observation of multiple-quantum coherences and populations from biexcitons and higher-lying states will have additional importance in laser gain, solar energy conversion, and other applications. Two-quantum 2D FTOPT experiments of photosynthetic complexes can provide knowledge about energy dissipation from multiple electronic excitations that serve as protective channels for excess energy discharge. Also of interest would be exciton and biexciton correlations in J-aggregates where 2D FTOPT could reveal how electronic energy is transferred between different strata of a organic photovoltaic cell. Three-dimensional FTOPT spectroscopic measurements are also possible, which can discern more of the Feynman pathways contributing to the signal.

The multiple fully coherent pulses generated using the spatiotemporal pulse shap-

ing techniques elaborated here can be extended to a variety of spectroscopic measurements. Higher-order spectroscopy techniques, which demonstrate the excitation of six-particle correlations through a $\chi^{(5)}$ process, may benefit from the capabilities of spatial and temporal shaping of ultrafast laser pulses and inherent phase stability of the method. Furthermore, the phase coherent pulse pairs generated by the spatiotemporal pulse shaping technique may be adapted to wave-packet interferometry experiments, which aim to map out the excited state potential energy surfaces of small molecules [130]. Spatiotemporal pulse shaping can also provide non-collinearly propagating, multiple pulse probes for a THz-pump/optical-probe experiment on semiconductor QWs, where the strong THz field can accelerate the excited carriers. The future is bright for coherently controlled ultrafast spectroscopy.

Bibliography

[1] G. D. Scholes and G. Rumbles. Excitons in nanoscale systems. *Nature Materials*, 5:683, 2006.

[2] D. Snoke, S. Denev, Y. Liu, L. Pfeiffer, and K. West. Long-range transport in excitonic dark states in coupled quantum wells. *Nature*, 418:754, 2002.

[3] S. Utsunomiya, L. Tian, G. Roumpos, C. W. Lai, N. Kumada, T. Fujisawa, M. Kuwata-Gonokami, A. Loffler, S. Hofling, A. Forchel, and Y. Yamamoto. Observation of bogoliubov excitations in exciton-polariton condensates. *Nature Physics*, 4:700, 2008.

[4] Wang Yao, Ren-Bao Liu, and L. J. Sham. Optically manipulating spins in semiconductor quantum dots. *Journal of Applied Physics*, 101:081721, 2007.

[5] Xiaodong Xu, Bo Sun, Paul R. Berman, Duncan G. Steel, Allan S. Bracker, Dan Gammon, and L. J. Sham. Coherent optical spectroscopy of a strongly driven quantum dot. *Science*, 317:929, 2007.

[6] Jonathan R. Tischler, M. Scott Bradley, and Vladimir Bulovic. Strong coupling in a microcavity led. *Physical Review Letters*, 95:036401, 2005.

[7] Seth Coe, Wing-Keung Woo, Moungi Bawendi, and Vladimir Bulovic. Electroluminescence from single monolayers of nanocrystals in molecular organic devices. *Nature*, 420:800, 2005.

[8] Jagdeep Shah. *Ultrafast Spectroscopy of Semiconductors and Semiconductor Nanostructures*. Springer, Berlin, 1999.

[9] Gregory S. Engel, T. R. Calhoun, Elizabeth L. Read, Tae-Kyu Ahn, Tomas Mancal, Yuan-Chung Cheng, Robert E. Blankenship, and Graham R. Fleming. Evidence for wavelike energy transfer through quantum coherence in photosynthetic systems. *Nature*, 446:782, 2007.

[10] Hohjai Lee, Yuan-Chung Cheng, and Graham R. Fleming. Coherence dynamics in photosynthesis: Protein protection of excitonic coherence. *Science*, 316:1462, 2007.

[11] D. Abramavicius, D. V. Voronine, and S. Mukamel. Double-quantum resonance and exciton-scattering in coherent 2d spectroscopy of photosynthetic complexes. *Proceedings of the National Academy of Sciences*, 105(25):8525, 2008.

[12] Ben Bruggeman and Volkhard May. Ultrafast laser pulse control of exciton dynamics: a computational study on the fmo complex. *Journal of Physical Chemistry B*, 108(29):10529, 2004.

[13] Henk Fidder, Jasper Knoester, and Douwe A. Wiersma. Observation of the one-exciton to two-exciton transition in a J-aggregate. *Journal of Chemical Physics*, 98:6564, 1993.

[14] Arend G. Dijkstra, Thomas la Cour Jansen, and Jasper Knoester. Localization and coherent dynamics of excitons in the two-dimensional optical spectrum of molecular J-aggregates. *The Journal of Chemical Physics*, 128:164511, 2008.

[15] D. S. Chemla and Jagdeep Shah. Many-body and correlation effects in semiconductors. *Nature*, 411:549, 2001.

[16] M. Koch, J. Feldmann, G. von Plessen, E. O. Gobel, and P. Thomas. Quant um beats versus polarization interference: An experimental distinct ion. *Physical Review Letters*, 69:3631, 1992.

[17] L. Shulthesis, J. Kuhl, A. Honold, and C. W. Tu. Ultrafast phase relaxation of excitons via exciton-exciton and exciton–electron collisions. *Physical Review Letters*, 57(13):1635, 1986.

[18] Hailin Wang, Kyle Ferrio, Duncan G. Steel, Y. Z. Hu, R. Binder, and S. W. Koch. Transient nonlinear optical response from excitation induced dephasing in gaas. *Physical Review Letters*, 71(8):1261, 1993.

[19] R. C. Miller, D. A. Kleinman, A. C. Gossard, and O. Munteanu. Biexcitons in gaas quantum wells. *Physical Review B*, 25(10):6545, 1982.

[20] K. Bott, O. Heller, D. Bennhardt, S. T. Cundiff, P. Thomas, E. J. Mayer, G. O. Smith, R. Eccleston, J. Kuhl, and K. Ploog. Influence of exciton-exciton interactions on the coherent optical response in gaas quantum wells. *Physical Review B*, 48(23):17418, 1993.

[21] E. J. Mayer, G. O. Smith, V. Heuckeroth, J. Kuhl, K. Bott, A. Schulze, T. Meier, D. Bennhardt, S. W. Koch, P. Thomas, R. Hey, and K. Ploog. Evidence of biexcitonic contributions to four-wave mixing in gaas quantum wells. *Physical Review B*, 50(19):14730, 1994.

[22] Arthur L. Smirl, Martin J. Stevens, X. Chen, and O. Buccafusca. Heavy-hole and light-hole oscillations in the coherent emission from quantum wells: Evidence for exciton-exciton correlations. *Physical Review B*, 60:8267, 1999.

[23] Tobias Voss, Ilja Ruckman, Jurgen Gutowski, Vollrath Martin Axt, and Tilman Kuhn. Coherent control of the exciton and exciton-biexciton transitions in the generation of nonlinear wave-mixing signals in a semiconductor quantum well. *Physical Review B*, 73:115311, 2006.

[24] P. Gilliot, S. Cronenberger, H. Rahimpour Soleimani, C. Brimont, O. Crgut, M. Gallart, and B. Hnerlage. Measurement of exciton spin coherence by non-degenerate four-wave mixing experiments in the $\chi^{(3)}$ regime. *Physical Review B*, 75:125209, 2007.

[25] Jeffrey A. Davis and Chennupati Jagadish. Ultrafast spectroscopy of zno/znmgo quantum wells. *Laser and Photonics Reviews*, 3:85, 2008.

[26] R. Oszwaldowski, D. Abramavicius, and S. Mukamel. Many-body effects in two-dimensional optical spectra of semiconductor quantum dot pairs; time-dependent hartreefock approximation and beyond. *Journal of Physics: Condensed Matter*, 20:045206, 2008.

[27] Mark C. Phillips, Hailin Wang, I. Rumyantsev, N. H. Kwong, R. Takayama, and R. Binder. Electromagnetically induced transparency in semiconductors via biexciton coherence. *Physical Review Letters*, 91(18):183602, 2003.

[28] Xiaoqin Li, Yanwen Wu, Duncan Steel, D. Gammon, T. H. Stievater, D. S. Katzer, D. Park, C. Piermarocchi, and L. J. Sham. An all-optical quantum gate in a semiconductor quantum dot. *Science*, 301:809, 2003.

[29] Valery I. Rupasov and Victor I. Klimov. Carrier multiplication in semiconductor nanocrystals via intraband optical transitions involving virtual biexciton states. *Physical Review B*, 76:125321, 2007.

[30] R.J. Ellingson, M.C. Beard, J.C. Johnson, P. Yu, O. I. Micic, A. J. Nozik, A. Shabaev, and A. L. Efros. Highly efficient multiple exciton generation in colloidal pbse and pbs quantum dots. *Nanotechnology Letters*, 5:865, 2005.

[31] Ziad Ganim, Hoi Sung Chung, Adam W. Smith, Lauren P. DeFlores, Kevin C. Jones, and Andrei Tokmakoff. Amide i two-dimensional infrared spectroscopy of proteins. *Accounts of Chemical Research*, 41:432, 2007.

[32] Junrong Zheng, Kyungwon Kwak, and M. D. Fayer. Ultrafast 2d ir vibrational echo spectroscopy. *Accounts of Chemical Research*, 40:75, 2007.

[33] Peter Hamm, Jan Helbing, and Jens Bredenbeck. Two-dimensional infrared spectroscopy of photoswitchable peptides. *Annual Reviews of Physical Chemistry*, 59:291, 2007.

[34] Eric C. Fulmer, Feng Ding, Prabuddha Mukherjee, and Martin T. Zanni. Vibrational dynamics of ions in glass from fifth-order two-dimensional infrared spectroscopy. *Physical Review Letters*, 94:067402, 2005.

[35] David M. Jonas. Optical analogs of 2d nmr. *Science*, 200:1515, 2003.

[36] Sarah M. Gallagher, Allison W. Albrecht, John D. Hybl, Brett L. Landin, Bhavani Rajaram, and David M. Jonas. Heterodyne detection of the complete electric field of femtosecond four-wave mixing signals. *Journal of the Optical Society of America B*, 15:2338, 1998.

[37] Tianhao Zhang, Camelia N. Borca, Xiaoqin Li, and S. T. Cundiff. Optical two-dimensional fourier transform spectroscopy with active interferometric stabilization. *Optics Express*, 13:7432, 2005.

[38] Tobias Brixner, Jens Stenger, Harsha M. Vaswani, Minhaeng Cho, Robert E. Blankenship, and Graham R. Fleming. Two-dimensional spectroscopy of electronic couplings in photosynthesis. *Nature*, 434:625, 2005.

[39] M.L. Cowan, J.P. Ogilvie, and R.J.D. Miller. Two-dimensional spectroscopy using diffractive optics based phased-locked photon echoes. *Chemical Physics Letters*, 386:184, 2004.

[40] Marc M. Wefers and Keith A. Nelson. Analysis of programmable ultrashort waveform generation using liquid-crystal spatial light modulators. *Journal of the Optical Society of America B*, 12:1343, 1995.

[41] Joshua C. Vaughan, T. Feurer, and Keith A. Nelson. Automated two-dimensional femtosecond pulse shaping. *Journal of the Optical Society of America B*, 19:2489, 2002.

[42] T. Feurer, Joshua C. Vaughan, and Keith A. Nelson. Spatiotemporal coherent control of lattice vibrational waves. *Science*, 299:374, 2003.

[43] J. C. Vaughan, T. Hornung, K. W. Stone, and K. A. Nelson. Coherently controlled ultrafast four-wave mixing spectroscopy. *Journal of Physical Chemistry A*, 111(23):4873, 2007.

[44] P. Tian, D. Keusters, Y. Suzaki, and W. S. Warren. Femtosecond phase-coherent two-dimensional spectroscopy. *Science*, 300:1553, 2003.

[45] Ulrike Selig, Florian Langhojer, Frank Dimler, Tatjana Lhrig, Christoph Schwarz, Bjrn Gieseking, and Tobias Brixner. Inherently phase-stable coherent two-dimensional spectroscopy using only conventional optics. *Optics Letters*, 33:2851, 2008.

[46] Richard R. Ernst, Geoffrey Bodenhausen, and Alexander Wokaun. *Principles of Nuclear Magnetic Resonance in One and Two Dimensions*. Oxford University Press, 1990.

[47] HoiSung Chung, Munira Khalil, and Andrei Tokmakoff. Nonlinear infrared spectroscopy of protein conformational change during thermal unfolding. *The Journal of Physical Chemistry B*, 108:15332, 2004.

[48] Valentina Cervetto, Peter Hamm, and Jan Helbing. Transient 2d-ir spectroscopy of thiopeptide isomerization. *The Journal of Physical Chemistry B*, 112:8398, 2008.

[49] Martin T. Zanni, Nien-Hui Ge, Yung Sam Kim, and Robin M. Hochstrasser. Two-dimensional ir spectroscopy can be designed to eliminate the diagonal peaks and expose only the crosspeaks needed for structure determination. *Proceedings of the National Academy of Sciences*, 98:11265, 2001.

[50] Mark A. Rickard, Andrei V. Pakoulev, Nathan A. Mathew, Kathryn M. Kornau, and John C. Wright. Frequency- and time-resolved coherence transfer spectroscopy. *The Journal of Physical Chemistry A*, 111:1163, 2007.

[51] D. Kraemer, M.L. Cowan, A. Paarmann, N. Huse, E.T.J. Nibbering, T. Elsaesser, and R.J.D. Miller. Temperature dependence of the two-dimensional infrared spectrum of liquid h_2o. *Proceedings of the National Academy of Sciences*, 105:437, 2008.

[52] John D. Hybl, Allison W. Albrecht, Sarah M. Gallagher Faeder, and David M. Jonas. Two-dimensional electronic spectroscopy. *Chemical Physics Letters*, 297:307, 1998.

[53] T. Zhang, I. Kuznetsova, T. Meier, Xiaoqin Li, R. P. Mirin, P. Thomas, and S. T. Cundiff. Multidimensional ultrafast spectroscopy special feature: polarization-dependent optical 2d fourier transform spectroscopy of semiconductors. *Proceedings of the National Academy of Sciences*, 104(36):14227, 2007.

[54] M. C. Asplund, M. T. Zanni, and R. M. Hochstrasser. Two-dimensional infrared spectroscopy of peptides by phase-controlled femtosecond vibrational photon echoes. *Proceedings of the National Academy of Sciences*, 97:8219, 2000.

[55] David M. Jonas. Two-dimensional femtosecond spectroscopy. *Annual Reviews of Physical Chemistry*, 54:425, 2000.

[56] M. Khalil, N. Demirdoven, and A. Tokmakoff. Coherent 2d ir spectroscopy: molecular structure and dynamics in solution. *Journal of Physical Chemistry A*, 107:5258, 2003.

[57] M. Munowitz and A. Pines. Multiple-quantum nuclear magnetic resonance spectroscopy. *Science*, 233:525, 1986.

[58] A. Wokaun and R. R. Ernst. Selective detection of multiple quantum transitions in nmr by 2-dimensional spectroscopy. *Chemical Physics Letters*, 52:407, 1977.

[59] Wolfgang Richter and Warren S. Warren. Intermolecular multiple quantum coherences in liquids. *Concepts in Magnetic Resonance*, 12:396, 2000.

[60] Gigi Galiana, Rosa T. Branca, Elizabeth R. Jenista, and Warren S. Warren. Accurate temperature imaging based on intermolecular coherences in magnetic resonance. *Science*, 322:421, 2008.

[61] Eric C. Fulmer, Prabuddha Mukherjee, Amber T. Krummel, and Martin T. Zanni. A pulse sequence for directly measuring the anharmonicities of coupled vibrations: Two-quantum two-dimensional infrared spectroscopy. *Journal of Chemical Physics*, 120:8067, 2004.

[62] Soohwan Sul, Denis Karaiskaj, Ying Jiang, and Nien-Hui Ge. Conformations of n-acetyl-l-prolinamide by two-dimensional infrared spectroscopy. *The Journal of Physical Chemistry B*, 110:19891, 2006.

[63] Andrei V. Pakoulev, Mark A. Rickard, Kent A. Meyer, Kathryn Kornau, Nathan A. Mathew, David E. Thompson, and John C. Wright. Mixed frequency/time domain optical analogues of heteronuclear multidimensional nmr. *The Journal of Physical Chemistry A*, 110:3352, 2006.

[64] Marcos Dantus and Vadim V. Lozovoy. Experimental coherent laser control of physicochemical processes. *Chemical Reviews*, 104:1813, 2004.

[65] A. M. Weiner. Femtosecond pulse shaping using spatial light modulators. *Review of Scientific Instruments*, 71:1929, 2000.

[66] M. Ninck, A. Galler, T. Feurer, and T. Brixner. Programmable common-path vector field synthesizer for femtosecond pulses. *Optics Letters*, 32:3379, 2007.

[67] G. Stobrawa, M.Hacker, T. Feurer, D. Zeidler, M. Motzkus, and F. Reichel. A new high-resolution femtosecond pulse shaper. *Applied Physics B*, 72:627, 2001.

[68] Weiguo Yang, Dorine Keusters, Debabrata Goswami, and Warren S. Warren. Rapid ultrafine-tunable optical delay line at the 1.55-mm wavelength. *Optics Letters*, 23:1843, 1998.

[69] Sang-Hee Shim, David B. Strasfeld, Eric C. Fulmer, and Martin T. Zanni. Femtosecond pulse shaping directly in the mid-ir using acousto-optic modulation. *Optics Letters*, 31:838, 2006.

[70] P. Wasylczyk C. Radzewicz, W. Wasilewski, and J. S. Krasinski. Piezo-driven deformable mirror for femtosecond pulse shaping. *Optics Letters*, 29:177, 2004.

[71] Uma Krishnamoorthy Kebin Li, Jonathan P. Heritage, and Olav Solgaard. Coherent micromirror arrays. *Optics Letters*, 27:366, 2002.

[72] M. Hacker, G. Stobrawa, R. Sauerbrey, T. Buckup, M. Motzkus, M. Wildenhain, and A. Gehner. Micromirror slm for femtosecond pulse shaping in the ultraviolet. *Applied Physics B*, 76:711, 2003.

[73] J. C. Vaughan, T. Feurer, K. W. Stone, and K. A. Nelson. Analysis of replica pulses in femtosecond pulse shaping with pixelated devices. *Optics Express*, 14(3):1314, 2006.

[74] J. C. Vaughan. *Two-Dimensional Ultrafast Pulse Shaping and its Application to Coherent Control and Spectroscopy.* PhD thesis, Massachusetts Institute of Technology, 2005.

[75] L. Lepetit, G. Cheriaux, and M. Joffre. Linear techniques of phase measurement by femtosecond spectral interferometry for applications in spectroscopy. *Journal of the Optical Society of America B*, 12(12):2467, 1995.

[76] A. A. Maznev, T. F. Crimmins, and K. A. Nelson. How to make femtosecond pulses overlap. *Optics Letters*, 23:1378, 1998.

[77] J. C. Vaughan, T. Hornung, T. Feurer, and K. A. Nelson. Diffraction-based femtosecond pulse shaping with a two-dimensional spatial light modulator. *Optics Letters*, 30(3):323, 2005.

[78] Edwin D. Becker. *High Resolution NMR.* Academic Press, New York, 1980.

[79] Ellen H. G. Backus, Sean Garrett-Roe, and Peter Hamm. Phasing problem of heterodyne-detected two-dimensional infrared spectroscopy. *Optics Letters*, 33:2665, 2008.

[80] A. D. Bristow, D. Karaiskaj, X. Dai, and S. T. Cundiff. All-optical retrieval of the global phase for two-dimensional fourier-transform spectroscopy. *Optics Express*, 16:18017, 2008.

[81] Shaul Mukamel and Darius Abramavicius. Many-body approaches for simulating coherent nonlinear spectroscopies of electronic and vibrational excitons. *Chemical Reviews*, 104:2073, 2004.

[82] Vladimir Chernyak, Wei Min Zhang, and Shaul Mukamel. Multidimensional femtosecond spectroscopies of molecular aggregates and semiconductor nanostructures: The nonlinear exciton equations. *Journal of Chemical Physics*, 109:9587, 1998.

[83] T. Meier, P. Thomas, and S. W. Koch. *Coherent semiconductor optics: from basic concepts to nanostructure applications.* Springer, Berlin; New York, 2007.

[84] V.M. Axt and A. Stahl. A dynamics-controlled truncation scheme for the hierarchy of density matrices in semiconductor optics. *Zeitschrift fur Physik B*, 93:195, 1994.

[85] Harmut Haug and Stephan W. Koch. *Quantum theory of the optical and electronic properties of semiconductors.* World Scientific, Singapore, 2004.

[86] J. M. Shacklette and S. T. Cundiff. Role of excitation-induced shift in the coherent oprical response of semiconductors. *Physical Review B*, 66:045309, 2002.

[87] X. Li, T. Zhang, C. N. Borca, and S. T. Cundiff. Many-boby interactions in semiconductors probed by optical two-dimensional fourier transform spectroscopy. *Physical Review Letters*, 96:057406, 2006.

[88] Camelia N. Borca, Tianhao Zhang, Xiaoqin Li, and Steven T. Cundiff. Optical two-dimensional fourier transform spectroscopy of semiconductors. *Chemical Physics Letters*, 416:311, 2005.

[89] N. H. Kwong, I. Rumyantsev, R. Binder, and Arthur L. Smirl. Relation between phenomenological few-level models and microscopic theories of the nonlinear optical response of semiconductor quantum wells. *Physical Review B*, 72:235312, 2005.

[90] L. Allen and J. H. Eberly. *Optical Resonance and Two-Level Atoms*. Dover Publications, Inc., New York, 1987.

[91] Shaul Mukamel. *Principles of Nonlinear Optical Spectroscopy*. Oxford University Press, Inc., New York, 1995.

[92] M Lindberg, R. Binder, and S. W. Koch. Theory of the semiconductor photon echo. *Physical Review A*, 45(3):1865, 1992.

[93] J. M. Shacklette and S. T. Cundiff. Nonperturbative transient four-wave-mixing line shapes due to excitation-induced shift and excitation-induced dephasing. *Journal of the Optical Society of America B*, 20:764, 2003.

[94] William E. Boyce and Richard C. DiPrima. *Elementary Differential Equations and Boundary Value Problems*. 7th edition edition, 2000.

[95] Robert W. Boyd. *Nonlinear Optics*. Academic Press, London, 2nd edition, 2003.

[96] H. A. Lorentz. *The theory of electrons and its applications to the phenomena of light and radiant heat*. 1916.

[97] J. Guo, J. Cooper, and A. Gallagher. Selective reflection from a dense atomic vapor. *Physical Review A*, 53:1130, 1996.

[98] S. T. Cundiff. Time domain observation of the lorentz-local field. *Laser Physics*, 12:1073, 2002.

[99] Peter Y. Yu and Manuel Cardona. *Fundamentals of semiconductors : physics and materials properties*. Springer, Berlin; New York, 2001.

[100] Marcos H Degani and Oscar Hipolito. The exciton-phonon system in gaas-$ga_{1-x}al_x$as quantum wells. *Semiconductor Science and Technology*, 2:578, 1987.

[101] S. Rudin and T. L. Reinecke. Size effects in the temperature dependence of exciton linewidths. *Phys. Stat. Sol.*, 190:677, 2002.

[102] D. Gammon, S. Rudin, T. L. Reinecke, D. S. Katzer, and C. S.Kyono. Phonon broadening of excitons in gaas/al$_x$ga$_{1-x}$, as quantum wells. *Physical Review B*, 51:16785, 1995.

[103] Karl Leo, Theo C. Damen, Jagdeep Shah, E. O. Gobel, and K. Kohler. Quantum beats of light hole and heavy hole excitons in quantum wells. *Applied Physics Letters*, 57:19, 1990.

[104] M. Koch, J. Feldmann, G. von Plessen, E. O. Gobel, P. Thomas, and K. Kohler. Quantum beats versus polarization interference: An experimental distinct ion. *Physical Review Letters*, 69:3631, 1992.

[105] G. Manzke, Q. Y. Peng, K. Henneberger, U. Neukirch, K. Hauke, K. Wundke, J. Gutowski, and D. Hommel. Density dependence of the exciton energy in semiconductors. *Physical Review Letters*, 80(22):4943, 1998.

[106] K. Leo, M. Wegener, J. Shah, D. S. Chemla, E. O. Gobel, T. Damen, S. Schmitt-Rink, and W. Schafer. Effects of coherent polarization interactions on time-resolved degenerate four-wave mixing. *Physical Review Letters*, 65:1340, 1990.

[107] M. Wegener, D. S. Chemla, S. Schmitt-Rink, and W. Schafer. Line shape of time-resolved four-wave mixing. *Physical Review A*, 42(9):5675, 1990.

[108] T. F. Albrecht, K. Bott, T. Meier, A. Schulze, M. Koch, S. T. Cundiff, J. Feldmann, W. Stolz, P. Thomas, S. W. Koch, and E. O. Gobel. Disorder mediated biexcitonic beats in semiconductor quantum wells. *Physical Review B*, 54:4436, 1996.

[109] Lijun Yang and Shaul Mukamel. Two-dimensional correlation spectroscopy of two-exciton resonances in semiconductor quantumwells. *Physical Review Letters*, 100:057402, 2008.

[110] Lijun Yang and Shaul Mukamel. Revealing exciton-exciton couplings in semiconductors using multidimensional four-wave mixing signals. *Physical Review B*, 77:075335, 2008.

[111] I. Kuznetsova, T. Meier, S. T. Cundiff, and P. Thomas. Determination of homogeneous and inhomogeneous broadening in semiconductor nanostructures by two-dimensional fourier-transform optical spectroscopy. *Physical Review B*, 76(153301), 2007.

[112] V. M. Axt and T. Kuhn. Femtosecond spectroscopy in semiconductors: a key to coherences, correlations and quantum kinetics. *Reports on Progress in Physics*, 67:433, 2004.

[113] D. S. Chemla and Jagdeep Shah. Many-body and correlation effects in semiconductors. *Nature*, 411:549, 2001.

[114] S. W. Koch, M..Kira, and T. Meier. Correlation effects in the excitonic optical properties of semiconductors. *Journal of Optics B*, 3:R29, 2001.

[115] Steven T. Cundiff. Coherent spectroscopy of semiconductors. *Optics Express*, 16(7):4639, 2008.

[116] B. F. Feuerbacher, J. Kuhl, and K. Ploog. Biexcitonic contribution to the degenerate-four-wave-mixing signal from a gaas/al$_x$ga$_{1-x}$as quantum well. *Physical Review B*, 43(3):2439, 1991.

[117] W. S. Warren and A. Pines. Analogy of multiple-quantum nmr to isotopic spin labeling. *Journal of the American Chemical Society*, 103:1613, 1981.

[118] G. Chen, T. H. Stievater, E. T. Batteh, Xiaoqin Li, D. G. Steel, D. Gammon, D. S. Katzer, D. Park, and L. J. Sham. Biexciton quantum coherence in a single quantum dot. *Physical Review Letters*, 88(11):117901, 2002.

[119] K. B. Ferrio and D. G. Steel. Observation of the ultrafast two-photon coherence biexciton oscillation in a gaas/al$_x$ga$_{1-x}$as multiple quantum well. *Physical Review B*, 54(8):R5231, 1996.

[120] Daniel B. Turner, Katherine W. Stone, Kenan Gundogdu, and Keith A. Nelson. Three-dimensional electronic spectroscopy of excitons in gaas quantum wells. in progress.

[121] H. Wang, K. B. Ferrio, D. G. Steel, P. R. Berman, Y. Z. Hu, R. Binder, and S. W. Koch. Transient four-wave-mixing line shapes: Effects of excitation-induced dephasing. *Physical Review A*, 49:R1551, 1994.

[122] T. Meier, S. W. Koch, Mark Phillips, and Hailin Wang. Strong coupling of heavy- and light-hole excitons induced by many-body correlations. *Physical Review B*, 62:12605, 2000.

[123] K.-H. Pantke, D. Oberhauser, V. G. Lyssenko, J. M. Hvam, and G. Weimann. Coherent generation and interference of excitons and biexcitons in gaas/algaas quantum wells. *Physical Review B*, 47:2413, 1993.

[124] Hailin Wang, Jagdeep Shah, T. C. Damen, and L. N. Pfeiffer. Polarization-dependent coherent nonlinear optical response in gaas quantum wells: Dominant effects of two-photon coherence between ground and biexciton states. *Solid State Communications*, 91:869, 1994.

[125] D. Birkedal, J. Singh, V. G. Lyssenko, J. Erland, and J. M. Hvam. Binding of quasi-two-dimensional biexcitons. *Physical Review Letters*, 76:672, 1996.

[126] S. R. Bolton, U. Neukirch, L. J. Sham, D. S. Chemla, and V. M. Axt. Demonstration of sixth-order coulomb correlations in a semiconductor single quantum well. *Physical Review Letters*, 85:2002, 2000.

[127] Ksenia Dolgaleva, Robert W. Boyd, and Peter W. Milonni. Influence of local-field effects on the radiative lifetime of liquid suspensions of nd:yag nanoparticles. *The Journal of the Optical Society of America B*, 24:516, 2007.

[128] Heping Zeng and Han Xu. Quantum controllable optical selective resonant excitation in a dense medium. *Physical Review A*, 69:043803, 2004.

[129] Daniel A. Steck. Rubidium 85 d line data, 2008.

[130] T. S. Humble and J. A. Cina. Molecular state reconstruction by nonlinear wavepacket interferometry. *Physical Review Letters*, 93(6):060402, 2004.